Search for periodic resonances at $\sqrt{s} = 13$ TeV with ATLAS detector

by

Ho Chun Lau

A thesis submitted in partial fulfillment of the requirements for the degree of

Master of Science

Department of Physics
University of Alberta

Abstract

Integrating gravity into the Standard Model (SM) of particle physics presents a challenge in formulating a unified theory of all interactions. Quantum gravity inherits a principle from quantum field theories. Here, gravity is interpreted as a field. This conceptualization leads to the quantization of the gravitional field, which necessitates the hypothesis of a tensor spin-2 particle, known as the graviton (G), as the gravitational force carrier. Previous models such as the Arkani-Dimopoulos-Dvali (ADD) large extra dimensions model and the Randall-Sundrum (RS) wrapped extra dimension model attempted to unify gravity with other forces and predict the existence of gravitons. However, the absence of experimental evidence to support the predictions of these models has halted their success. The clockwork/linear dilaton (CW/LD) model which is a variation of two models offers an alternative approach. It predicts a series of massive gravitons that may be produced at Large Hadron Collider collision energies, and appear in the detectors through 2-body graviton decays, such as $G \to e^+e^-$ and $G \to \gamma\gamma$. The graviton resonance pattern is different from predictions of the ADD and RS models.

This thesis presents an analysis of the e^+e^- and $\gamma\gamma$ invariant mass spectrums acquired by the ATLAS experiment during 2015 to 2018 with an integrated luminosity of 140 fb^{-1} at $\sqrt{s} = 13$ TeV. A Fourier transform tailored to the CW/LD model's periodic signal hypothesis, is used to search for graviton resonances. An invariant mass range of [250, 4182] GeV for e^+e^-, and [150, 2360] GeV for $\gamma\gamma$ has been searched. The investigation reveals no significant deviations from SM expectations. The most pronounced signal appears with a period of 1 TeV(0.6 TeV) in the $e^+e^-(\gamma\gamma)$ invariant mass spectrum with a global significance of 0.14(0.20) standard deviations. In the absence of a significant excess, we constrain the parameter space of the CW/LD model by setting exclusion limits.

Acknowledgements

This thesis is dedicated to my beloved father. Thank you for staying strong and waiting for me to finish my studies while you are fighting with cancer. It is my deepest sorrow that I could not be with you throughout this journey, I hope it is not too late, but I have finally made it. I promise I will make you proud, now and the future. Thank you my mother and brother, bearing the duties of taking care of father while I was away, I know it has been not easy, and I always feel guilty about it. I would like to thank my supportive supervisor, Dr. Douglas Gingrich, for his guidance and support throughout my study. You are an excellent mentor, providing me opportunities to grow and learn, and pushing me when I am not doing enough. I also want to thank my helpful post-doc, Jack Lindon, for his patience and guidance in teaching me the physics; and the best office-mate Mitch Kelly, for listening to all my complaints and sharing all the joy with me. Thank you my beloved girlfriend Ka Yin, for your support and encouragement, and for being there for me when I need you the most. I am deeply thankful to my friends Kyle, Kylie and Ice, eating dim sum (occasionally ice-cream) together every week is one of the best memories I have in Edmonton. For Shelby, Joshua, and all my friends in Edmonton, thank you for making my life in Edmonton so much better. This journey has been filled with bittersweet memories, I do not regret it, and I am glad that I have you all with me.

Table of Contents

List of Tables

List of Figures

Chapter 1

Introduction

The SM of particle physics [1] serves as our current best explanation for three of the core forces that define the nature of the universe: the electromagnetic, weak, and strong forces. Incorporating gravity into the SM has been a challenge. Unifying gravity with the other forces within a quantum mechanical framework requires the introduction of the graviton, a quantization of the gravitational field [2]. However, including the graviton into the quantum framework is impeded by the non-renormalizable nature of gravity at high energies, leading to the hierarchy problem [2].

Proposed solutions to include gravity come from the model of large extra dimensions presented by Arkani-Hamed, Dimopoulos, Dvali, often referred to as the ADD model [2–4], and the five-dimensional warped geometry model proposed by Randall and Sundrum, known as the RS model [4–6]. These models provided a framework that reconcile the observed weakness of gravity with the other forces, suggesting a construction of a higher dimensional space-time to permit the existence of graviton. Both models predict massive gravitons, which are Kaluza-Klein excitations of the massless graviton. Extensive searches for gravitons and extra dimensions have been conducted by the ATLAS and CMS collaborations at CERN's Large Hadron Collider, and other collaborations [7–11]. No evidence of the graviton has been found, and exclusion limits have been set on the parameter space of these models.

The clockwork model [12], which bears similarities to the linear dilaton (LD) model [13], has been introduced to address the hierarchy and Higgs naturalness problems. The clockwork model is closely related to string theory as it has an identical spacetime metric to the LD model, which approximates the dual of Little String Theory [14, 15]. Despite a lot of similarities with ADD and RS phenomenology, the CW/LD model predicts a different graviton spectrum. In the theory, two undetermined parameters, the Higgs-curvature k and the five-dimensional fundamental Planck scale M_5, dictate the graviton masses. The CW/LD graviton spectrum has multiple resonances, unlike the continuum of densely packed mass states in the ADD model. Conversely, the RS model represents another extreme, with gravitons widely spaced in mass precluding observation of multiple resonances within the LHC's energy range. The CW/LD model, however, predicts a closely spaced quasi-periodic pattern of graviton masses.

The CMS collaboration has conducted a search for gravitons in the CW/LD model using the diphoton ($\gamma\gamma$) decay channel [16], however, the search does not address the periodicity, rather it regards CW/LD gravitons are closely packed as if they are ADD gravitons, but on-shell. They exclude values of M_5 lower than 5 TeV for k values in the range of 0.1 GeV to 2.0 TeV at 95 % confidence level. ATLAS also conduct a search concurrent with this thesis [17], a neural network approach is applied. They exclude the value of M_5 in the range 11 TeV to 1 TeV for values of k in the range 0.1 TeV to 3.0 TeV at 95 % confidence level also using the $\gamma\gamma$ channel. They also obtained an exclusion limit using the e^+e^- channel, but the limit is not as strong as using the $\gamma\gamma$ channel.

In this study, we performed an analysis using the clockwork model to search for CW/LD gravitons at the LHC in the e^+e^- and $\gamma\gamma$ graviton decay channels. We are interested in two undetermined parameters (k, M_5) in the model. If the data show no significant deviation from the SM predictions, gravitons are not observed, and we set an upper limit on the production cross-section × acceptance × efficiency × branching ratio in proton-proton (pp) collisions using the data from ATLAS experiment [17].

Using the model, these limits are converted to limits on the model parameters. A lower limit of M_5 versus k for the CW/LD model is obtained in both e^+e^- and $\gamma\gamma$ gravity decay channels.

The layout of this thesis is as follows:

Chapter 2 provides a brief overview of the Standard Model and the clockwork model. The main aspect of creating particles through symmetry breaking and the hierarchy problem are discussed.

Chapter 3 provides a detailed description of the clockwork model and the clockwork graviton. The production of clockwork graviton in pp collision and the decay of clockwork graviton into e^+e^- and $\gamma\gamma$ are discussed.

Chapter 4 provides a brief overview of the LHC, related parts of the ATLAS detector and the conventional terminology used by ATLAS. It also describes the triggering used by ATLAS for data acquisition.

Chapter 5 provides an overview of the data selection process, from $ee/\gamma\gamma$ reconstructions to object selection requirement, and the event selection process. It also described the triggering used to extract relevant data.

Chapter 6 provides detailed information on the Monte Carlo (MC) simulation used in this study. It describes both the MC signal and background generation in *truth* level. It included the use of transfer method to model the detector responses to the simulated events; and described the algorithm to include cascade of decay events.

Chapter 7 discusses the main analysis methods: model independent Fourier transform and model dependent Fourier transform.

Chapter 8 provides a detailed statistical method used in this study. The methodology to evaluate the discovery significance and the exclusion limit are described. The test statistics used in this study derived from the Fourier transform application are also discussed in this chapter.

Chapter 9 presents results of the analysis including the exclusion limit and discovery significance.

Chapter 2

Theories and models

In this chapter, the SM is first introduced, which serves as the cornerstone of particle physics theory and has undergone numerous measurements and tests. The SM is responsible for describing both the fundamental particles and known forces. Despite its many successes, the SM does not account for gravity, leading to the development of more advanced frameworks that incorporate and expand upon the SM's principles. One such framework is the clockwork model, which is of particular interest and will be discussed in this thesis. The clockwork model provides a mechanism for describing fundamental particles, including the graviton, a theoretically predicted carrier of gravitational force. This mechanism can be empirically tested using data collected by the ATLAS detector and has the potential to solve some of unanswered questions left by the SM: hierarchy problem and Higgs naturalness.

2.1 Standard Model

The SM represents the most comprehensive theoretical framework for describing the fundamental particles and their interactions. Particles can be classified into two distinct categories based on their intrinsic spins: fermions and bosons.

Fermions are characterized with half-integer spin and obey Fermi-Dirac statistics, and are further subdivided into two primary groups: leptons and quarks, both of which comprise three generations primarily distinguished by their invariant mass. In the lepton category, electrons (e), muons (μ), and tau particles (τ) each constitute one generation, accompanied by their corresponding neutrinos (ν_ℓ). The quarks are classified with six distinct flavors: up (u) and down (d) quarks, strange (s) and charm (c) quarks, as well as bottom (b) and top (t) quarks, with each flavor pair forming one generation. Furthermore, there exists anti-leptons and anti-quarks, which have identical mass to their corresponding particle counterparts but possess opposing quantum numbers, including electric charge and lepton number.

The bosons are characterized with integer spin which obey Bose-Einstein statistic, and the vector bosons (spin-1) are the force carriers of fundamental forces: weak force, strong force and electromagnetic force. The known vector bosons are gluons (g), photons (γ), Z boson, $W^\pm$ bosons, and the only scalar boson is the Higgs boson (h). Due to the success of describing forces with the preceding bosons, it has been hypothesized that gravity could similarly be depicted through a force carrier, specifically, the graviton. However, this theoretical approach is not successful within the SM framework. This is primarily because gravity is incredibly weak compared to the other three forces and is difficult to reconcile with quantum mechanics A schematic table of the SM is shown in Fig. 2.1.

There are two main features of the SM, the global symmetry and local symmetry. Local symmetry refers to the invariant property under the space-time coordinate dependent transformation, for instance, the Maxwell equations are invariant under spacial rotation is a kind of local symmetry. In contrast, global symmetry pertain to the space-time coordinates independent transformation invariance, such as the rotation of self-interacting scalar fields which remain invariant when the rotation angle is unrelated to space-time.

The Lagrangian of the SM is constructed to be invariant under particular local symmetries. To maintain the invariance when undergoing space-time dependent transformation, additional gauge field is introduced to compensate the change induced by the transformation. Consequently, quantization of the field introduces the gauge

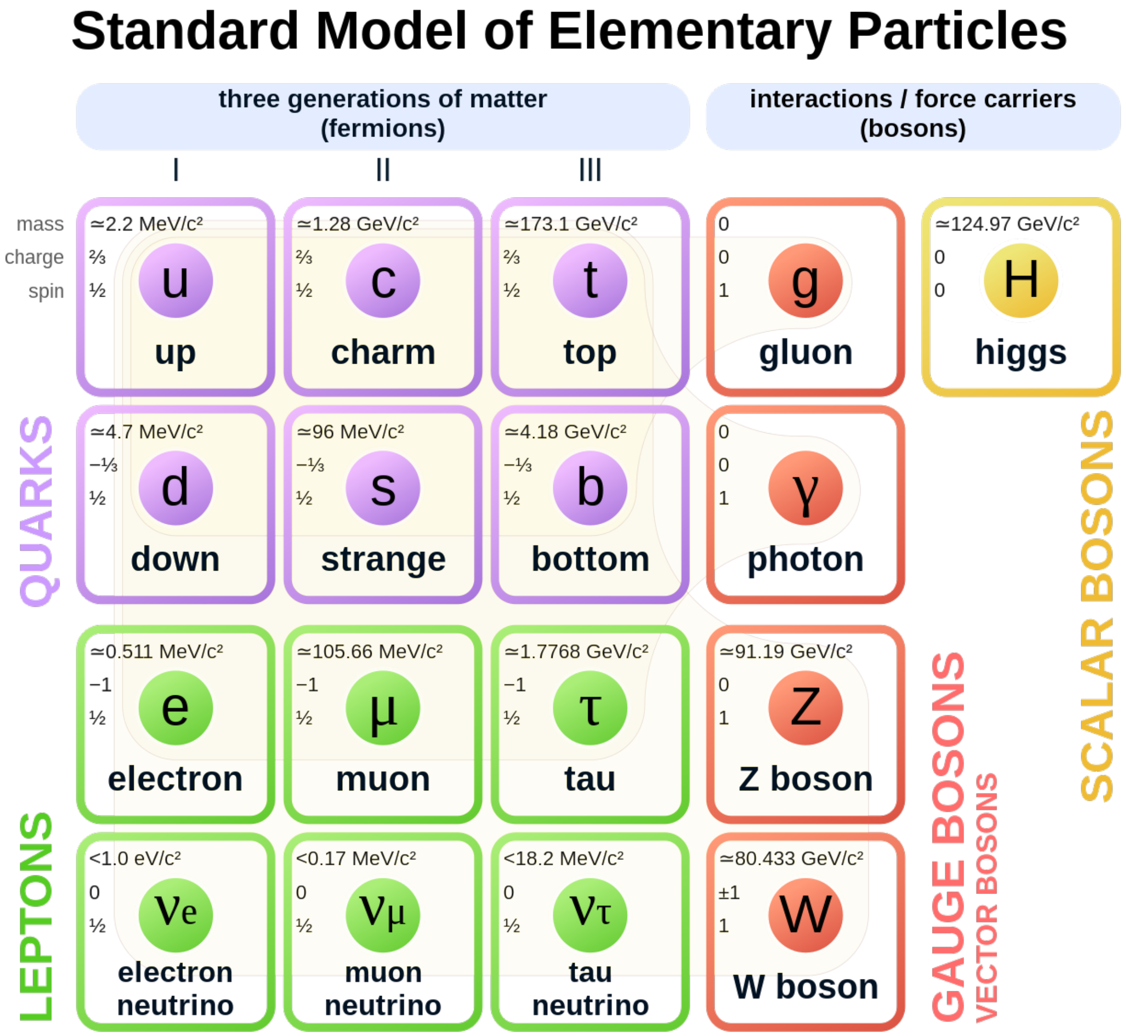

Figure 2.1: A schematic diagram of the SM particles taken from Wikipedia, and in public domain. The mass, charges and the spin are listed next to the particle. The anti-particles are not shown but are implied for the fermions.

bosons to the SM, which are the aforementioned force carriers. The mathematical formulations of the SM symmetry is represented by $SU(3)_C \times SU(2)_L \times U(1)_Y$, where the subscripts C, L, and Y denote color, left-handness, and weak hypercharge, respectively. And U, SU are the unitary and the special unitary group respectively.

The $SU(3)_C$ symmetry is the color symmetry as described by quantum chromodynamics (QCD). Within the QCD framework there are 3 colors. Each quark is assigned one color, and each gluon is assigned a color and anti-color pair. However, due to the traceless matrix property resulting from their massless nature, only eight linearly independent combinations of gluons exist. QCD explains the interactions between quarks and gluons, with gluons binding quarks together to form hadrons, such as baryons and mesons. These interactions play an important role in hadron-hadron collisions. The nuclear structure of protons was explained by parton theory and parton distribution functions [18] (PDF), which are extensively used in subsequent research. The partons are quarks and gluons, and PDFs are, in fact, (anti)quark and gluon distribution functions. Due to the non-perturbative nature of QCD, PDFs cannot be analytically derived or directly measured. However, a model can be formed from hadron-hadron collision data.

The $SU(2)_L$ weak isospin group that only applies to the left-handed fermions, are responsible for describing the behavior of the weak interaction mediated by the $W^\pm$ and Z bosons. $U(1)_Y$ is the hypercharge group, which is responsible for describing the behavior of the electromagnetic interaction mediated by the photon between all charged fermions. The $SU(2)_L$ and $U(1)_Y$ are combined to form the electroweak symmetry group $SU(2)_L \times U(1)_Y$. It unifies the electromagnetic and weak interactions into a single electroweak interaction. This symmetry undergoes a spontaneous symmetry breaking, giving the $W^\pm$ and Z bosons their masses, as well as the Higgs boson mass through the Higgs mechanism. The Higgs boson is the only scalar boson in the SM, and was discovered in 2012 at the Large Hadron Collider (LHC) at CERN with mass value 125 GeV.

Although the Standard Model has been immensely successful in explaining the behavior of fundamental particles and their interactions, it is crucial to recognize that it is not an all-encompassing theory. The number of empirical parameters in the SM is not desirable to physicists, we believe that there exist a better theory that can explain the same phenomena with fewer parameters. Moreover, there are a few unanswered questions in physics that the SM cannot explain [1], which brings us to the theory of interest, clockwork model.

2.2 Hierarchy Problem and Higgs Naturalness

Before introducing the clockwork model, we want to motivate the theory by introducing the hierarchy problem and the Higgs naturalness. The hierarchy problem arises from the two fundamental scales in physics: the Planck scale $M_{Pl} \approx 10^{18}$ GeV and the electroweak scale $m_{EW} \approx 10^3$ GeV [2]. Over the decades, explaining the order of magnitudes discrepancy between these two scales has been the main challenge in beyond Standard Model (BSM) theories. One common framework is to construct a new effective field theory (EFT) that is valid at low energies (weak scale), explaining the origin of the hierarchy. For instance, supersymmetry takes this approach. On the other hand, one can also construct a quantum theory of the gravity that is valid at high energies (Planck scale). In both paradigms, the values of M_{Pl} and m_{EW} are considered constant parameters that differentiate different regimes of physical phenomena. Quantum gravitational effects becomes dominant at distances smaller than M_{Pl}^{-1} (10^{-35}m in distance unit). Conversely, electroweak effects become increasingly important at distances smaller than m_{EW}^{-1} (10^{-24}m in distance unit).

It has been determined that the weak scale exhibits consistency up to 10^3 GeV, it also serves as the ultraviolet cutoff. Beyond the cutoff, the low energy approximation of the current theory becomes inapplicable, the constancy of the weak scale is no longer guaranteed, introducing a new theoretical framework in describe the behavior of the scale in that regime is necessary. A similar idea is applied to the gravitational interaction. The Planck length correspondingly the Planck scale serves as the ultraviolet cutoff of the general relativity, quantum gravity theory is needed in describing the gravitational interaction in that regime. Due to the technology limit on the experiments, we have ascertained that predictions of general relativity for gravitational interactions remain reliable down to length scale 0.01 meter, and we have further assumed the relativity theory is reliable between 0.01 m to the Planck length $\approx 10^{-35}$ m [2].

To explain the discrepancy between two scales, a common approach is to argue that the Planck scale is not truly fundamental, there exist an alternative true fundamental scale that is closer to the weak scale. The idea is to introduce n extra compactified spatial dimensions of radius R in addition to the 4 space-time dimensions we observed, and the gravitational interaction is allowed to propagate in the extra dimensions. Those extra dimensions are fundamental part of the nature, just like the 4 dimensions we are familiar with. However, these extra dimension are compactified, they are curled up at very small scale, thus have limited influence on macroscopic phenomena. The true fundamental scale is denoted as the reduced Planck scale $M_{(4+n)}$. In this framework, applying the Gauss's law in (4+n) dimensions, the gravitational potential $V(r)$ can be derived as

$$V(r) \approx \frac{m_1 m_2}{M_{(4+n)}^{n+2}} \frac{1}{r^{n+1}} \qquad (r \ll R), \tag{2.1}$$

where $M_{(4+n)}$ is the reduced Planck constant at $(4+n)$ dimensions. However, if the range of interaction is at distance $r \gg R$, the gravitational flux lines contributed by the extra dimensions are no longer significant, and the Newton's gravitational law is recovered.

$$V(r) \approx \frac{m_1 m_2}{M_{4+n}^{n+2} R^n} \frac{1}{r} \qquad (r \gg R), \tag{2.2}$$

and our effective 4 dimensional M_{Pl} is given by

$$M_{Pl}^2 \approx M_{4+n}^{2+n} R^n. \tag{2.3}$$

This relationship originated from the ADD model introduced by Arkani-Hamed, Savas Dimopoulos and Gia Dvali in 1998 [3], and later will be modified with the assumption made by the clockwork model.

The Higgs naturalness problem is associated with the Higgs boson mass and is closely related to the hierarchy problem. According to the naturalness criterion, parameters in a theory can be much smaller than unity only if setting them to zero increases the symmetry of the theory; otherwise, the theory is considered unnatural [19]. Throughout history, nature has often adhered to this criterion, studying the extreme values of model parameter and respecting the criterion has led physicists to the discovery of new physics that restores naturalness [20]. Physicists believe that all physical quantities observed at low energy scales are determined by the fundamental parameters at high energy scales with no free parameters. It is important to note that the criterion is not a physical principle but an aesthetic property, suggesting a meaningful interconnection between parameters.

A key point of interest is the large ratio between the Fermi constant and the Newton constant in natural unit, $\frac{G_F}{G_N}\left(\frac{c}{\hbar^2}\right) = 1.73859(15)\times 10^{33}$ [21]. The constant is again illustrating the strength difference between the electroweak and gravitational interactions. This has led physicists to question whether it stems from statistical fluctuations or cosmological evolution. In the SM, G_F is determined by the inverse square of the Higgs boson mass, m_H^{-2}. As the Higgs boson propagates in a vacuum, it interacts with virtual particles, and the mass squared receiving an additional contribution [20]:

$$\delta m_H^2 = \kappa \Lambda^2. \tag{2.4}$$

Here, Λ represents the maximum energy accessible to virtual particles, while κ is a proportionality constant accounting for different contributions to m_H. The leading correction to the Higgs mass is expressed as:

$$\kappa = \frac{3G_F}{4\sqrt{2}\pi^2}\left(4m_t^2 - 2m_w^2 - m_Z^2 - m_H^2\right). \tag{2.5}$$

In this equation, m_t, m_w, m_Z, and m_H denote the masses of the top quark, W boson, Z boson, and Higgs boson, respectively. The first three particles contributed to the leading effect as the Higgs field strongly interacts with heavier particles; The Higgs boson can also interact with itself, this is known as the Higgs self-interaction. Additionally, $\kappa \approx 3 \times 10^{-2}$. To account for the large G_F/G_N ratio, κ must be on the order of 10^{-32}. This discrepancy can only be resolved by assuming that when all quantum effects and higher energy corrections are included, this tiny value will be obtained. This necessitates a precise cancellation of contributions to m_H, a process known as fine-tuning. In the SM, the massive spin-zero Higgs boson does not have the extra symmetry that ensures the proportionality constant κ is small, making it unnatural [20]. Insisting on the naturalness criterion, it implies the possibility that unsolved mystery is behind the κ. As a result, the clockwork model has been proposed to address this issue.

2.3 Clockwork model

The clockwork mechanism [12] serves as a framework to describe the creation and decay of particles with exponentially suppressed interactions without introducing small parameters directly. This satisfies the naturalness criterion and offers a means for generating small numbers with only $\mathcal{O}(1)$ parameters, respecting the naturalness. In this framework, despite the presence of exponentially suppressed interaction strengths, an effectively large interaction scale can be realized for fermions, bosons, and even gravitons at low energies. Moreover, it serves as a mathematical tool for constructing axion, neutrinos, flavor, weak scale, and even gravitons [22].

The clockwork model has the same mathematical structure with the previously proposed linear dilaton (LD) model [13, 23–25], particularly the high dimensions space-time metric used by LD. They share a similar phenomenology, such as generating particles with different mass modes resembles the Kaluza-Klein (KK) excitations [26]. A dilaton is a scalar field that appears in all variants of string theory. The vacuum expectation value of the dilaton determines the gauge coupling parameters at high energy scale [25], and also determines the strength of the gravitational interaction at low energy by reducing high dimensional gravity and gauge groups to through low energy effective field theory. A linear dilaton is a particular solution that the coupling strength varies linearly with the coordinate of the extra spatial dimension. The clockwork model can be regard as a different interpretation of the existing LD model and will be referred to the Clockwork/Linear Dilaton (CW/LD) model in the following discussion.

The general framework of the mechanism can be described as follows. Consider a system that includes a massless particle P which its Lagrangian has a symmetry $\mathcal{S}$. The specific details of the model are not crucial for the setup. The system is duplicated into $N+1$ copies and treated as a one-dimensional lattice. It has a symmetry $\mathcal{G}$, where the product of the $N+1$ symmetries $\mathcal{S}$ is a subgroup of $\mathcal{G}$ ($\mathcal{G} \supseteq \mathcal{S}^{N+1}$). A soft symmetry breaking of $\mathcal{G}$ is induced by introducing mass mixing between neighboring lattice sites within the $N+1$ lattice. This construction is a common approach that resembles the fields in a deconstructed extra dimension [27]. However, the critical difference is the mass mixing in the CW/LD is asymmetric. In the mathematical formalism, the difference between dynamic quantities at adjacent sites j and $j+1$ is encapsulated by the term $(V_j - qV_{j+1})$. Here, V denotes a dynamic variable of interest, while $q \neq 1$ serves as a scaling parameter that quantifies the degree of asymmetry between the sites. In the one-dimensional lattice system with boundaries, it can form at most N links between the sites, breaking N individual symmetries $\mathcal{S}$. One symmetry group $\mathcal{S}_0$ remains, resulting in one particle P_0 remains massless. CW/LD model addresses two key ideas to obtain an exponential suppression. The influence of each site on its neighbor is scaled down by this factor q as $q \neq 1$. The massless particle

P_0 is located at the boundary site. As a result, the component of P_0 is exponentially suppressed at the opposite end by a factor of $1/q^N$.

By coupling the clockwork sector to the SM sector at the boundary with reasonably large values for q and N, a very small coupling of P_0 to the SM particles can be achieved without introducing parameters that violate the naturalness criterion. This avoids the need for small parameters, multiple mass scales, or exponentially large field multiplicity in the fundamental theory. The properties of P and $\mathcal{S}$ can be found in table 2.1. Again the clockwork mechanism is capable of generating various types of particles, including fermions, scalar and vector bosons, as well as the graviton. In the following discussion, clockwork scalar (spin-0) particles are first discussed, which help bridging the concepts to the clockwork graviton (spin-2).

P	Symmetry $\mathcal{S}$
Spin-0 scalar	Goldstone shift symmetry
Spin-1/2 fermion	chiral symmetry
Spin-1 boson	gauge symmetry
Spin-2 graviton	linearized 4D diffeomorphism invariance

Table 2.1: Particle types and their associated symmetries

2.3.1 Clockwork graviton

In this section a novel phenomena in the clockwork model is discussed: generating clockwork particles with different masses. A Goldstone boson is produced when the system undergoes spontaneous symmetry breaking [28]. Furthermore, if the nature of the breaking happens at all scales of energy, the process is denoted as a hard symmetry breaking. Hard spontaneous symmetry breaking results in a massive Goldstone boson, also known as pseudo-Goldstone boson. The mass of the pseudo-Goldstone boson can be derived from the non-derivative quadratic term in the Lagrangian [29], that is, the term is 0 for Goldstone boson, and non-zero for pseudo-Goldstone boson.

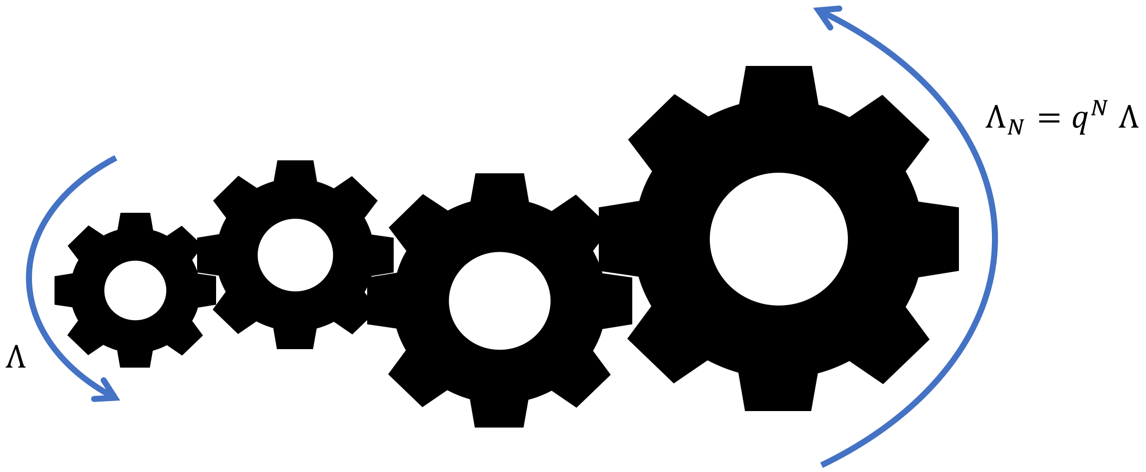

Figure 2.2: A schematic representation of the clockwork mechanism increasing the interaction scale [22].

A low energy effective Lagrangian of a clockwork scalar ϕ with two leading terms is given by

$$\mathcal{L} = -\frac{1}{2}\sum_{j=0}^{N}\partial_\mu\phi_j\partial^\mu\phi_j - \frac{1}{2}\sum_{i,j=0}^{N}\phi_i M^2_{\phi ij}\phi_j + \mathcal{O}(\phi^4), \tag{2.6}$$

where M^2_ϕ is the mass matrix. The resulting mass values are given by

$$\begin{gathered} m^2_{a_0} = 0, \;\; m^2_{a_k} = \lambda_n m^2, \;\; n = 1, ...N \\ \lambda_n = q^2 + 1 - 2q\cos\left(\frac{n\pi}{N+1}\right). \end{gathered} \tag{2.7}$$

The mass corresponding to the integer k is known as mass mode k, and subsequent masses can be obtained by increasing the integer mode k. Fig. 2.2 is a graphical representation of the clockwork mechanism where each gear represents a clockwork particle.

In the context of spin-2 gravitons, the situation bears resemblance to that of clockwork scalar [12]. Consider $N+1$ instances of massless gravitons, the existence of gravitons perturbs the flat spacetime, and we further introduce a perturbation in the spacetime to break the symmetry. The symmetry it possesses is the linearized 4D diffeomorphism invariance. Diffeomorphism is a property inherit from tensor equations that the form of the equation is independent of the choices of the coordinate system, which are explicitly used in formulating general relativity. This perturbed metric at site j : $g_j^{\mu\nu}$ is represented by $g_j^{\mu\nu} = \eta_j^{\mu\nu} + 2h_j^{\mu\nu}$, where $\eta_j^{\mu\nu}$ is the flat space-time metric, $h_j^{\mu\nu}$ is the perturbation. As a result of this perturbation, the symmetry of $N+1$ copies of diffeomorphism invariance is reduced to a singular diffeomorphism invariance. Analogous to the $U(1)^{N+1}$ symmetry breaking observed in the case of scalar fields. The leading terms of the clockwork Lagrangian, which encompasses the near-neighbor mass terms for massive gravitons [30], can be formulated as:

$$\mathcal{L} = -\frac{m^2}{2}\sum_{j=0}^{N-1}\left([h_j^{\mu\nu} - qh_{j+1}^{\mu\nu}]^2 - [\eta_{\mu\nu}(h_j^{\mu\nu} - qh_{j+1}^{\mu\nu})]^2\right), \tag{2.8}$$

such that the Lagrangian is up to linear approximation in the mass terms invariant under the gauge symmetry

$$h_j^{\mu\nu} \to h_j^{\mu\nu} + \frac{1}{q^j}(\partial^\mu A^\nu + \partial^\nu A^\mu), \tag{2.9}$$

where A^μ is a space-time vector. The results resemble the structure of the clockwork gearing, solving the eigenvalues of the mass matrix provide a massless graviton and heavy gravitons with integer mass modes n. Thus, the mass of clockwork graviton has similar form with the clockwork scalar, given by

$$m_0 = 0, \quad m_n^2 = k^2 + \frac{n^2}{R^2}, \quad n = 1, 2, 3, \cdots. \tag{2.10}$$

R represents the radius of the compactified dimensions discussed in section 2.2, and k is the Higgs-curvature which will be discussed in next section.

2.4 Clockwork under continuum limit

Similar to the ADD model [3, 31], Randall-Sundrum model [5], the clockwork model is a 5D theory characterized by an additional spatial dimension denoted by the coordinate y, ranging from $-\pi R$ to πR. Here, R represents the radius of the compactified dimension. In the clockwork model, the space is wrapped to maintain symmetry. The general 5D metric can be written as:

$$ds^2 = X(|y|)dx^2 + Y(|y|)dy^2 \ , \ dx^2 = -dt^2 + d\vec{x}^2. \tag{2.11}$$

The action for a real massless scalar field is the generalized form of the Einstein-Hilbert action,

$$\begin{aligned}
\mathcal{S} &= \int_{-\pi R}^{\pi R} dy \int d^4x \sqrt{-g}\left(-\frac{1}{2}g^{MN}\partial_M\phi\partial_N\phi\right), \\
&= -\int_0^{\pi R} dy \int d^4x X^2 Y^{1/2}\left[\frac{(\partial_\mu\phi)^2}{X} + \frac{(\partial_y\phi)^2}{Y}\right], \\
&= -\int_0^{\pi R} dy \int d^4x \left[(\partial_\mu\phi)^2 + \frac{X^2}{Y^{1/2}}\left(\partial_y \frac{\phi}{X^{1/2}Y^{1/4}}\right)^2\right],
\end{aligned} \tag{2.12}$$

where the M, N are the 5D indices. In the theory space of the extra dimension, extra dimension is discretized into N points with lattice spacing a, y becomes $y_j = ja$ for $j = 0, ..., N$, such that $Na = \pi R$. The action which corresponds to Lagrangian in Eq. 2.8 after rescaling can be rewritten as

$$\mathcal{S} = -\frac{1}{2}\int d^4x \left[\sum_{j=0}^{N}(\partial_\mu\phi_j)^2 + \sum_{j=0}^{N-1} m_j^2(\phi_j - q_j\phi_{j+1})^2\right] \tag{2.13}$$

$$m_j = \frac{N^2 X_j}{\pi^2 R^2 Y_j}, \quad q_j = \frac{X_j^{1/2}Y_j^{1/4}}{X_{j+1}^{1/2}Y_{j+1}^{1/4}}. \tag{2.14}$$

The clockwork framework constrains the mass of mode j constant, $m^2 = \frac{N^2}{\pi^2 R^2}$, the asymmetry scale q remains y-independent and q^N gives the limit of the clockwork mechanism in infinite spacing limit $q^N = e^{k\pi R}$. The parameter k is Higgs-curvature also called the 'clockwork spring' and measures the curvature of the wrapped metric. In the case of flat space-time with $X = Y = 1$, then $k = 0$. The only choice for X and Y is

$$X_j \propto Y_j \propto e^{-\frac{4k\pi Rj}{3N}}, \tag{2.15}$$

It is important to clarify that m^2 does not represent the mass of a specific mode, but rather a mass scale generated by the clockwork model for mode j. Notably, the mass scales at any j are identical. To determine the mass of the particle, substitute m^2 and $q = e^{k\pi R/N}$ into the mass matrix. In the large limit of N, the excitations of the clockwork graviton are obtained as in Eq. 2.10. Also in the continuum limit $N \to \infty$, the metric of the clockwork space in Eq. 2.11 becomes

$$ds^2 = e^{\frac{4k|y|}{3}}(dx^2 + dy^2). \tag{2.16}$$

The mass of the clockwork graviton depends on the clockwork spring constant k and the compactification radius R. These two parameters decide the scales and the curvature of the 5D space where the clockwork model lives. All the phenomenology of the theory can be determined from the parameters. They will be our primary focus in the searches. Again this metric is obtained from continuum limit, and has the same form as the LD metric which is given by $ds^2 = e^{-\frac{2}{3}\alpha|z|}(dx^2 + dy^2)$, where α is a proportional constant to ensure the 5D curvature is smaller than the fundamental scale, and z is the extra dimension.

In addition, there are a similar KK excitation states, with a mass spectrum given by $m_n^2 = \frac{\alpha^2}{4} + (\frac{n\pi}{r_c})^2$ where r_c is the compactification radius similar to the R in the clockwork model. The theoretical results from LD have their correspondents in clockwork model, differ only by the scales [13]. Therefore, KK mode and dilaton modes will not be discussed in the following sections, the result of the thesis, particularly the limit of k and M_5, can be easily translated to other models.

Chapter 3

CW/LD graviton phenomenology

This chapter discusses the phenomenology of the CW/LD gravitons. In the following discussion, the term graviton shall unambiguously denote the CW/LD graviton unless it is massless. We address the kinematics of the gravitons production processes and decay properties. We also explore a characteristic which may be seen in the decay channels, where a high-mass graviton decays into two lower-mass gravitons. If kinematically feasible, these lower-mass gravitons can further decay into yet lighter mass gravitons. This process is denoted as a cascade of decay. The physics phenomenology at different values of (k, M_5, R) and the impact of the cascade of decay are demonstrated.

The clockwork graviton's model can be simplified into a function of two independent variables (k, M_5). The radius of the extra dimension R can be determined by the hierarchy relationship with an approximation [17]

$$kR \approx \frac{1}{\pi} \ln \left(\frac{M_P}{M_5} \sqrt{\frac{k}{M_5}} \right). \tag{3.1}$$

In order for the approximation in the hierarchy relationship to hold, it is necessary for the quantity kR to be significantly larger than unity, this can be satisfied by careful choice of (k, M_5). The relationship reduces the undetermined parameters from three to two, which simplify the analysis. The ultimate goal for this search is to determine the values of (k, M_5) if gravitons are produced in the ATLAS detector. Here (k, M_5) are chosen instead of (k, R) or (k, M_5) because R can be conveniently expressed as dependent variable through Eq. 3.1, and (k, M_5) are algebraically independent. There are constraints to the range of validity of (k, M_5). By the data obtained from the beam dump experiment, supernova emission and nucleosynthesis, the lower limit on k is 10 MeV to 1 GeV [32]. The limit spans across three orders of magnitude because of the inherent uncertainty in the observations. There are no upper limits to k. The M_5 is not limited, but the range of validity is set by [22]

$$m_n \lesssim 6.8 \left(\frac{k}{M_5} \right)^{1/7} M_5, \tag{3.2}$$

where m_n is the invariant mass of a graviton. Under this condition, KK excitations, which represent the four dimensional spacetime manifestation of quantized KK modes within higher dimensional framework, can be treated as individual resonances. These excitations, emerging from the occupation of specific KK modes by the gravitational field, exhibit distinct resonance properties in our observable universe. Otherwise the decay width becomes too wide and overlaps with other excitations. The model enters non-perturbative regime when $k > M_5$.

3.1 Cross-section

The cross-section $\sigma_G^{(n)}$ for graviton production of different mass modes n and (k, M_5) can be determined from the interaction strength $\Lambda_G^{(n)}$, which is the coupling strength of the clockwork graviton to the SM particles. The masses at different mass modes are given by Eq. 2.10 and reiterated below for convenience.

$$m_0 = 0, \quad m_n^2 = k^2 + \frac{n^2}{R^2}, \quad n = 1, 2, 3, \cdots. \tag{3.3}$$

$\Lambda_G^{(n)}$ and $\sigma_G^{(n)}$ are given by

$$\Lambda_G^{(0)2} = M_P^2, \quad \Lambda_G^{(n)2} = M_5^3 \pi R \left(1 + \frac{k^2 R^2}{n^2} \right) = M_5^3 \pi R \left(1 - \frac{k^2}{m_n^2} \right)^{-1} \tag{3.4}$$

and

$$\sigma(pp \to G_n) = \frac{\pi}{48\Lambda_G^{(n)2}} \left(3\,\mathcal{L}_{gg}(\hat{s} = m_n^2, Q^2 = m_n^2) + 4 \sum_q \mathcal{L}_{q\bar{q}}(\hat{s} = m_n^2, Q^2 = m_n^2) \right), \tag{3.5}$$

where

$$\mathcal{L}_{ij}(\hat{s}, Q^2) = \frac{\hat{s}}{s} \int_{\frac{\hat{s}}{s}}^{1} \frac{dx}{x} f_i(x, Q^2) f_j(x, Q^2) \left(\frac{\hat{s}}{xs} \right), \tag{3.6}$$

the $\mathcal{L}_{ij}$ is the parton luminosity with $i, j = q\bar{q}$ or gg, Q^2 is the QCD resolution scale, characterized by the square of the invariant mass of the virtual particle transmitted which is the graviton. The parameter $\hat{s}$ is square of the invariant mass involved in the partons collision, similarly s is the square of invariant mass involved in the initial hadron collision rather than the partons. The parameter x is the energy fraction carried by the parton relative to the hadron. Parton luminosity is the probability of finding partons i and j collide given certain amount of energy. It helps physicists predict the occurrence of particle reactions, based on the energy fractions carried by these partons.

To reduce the complexity of the simulation, The narrow-width approximation [33] of the graviton width is applied to Eq. 3.5. Gravitons are regarded as having single mass value at each mass mode, and the decay width is negligible compared to the mass value. It is justified by the calculation (in section 3.2) that the $\Gamma/M = \mathcal{O}(10^{-3})$ where Γ is the decay width, and M is the mass of the graviton. Fig. 3.1 shows two example of plots of the narrow-width approximated cross-section of the graviton at different mass modes n for $(k, M_5) = (2, 2)$ TeV and $(1, 6)$ TeV. The cross-section plots for other choices of (k, M_5) used are attached in the Appendix A.

The distributions have three distinguishing properties that provide insight for our search methods. Firstly, there are multiple peaks one for each mass modes n, implying a pattern of oscillation in the mass spectrum when we study their decay products. Secondly, the mass of the graviton of the smallest mode is approximately equals to k ($m_1 \approx k$), which sets the lowest mass of the search in the mass spectrum for each

k. Thirdly, the gap between the peaks differs for each k, narrower gaps are expected for smaller k, and vice versa. A unique frequency is assigned to each value of k. Combining the oscillation pattern, unique range and unique frequency properties, the gravitons of different values of (k, M_5) have unique signal spectrum that can be extracted by a Fourier transform analysis with the frequency space slight amended, this will be discussed in Ch. 7. The graviton production in LHC are limited to $gg \to G$ and $q\bar{q} \to G$ which are the two possible s-channel subprocesses. The Feynman diagrams for the production are shown in Fig. 3.2. If the model is realized, there will be only one k value and one M_5 value.

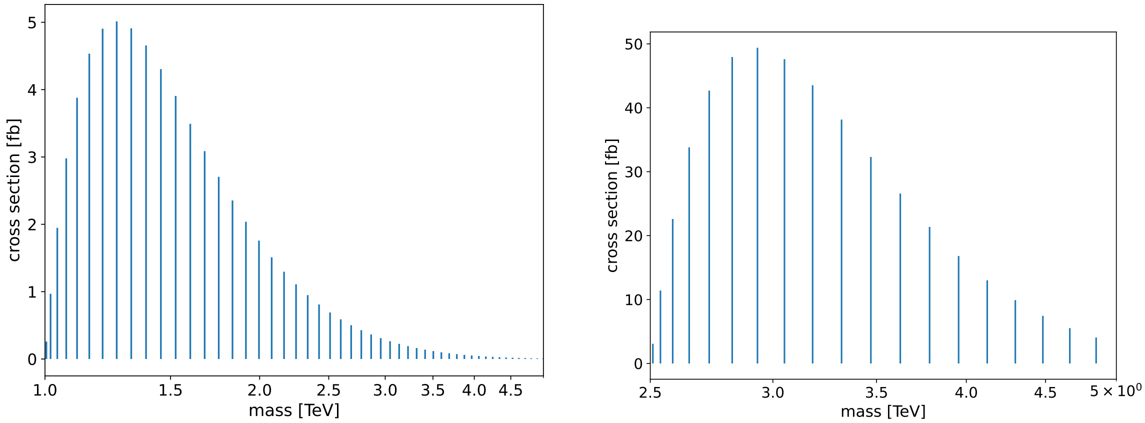

(a) $k = 1$ TeV, $M_5 = 6$ TeV

(b) $k = 2.5$ TeV, $M_5 = 1$ TeV

Figure 3.1: The cross-section of the gravitons at different masses with two chosen (k, M_5) models. Narrow-width approximation is applied.

3.2 Decay width and branching ratio

The gravitons decay into SM particles, or other gravitons with smaller mass modes, KK scalars and dilatons. Those decay into SM particles and smaller graviton are the interest of this thesis, the rest are omitted because their maximum contribution to the decay widths combined is two orders of magnitude smaller than the SM contribution, and drops to seven order of magnitude difference at the TeV scale [22]. The contribution SM cascade decay, which is the decay of a graviton into two SM particles, and

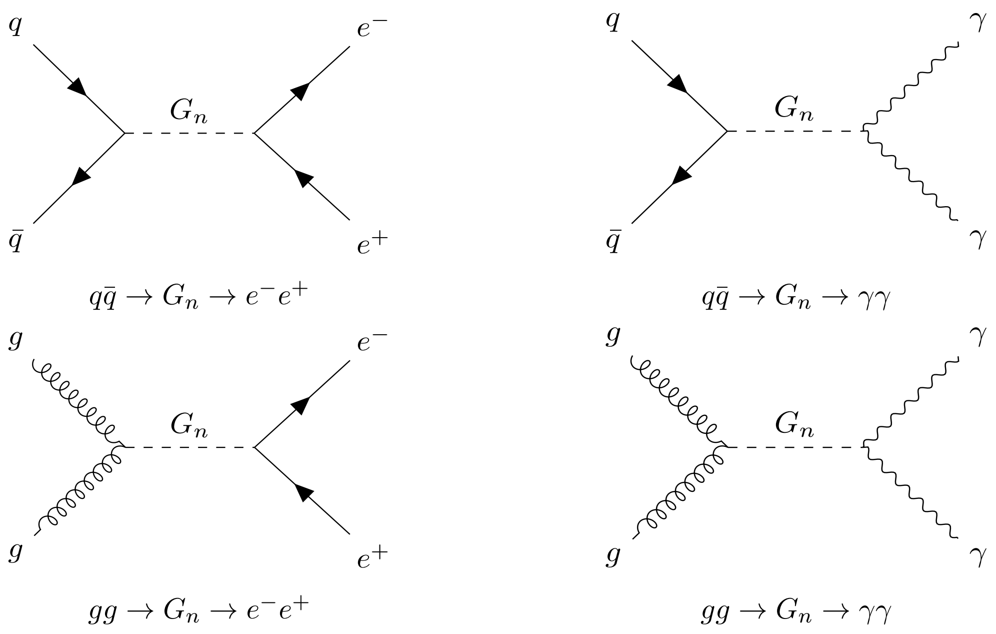

$q\bar{q} \to G_n \to e^- e^+$ $q\bar{q} \to G_n \to \gamma\gamma$

$gg \to G_n \to e^- e^+$ $gg \to G_n \to \gamma\gamma$

Figure 3.2: The Feynman diagrams for the graviton production and decay processes, G_n represents the n-th graviton mass mode.

SM particles further decay into other SM particles are ignored. The decay width of the graviton depends on their masses, that is, depends on mass mode n, and (k, M_5). The possible partial SM decay width Γ_{SM} are listed below [34]:

$$\Gamma_{\gamma\gamma} = \Gamma_0, \quad \Gamma_{gg} = 8\Gamma_0, \tag{3.7}$$

$$\Gamma_{ZZ} = \frac{1}{2}\left(\frac{13}{6} + \frac{7}{3}x_Z + \frac{1}{2}x_Z^2\right)(1 - x_Z)^{1/2}\,\Gamma_0, \tag{3.8}$$

$$\Gamma_{W^+W^-} = \left(\frac{13}{6} + \frac{7}{3}x_W + \frac{1}{2}x_W^2\right)(1 - x_W)^{1/2}\,\Gamma_0, \tag{3.9}$$

$$\Gamma_{hh} = \frac{1}{12}(1 - x_h)^{5/2}\,\Gamma_0, \tag{3.10}$$

$$\Gamma_{f\bar{f}} = \frac{N_f}{2}\left(1 + \frac{2}{3}x_f\right)(1 - x_f)^{3/2}\,\Gamma_0, \tag{3.11}$$

where,

$$x_i = \frac{4m_i^2}{m_n^2}, \quad \Gamma_0 = \frac{m_n^3}{80\pi\Lambda_G^{(n)2}}, \tag{3.12}$$

where x_i is a dimensionless quantity, with m_i as the mass of the SM daughter. The factor $(1 - x_i)$ is a kinematic threshold factor for the decay. Here $N_f = 3$ for each quark, 1 for each charged lepton and 1/2 for each (Majorana) neutrino. The decay widths are the leading order predictions of properties of spin-2 particles [34] and do not relate to any model other than spin and angular momentum rules. The graviton's exact mass values are used for the kinematic thresholds to determine if the decay is allowed. For the CW/LD model, the coupling strength is replaced with $\Lambda_G^{(n)}$ from Eq. 3.4. The mass to total decay width ratio is shown in Fig. 3.3. Only $M_5 = 1$ TeV and $M_5 = 6$ TeV are shown as examples, the decay width of other M_5 values are in between the two. A high mass to decay width ratio indicates a distinct resonance. A sharp resonance is easier to identify and analyze in experiments because it stands out clearly from the background. Also, the graph validates the usage of narrow-width approximation in the cross-section calculation. The narrow-width approximation starts failing when M_5 becomes small or k becomes large. However, it is applicable for all (k, M_5) of interest here.

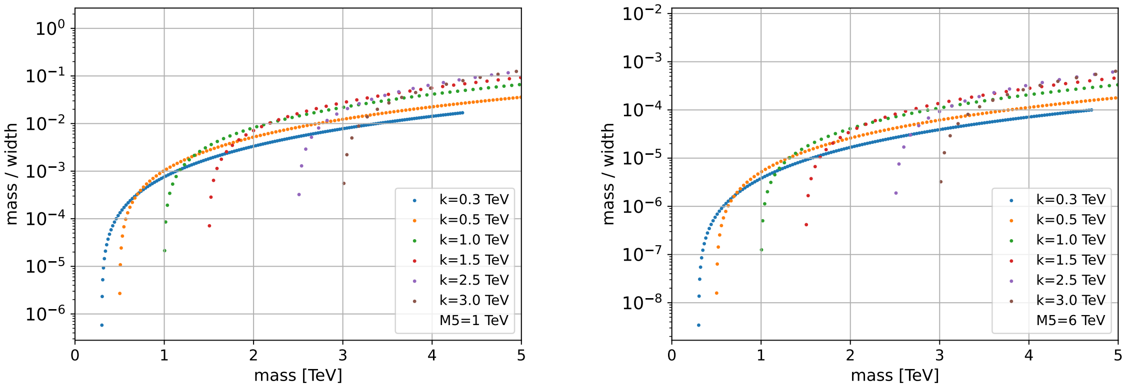

(a) $M_5 = 1$ TeV (b) $M_5 = 6$ TeV

Figure 3.3: The mass to total decay width ratio of the graviton at different mass.

We are particularly interested in the e^+e^- decays and $\gamma\gamma$ decays, which are the most promising channels for the search of the graviton. The e^+e^- and the $\gamma\gamma$ channels are considered to be the cleanest due to their favorable signal-to-background ratio upon the completion of rigorous data analysis, and the high energy resolution of the ATLAS detector. The gg and the $q\bar{q}$ channels were not chosen despite their high branching ratio because there are significant QCD background contribution make it difficult to distinguish a new physics signal from the SM. It was found that in the dijets studies, either the discriminating power of signal and background decreases at low dijets invariant mass or the dijets invariant mass is too high and is beyond the mass range of distinguishable KK resonances [22]. Despite the nature of $\mu^+\mu^-$ being similar to e^+e^-, the resolution of the $\mu^+\mu^-$ is typically less precise due to the different interactions with the detector material [7]. Also, around 10 times more background is anticipated in the W^+W^-, $\tau^+\tau^-$ channels due to the high SM production cross-section at high energy [35, 36]. The ZZ channel is not considered because each Z requires independent reconstruction via its decay product, leading to a multitude of possible decay product combination that must be considered in ZZ [21]. The Feynman diagram for the decay is shown in Fig. 3.2.

We ought to study a phenomenology that is universal across different values of (k, M_5). The ratio of the graviton SM daughter decay width to the decay width of graviton to $\gamma\gamma$ is dependent on x_i, the dimensionless quantity Γ_{SM}/Γ_0 against x_i do not explicitly depends on the choice of (k, M_5). It is a kinematic property of the gravitons, the decay product masses and the number of flavor of the decay products. It is shown in Fig. 3.4. The ratio hits the massless limit when $x_i = 0$. The same ratio but against the invariant mass of mother graviton m_i is shown in Fig. 3.5. Firstly, the decay width of Z is one half of that of the W bosons since there are one extra permutation for the W bosons decay process; and the ratio of $\ell\bar{\ell}$ is one third of $q\bar{q}$ since there are two extra color permutations for the $q\bar{q}$ decay process. Secondly, there are two extreme cases that are interesting, the first is the case where the graviton is very heavy, where $m_n \gg m_i$ and $x_i \ll 1$; the second is the case where the graviton is close to half of the mass value of the daughter particle, where $m_n \approx 2m_i$ and $x_i \approx 1$. In addition, the decay width of gg products is the largest, and is a constant value 8 throughout all x_i according to Eq. 3.7. Most of the massive gravitons are much heavier than the SM particles, for most of the mass modes of interest the x_i values for

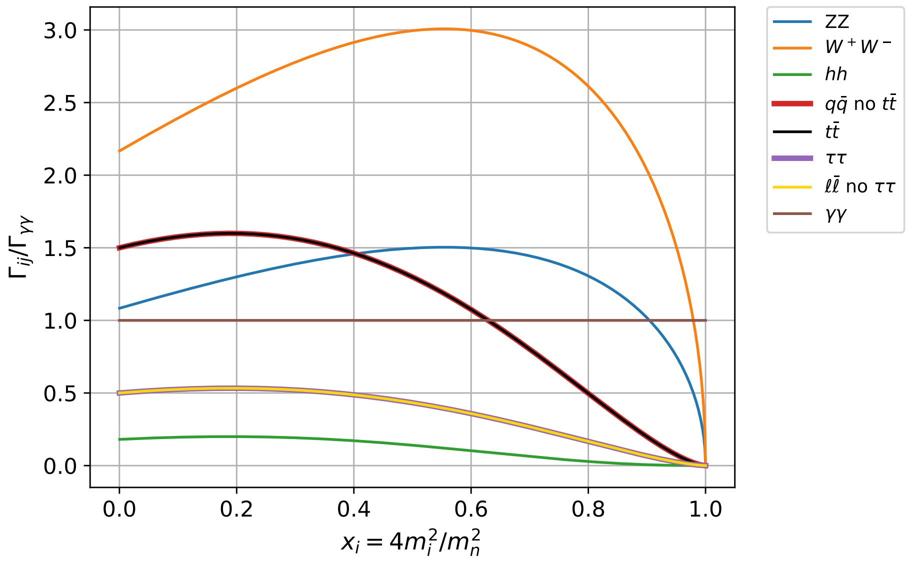

Figure 3.4: The ratio of SM daughters decay width to the decay width of $\gamma\gamma$ against x_i. Γ_{ij} is the decay width of process $G \to ij$. $G \to gg$ is not shown, but it is a constant of 8 throughout all x_i. All the massive particles only asymptotically approach $x = 0$, but it cannot be shown on the graph.

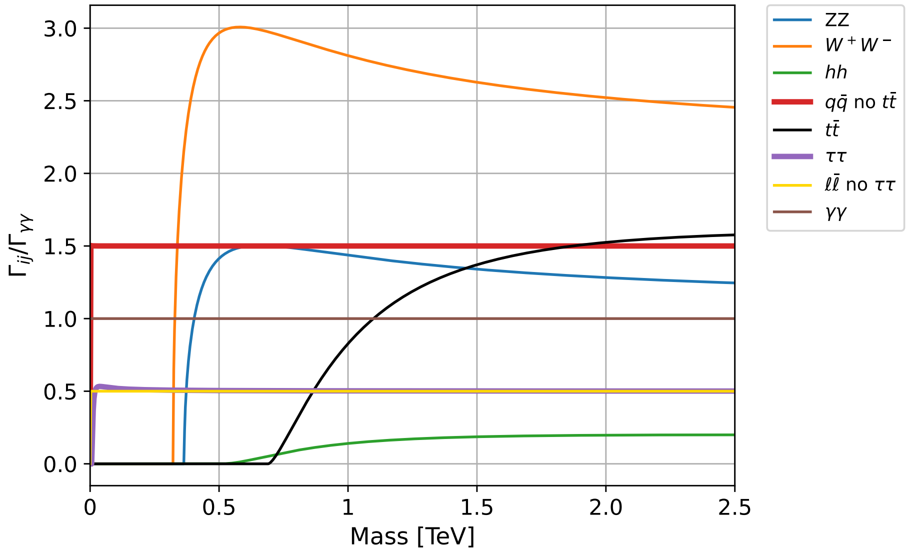

Figure 3.5: The ratio of SM daughters decay width to the decay width of $\gamma\gamma$ against the graviton mass. $G \to gg$ is not shown, but it is a constant of 8 throughout all masses.

whatever choice of (k, M_5) concentrates around the beginning of the plot, and having a constant ratio when increasing the mass modes or the mass values. Conversely, when the graviton mass values are close to the minimum energy to create a massive di-product, the ratio truncates to 0 because it is not kinematically allowed. It can be seen that in Fig. 3.5 the ratio for all channels except $t\bar{t}$ and W^+W^- are achieving a plateau after 2 TeV, which is above the invariant mass of $t\bar{t}$ pair.

So far we discussed only the SM particles decay widths, now we discuss the graviton decay into gravitons. The full decay width also includes the decay channels that graviton of higher mass mode decay into two smaller mass modes, the possible daughter combination are constrained by the daughters' invariant masses. The process is denoted as $G_n \to G_m G_l$ with n, m, l integers and $n > m \geq l$. The decay amplitude for $G_n \to G_m G_l$ is an integral over the wave functions in the 5D metric, and will be used to calculate the $G_n \to G_m G_l$ decay width $\Gamma_{G_m G_l}$.

$$I_{nml} = 2\int_0^{\pi R} dy e^{2ky} \psi_n(y)\psi_m(y)\psi_l(y) \tag{3.13}$$

$$= \frac{32}{R^3} \frac{k(nm_n)(mm_m)(lm_l)}{m^2_{l+m-n} m^2_{l-m+n} m^2_{m+n-l} m^2_{l+m+n}}. \tag{3.14}$$

The scattering amplitude I_{nml} is symmetrical under the permutations of the labels. It also depends on (k, M_5) through the mass terms.

The massive graviton has 5 spin states. In 3 space dimensions, there are $5^3 = 125$ physically distinct helicity amplitudes. They can be simplified into 4 distinctive analytical forms A_j. The norm of the amplitude over the azimuthal angle can be expressed analytically as a function of dimensionless amplitudes x and y [22]:

$$A_1^2(x, y) = \frac{2[x(1 + y^2) - 2]^2}{3(x^2 - y^2)} \tag{3.15}$$

$$A_2^2(x, y) = \frac{2[y^2 - 2y(1 + x) + 3]^2}{x - y} \tag{3.16}$$

$$A_3^2(x, y) = \frac{8[2x^2 + 2xy + (1 + y)^2]^2}{3(x + y)^2} \tag{3.17}$$

$$A_4^2(x, y) = \left[\frac{6 - 4x + x^2 + 2x^3 + y^4 + y^2 x(5x - 6) - 5y^2}{9(x^2 - y^2)}\right]. \tag{3.18}$$

And the overall amplitude A_T is expressed as

$$A_T^2(n, m, l) = \frac{I^2_{nml}}{5(M_5 \pi R)^3} \sum_{cyc} m_n^4 \sum_{j=1}^{4} A_j^2 \left(\frac{m_l^2 + m_m^2}{m_n^2}, \frac{m_l^2 - m_m^2}{m_n^2}\right). \tag{3.19}$$

The factor 1/5 is for averaging initial polarizations, and the cyclic summation over three permutations. The decay width for $G_n \to G_m G_l$ is

$$\Gamma_{n \to m,l} = \frac{|\mathbf{p}_m|}{16\pi m_n^2} A_T^2(n, m, l), \tag{3.20}$$

where $|\mathbf{p}_m|$ is the magnitude of the daughter momentum, and is identical to $|\mathbf{p}_l|$ in the center of mass frame. It can be easily determined through $1 \to 2$ decay process

$$|\mathbf{p}_m|^2 = \frac{(m_n^2 - (m_m - m_l)^2)(m_n^2 - (m_m + m_l)^2)}{4m_n^2}. \tag{3.21}$$

The only constraint on the decay is $m_n \geq m_m + m_l$: the sum of the mass of the daughter particles cannot exceed the mass of the mother particle. A massive graviton decays into two massless gravitons is forbidden, even though it satisfies the conservation of energy. A massless graviton is spin-2 and the helicity of a massless particle must be the maximal-magnitude of its spin, which is ± 2. The daughter massless gravitons must have opposite helicity to each other because they are identical particles. In addition, by the conservation of parity, one can derive that a mother particle with even angular momentum J is able to decay into opposite helicity particles if and only if $J \geq 2s$ where s is the spin of the daughter particles [37]. Decaying into photons is allowed if the graviton has $+1$ intrinsic parity because $s = 1$ for photons and $J \geq 2s$ is satisfied. Contrarily, a decay into two massless gravitons with $s = 2$ is forbidden if parity is conserved.

The total decay width can also be determined after finding all the possible combinations of $G_n \to G_m G_l$. That is, $\Gamma_{tot} = \Gamma_{SM} + \Gamma_{\sum_{(G_m, G_l)}}$. Fig. 3.6 shows the decay widths of all possible SM decay channels with various k, thus the cumulative width for $G_n \to G_m G_l$ as n increases. Other plots for decay widths for other choices of (k, M_5) used are attached in the Appendix B. The cumulative width is 0 before the first mass mode that the corresponding mass is sufficient to decay into (G_1, G_1). In addition, it is comparable to the SM channels decay widths in higher mass modes and should be taken into account in simulations. The effects of such kind of decay are discussed in Sec.3.2.

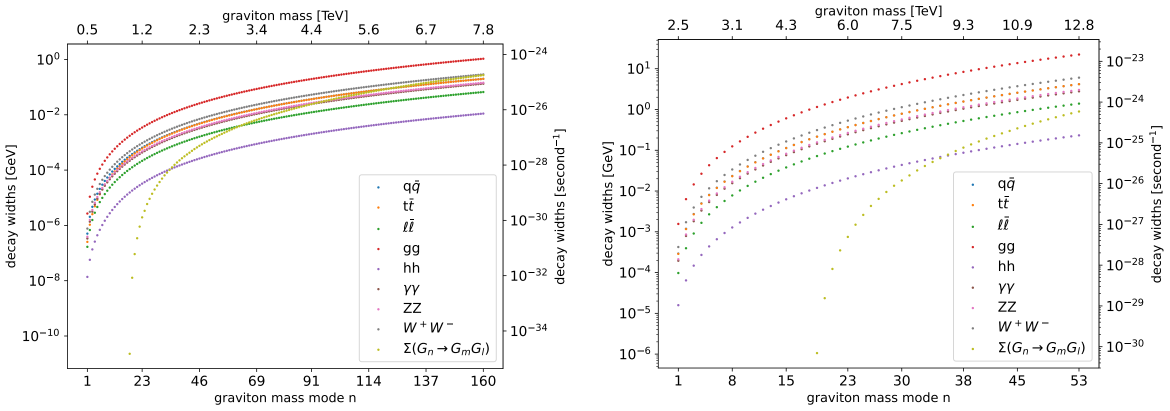

$k = 0.5$ TeV $\quad M_5 = 6$ TeV

$k = 2.5$ TeV $\quad M_5 = 6$ TeV

Figure 3.6: The decay widths of possible decay channels, including the cumulative widths of all $G_n \rightarrow G_m G_l$. Note that the decay width for $t\bar{t}$ is slightly smaller than that of the other quark pairs. However, it is merged into $q\bar{q}$ because the difference is indistinguishable in the plot. Also note that the mass mode axis (bottom) is plotted linearly result in non-linear mass axis (top).

The branching ratio which is given by Eq. 3.22. There is no guarantee that the branching ratio remains the same across different mass modes n, and (k, M_5).

$$BR(G_n \rightarrow XX) = \frac{\Gamma_{XX}}{\Gamma_{tot}}, \tag{3.22}$$

where XX denoted the interested SM channel. Fig. 3.7 shows the branching ratio of various (k, M_5) across different mass modes. We separated $t\bar{t}$ from other quark pairs because the difference in branching ratio is more observable unlike in the decay width. At lower k or lower mass mode, the graviton mass-energy is insufficient to decay into $t\bar{t}$, where a single t has mass 172.69 GeV[21]. The factor $(1 - x_f)^{3/2}$ in Eq. 3.11 does not approach 1 as for other quarks as the graviton mass is comparable to the $t\bar{t}$, result in a deviation of the decay width. This deviation is greatly reduced at higher mass mode or at higher k, the branching ratio of $t\bar{t}$ eventually approximately equals to that of other quarks. In addition, Fig. 3.7 also shows that the overall SM branching ratio is decreasing across the mass modes because the cumulative $G_n \rightarrow G_m G_l$ is becoming more dominant. Branching ratio plots for other choices of (k, M_5) are in Appendix C.

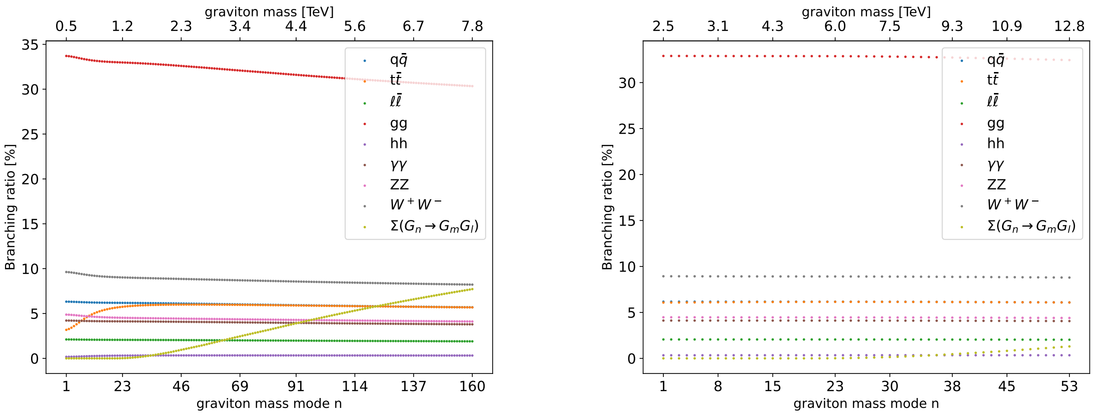

$k = 0.5$ TeV $\quad M_5 = 6$TeV

$k = 2.5$ TeV $\quad M_5 = 6$ TeV

Figure 3.7: The branching ratio of SM decay channels based on Eq. 3.22, the cumulative width of all $G_n \to G_m G_l$ is included in total width. The difference between the branching ratio of $t\bar{t}$ and that of the other $q\bar{q}$ states is observable in lower energy, that is, at lower k and lower mass modes.

3.3 Cascade decay

Unlike the particles in SM, where a particle possesses only a single mass value within the range of their decay width. Gravitons have different masses, but still each graviton has a single mass value with the decay width about it's mass. Additionally, gravitons of higher mass mode can decay into lower mass modes, according to the decay width stated in Eq. 3.20. This leads a phenomenon called cascade decay, where a higher mass mode graviton decays into two lower mass modes, and the resulting daughter gravitons may further decay into SM particle pairs, or into gravitons of even lower mass.

As an illustration, consider a hypothetical scenario where a 54^{th} mass mode graviton (G(54)) with $(k = 1, M_5 = 6)$ TeV is simulated. This graviton may decay into either a pair of SM particles or two lower mass mode gravitons, such as $G(27)$ and $G(3)$. The $G(27)$ would then undergo further decay into a pair of SM particles or two lower mass mode gravitons, and so on. When examining the invariant mass spectrum in the e^+e^- channel after all gravitons decay into SM particles, we anticipate detecting more lower-mode gravitons and fewer higher-mass mode gravitons.

To date, this effect has only been studied through simulations. Here, we present an analytical method for calculating the cascade decay effect. We express the effect in discrete sets within the mode space, enabling a comparison between the number of gravitons in different modes, including and excluding the cascade decay effect. By using a clockwork model with (k, M_5) parameters and focusing on the first n modes, The distribution is discrete and is described by $\mathcal{N} = [N_1, N_2, \cdots, N_n]$, where N_i is the fraction of counts and should match the values of the cross-section in the mode space. One can interpret $\mathcal{N}$ as counting. The value of n can, in fact, be an arbitrary large number. The cascade decay effect contributed by a particular mode, however, depends on the cross-section of that mode. Since the cross-section of gravitons at higher mass is smaller than that of the graviton at lower mass, we can safely assume that the number of gravitons created at higher mass is negligible and focus on the first n modes, where n is a finite number. Nevertheless, it is important to note that the possibility of n being indefinite implies that the cascade decay effect could, in principle, continue indefinitely, with gravitons decaying into even lower mass modes. While this might be mathematically plausible, in practice, the n is limited by the center of mass energy of the LHC. By concentrating on the first n modes within LHC center of mass energy, we can still capture the essential features of the cascade decay effect and gain valuable insights into the properties of gravitons and their decay processes.

It is crucial to distinguish between the production and decay processes of gravitons; the former is governed by the cross-section, while the latter affects the subsequent distribution of gravitons. Changing cross-section would involve introducing new Feynman diagrams in the production process, which is not the case here. Cascade decay is merely a decay process that changes the distribution of gravitons. Our focus lies on the changes in the number of gravitons at different modes after the cascade decay, as well as comparing this with the nominal case where all gravitons are created at parton collisions and decay to SM particles. The analytical method presented here allows us to investigate the cascade decay effect. By analyzing the changes in graviton number in each mode and the invariant mass spectrum, we learn the underlying decay processes of gravitons, thus obtaining the relative probability of detecting gravitons of different mass modes.

We do not consider the SM cascade decay in which gravitons decay into high mass SM daughter pairs ($t\bar{t}, b\bar{b}, ZZ, W^+W^-$, etc.) that further decay into e^+e^- and $\gamma\gamma$. This contributes to the potential signals has been ignored in this analysis.

We first calculate the number of counts N_n that decays into gravitons instead of SM particles using $\delta N_n = N_n \times \frac{\Gamma_{GG}}{\Gamma_{SM+GG}}$, and there will be $2 \times \delta N_n$ gravitons of lower mass modes created. We focus on the contribution of δN_n to N_m, where $n > m$, which is the sum of the probability that the $G(n)$ decays into $G(m)$ and $G(l)$ where l can be any other mode as long as we avoid double counting and kinematically allowed decays, written as:.

$$\delta N_m(n) = \delta N_n \left[\sum_l \theta(m_n - m_m - m_l) \frac{\Gamma_{G_n \to G_m G_l}}{\Gamma_{GG}} + \theta(m_n - 2m_m) \frac{\Gamma_{G_n \to G_m G_m}}{\Gamma_{GG}} \right]. \tag{3.23}$$

Here $\delta N_m(n)$ is the contribution to mode m by mode n. This formula includes a Heaviside step function, $\theta(x)$, to constrain kinematics and an additional term to account for the possibility of $G(n)$ decaying into two $G(m)$ particles. The momentum fraction is unimportant and not included in the step function. There are no limitation to l because the step function ensures that non-trivial contribution can only be achieved when the invariant mass of the daughter particles is less than the mass of the mother particle. Implicit constraint to l is applied. Since decays only goes from higher mode to lower mode, thus is a recursive process. The cascade decay is a recursive process, we iterate from $i = n$ to $i = m$ to obtain the final result. However, the counts in N_{n-1} to N_{m+1} are no longer the same due to contributions from N_n and modes $i > m + 1$, respectively. The analytical deduction can be expressed as the following recursive procedure. The updated contribution by mode j is simply the updated total number N'_j of mode j, which is given by

$$\delta N'_j = N'_j \times \frac{\Gamma_{GG}}{\Gamma_{SM+GG}}. \tag{3.24}$$

To obtain the updated N'_j, we sum over all the updated contributions from modes i to mode j where $i > j$, to obtain the total contribution to mode j.

$$N'_j = N_j + \sum_{i>j}^{n} \delta N'_j(i). \tag{3.25}$$

Again, $\delta N'_j(i)$ is the updated contribution to mode j by mode i. It has the same form as Eq. 3.23

$$\delta N'_j(i) = \delta N'_i \left[\sum_l \theta(m_i - m_j - m_l) \frac{\Gamma_{G_i \to G_j G_l}}{\Gamma_{GG}} + \theta(m_i - 2m_j) \frac{\Gamma_{G_i \to G_j G_j}}{\Gamma_{GG}} \right]. \tag{3.26}$$

The base case is $N'_n = N_n$ and $\delta N'_n = \delta N_n = N_n \times \frac{\Gamma_{GG}}{\Gamma_{SM+GG}}$. Through Eq. 3.24, Eq. 3.25 and Eq. 3.26, we can determine the changes in the shape of gravitons in mode space and the invariant mass spectrum after considering the (k, M_5) parameters.

The results show that the cascade decay effect is more significant at lower k values, the analytical results are shown in Fig. 3.8. Other plots for other choices of (k, M_5) are in Appendix D. The analytical results are compared with the MC simulations, which are generated with the same (k, M_5) parameters. The detail of the simulation procedure is presented in Ch. 6. The MC simulations are obtained by performing 10,000 pseudo-experiments of the cascade decay. At each mass there are blue dots forming ladder-like pattern. Each step corresponds to an extra graviton or missing graviton compare with the cross-section. Thus, a distribution of change in number of gravitons at each mass is obtained. A median and $\pm 1\sigma$ is fitted to the MC simulations to schematically show the distribution. One should note that a greater decrease in the number of gravitons at higher mass modes corresponds to greater number of gravitons at lower mass modes, which is challenging to show in the graph, and vice versa.

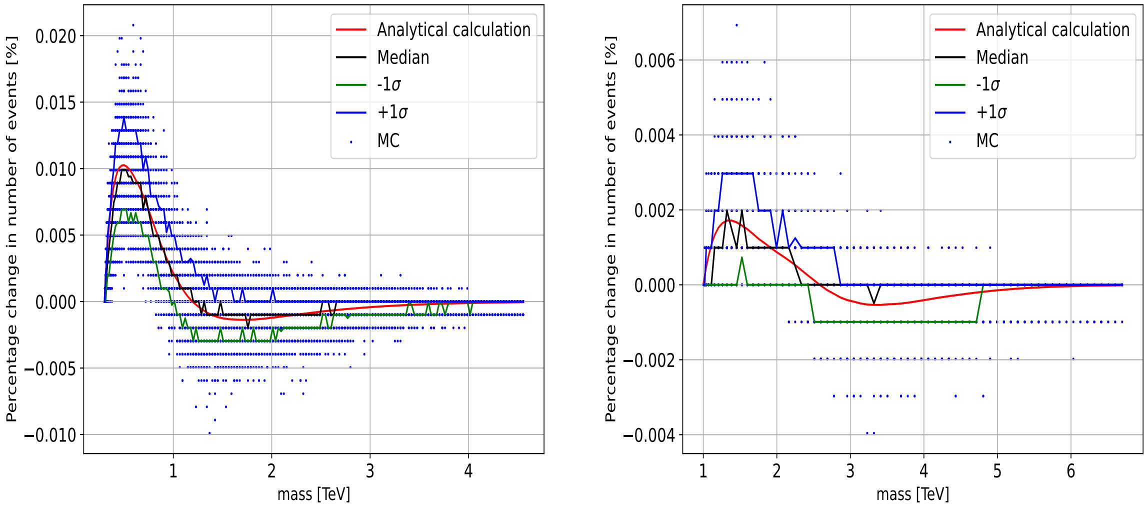

(a) $k = 0.3$ TeV $M_5 = 3.0$ TeV (b) $k = 1.0$ TeV $M_5 = 6.0$ TeV

Figure 3.8: The cascade decay effect contributed to the number of event of gravitons. The analytical result and the MC simulations are presented. The percentage changes are obtained through comparing the final counts of gravitons at each mode with the original total number of gravitons simulated.

We observe that the cascade decay effect is more pronounced at lower k values. The fractional changes generally follow a pattern in which a peak appears at the mode n just before the first possible $G(n)$ decays into $G(1)$ and $G(1)$, followed by a trough. The reason why the most significant changes are not observed at the minimum mass mode can be attributed to the amplitude equations Eq. 3.15. The amplitude squared of the decay process is proportional to the squared values of two parameters: $\frac{m_l^2+m_m^2}{m_n^2}$ and $\frac{m_l^2-m_m^2}{m_n^2}$. Greater amplitudes are obtained with larger parameters. The first parameter encourages the decay process to have greater m_l and m_m, while the second parameter promotes deviation between m_l and m_m. Taking both parameters into account, the decay process is more likely to have m_l and m_m close to m_n but deviating from each other. The minimum mode is not favored by the first parameter, and the cyclic sum reduces contributions from the minimum mode, explaining why the greatest changes are not observed at the minimum mass mode. The fractional changes eventually converge to 0 because the mass distribution of gravitons is dominated by the production cross-sections, which decrease at higher masses. Additionally, when

k is higher, the peak and trough positions deviate from each other, resulting in a plateau between them. Ultimately, the cascades will be implemented in simulation work to provide analysis results with completeness and a better understanding of gravitons.

Chapter 4

ATLAS detector

4.1 Large Hadron Collider

The Large Hadron Collider (LHC) is a 27 km circular particle collider operated by CERN located in Geneva, Switzerland. It creates high energy physics events. Undiscovered particles might be created by colliding two particles with TeV scale energy, thus beyond Standard Model (BSM) process could be produced. A process of interest generated a certain number of events, denoted as N_{event}, within a specific time period in the LHC collisions is given by:

$$N_{\text{event}} = L_{\text{int}}\sigma_{\text{event}}, \tag{4.1}$$

where L_{int} is the integrated luminosity representing the amount of collision data delivered over a period of time, and σ_{event} is the total cross-section. The LHC can produce proton-proton (pp), lead-lead ($Pb - Pb$), proton-lead ($p - Pb$) collisions for different physics studies [38], however, only pp data samples are used in this thesis. The collider now operates at a pp center of mass energy $\sqrt{s}$ of 13.6 TeV, but data in this thesis were collected at 13 TeV. As of the end of Run 2 of the LHC in the year 2015-2018, we obtained pp data sample corresponds to an integrated luminosity of 140 fb^{-1} with a relative uncertainty of 1.7 % after typical data-quality selections [39]. Energy and luminosity limit the ability to search for any BSM events, especially exotic events with relatively low production cross-section compare with SM events. In theory, large Poisson counting statistical fluctuations are expected when studying events with small cross-section. An overview of the layout of LHC is provided in Fig. 4.1.

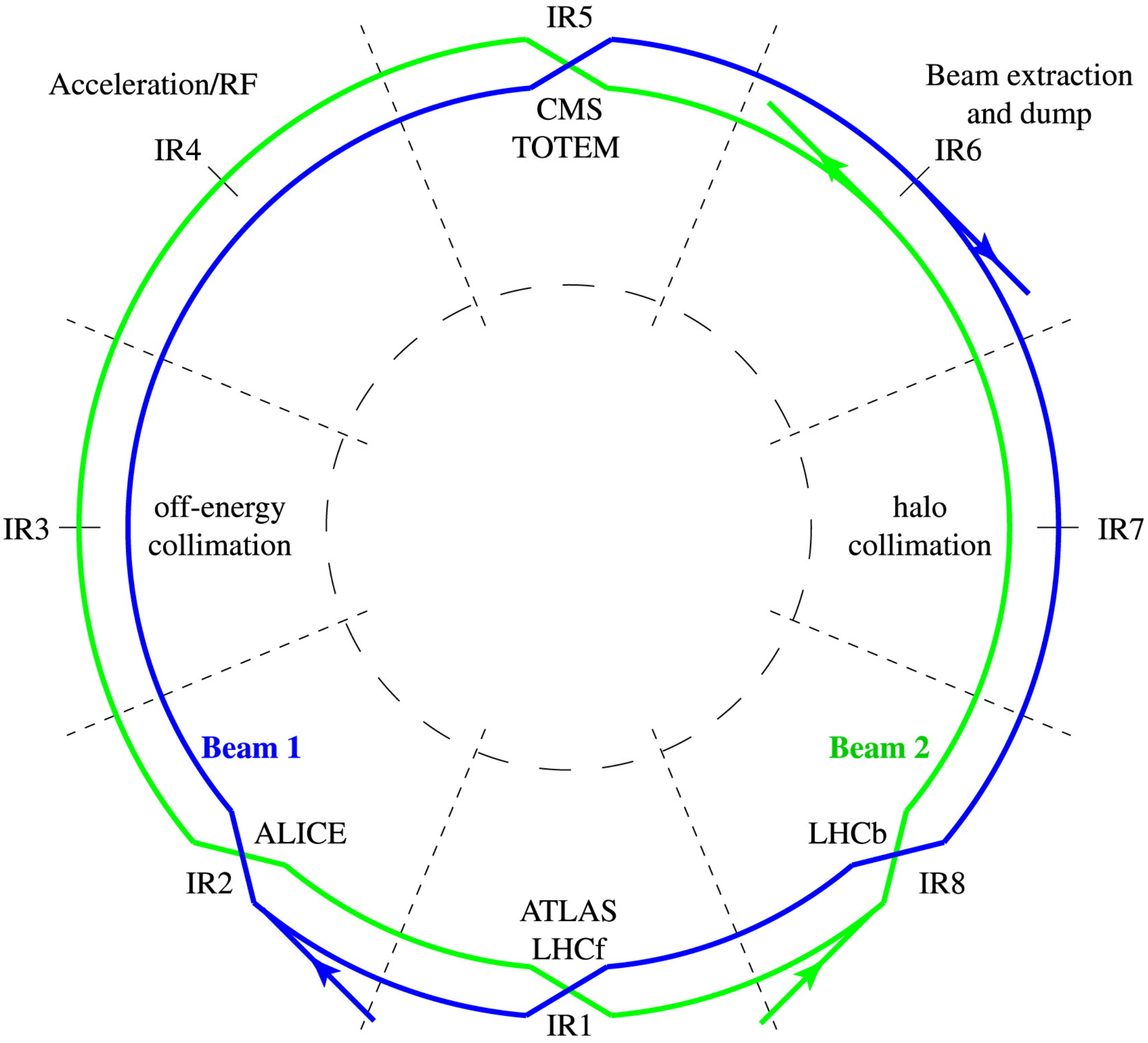

Figure 4.1: The layout of the LHC. Protons are accelerated in (anti) clockwise directions through the (green) blue path. Colliding at the intersections of the paths where detectors are located [40].

4.2 ATLAS Detector

A Toroidal LHC Apparatus (ATLAS) is a multipurpose detector to detect the outgoing particles produced by collisions in LHC [41]. It is designed according to a set of general requirements which originated from a few benchmark physics goal, including the searches for SM Higgs boson, new heavy gauge bosons W' and Z', decay of supersymmetric particles and quantum gravity. The detector is a cylindrical structure with a diameter of 25 m and a length of 44 m, weighting 7000 tons. The detector is composed of several sub-detectors, each of them is designed to measure the properties of different particles. The full details are reported in the technical report [42]. The tracker and the calorimetry provided us excellent quality data to study the electrons and photons we used. A cut-view of the ATLAS is provided in Fig. 4.2.

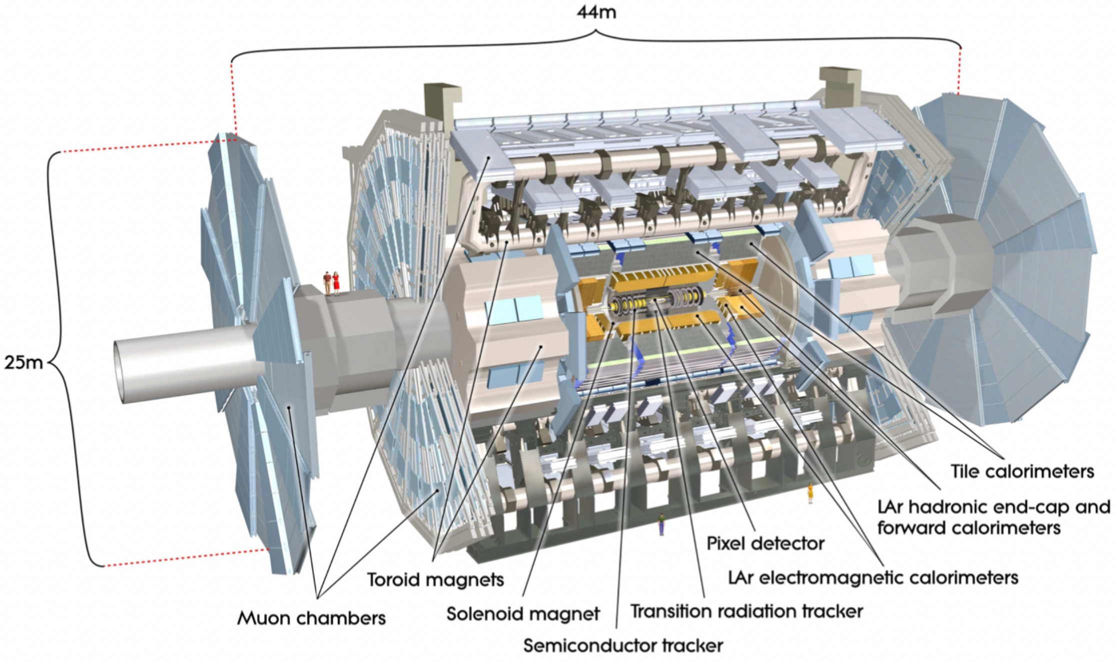

Figure 4.2: The cutview of the ATLAS detector [41]

.

4.2.1 Coordinate system in ATLAS

The analysis utilizes a right-handed cylindrical coordinate system (r, ϕ, z) to study the data. The origin of this coordinate system is at the center of the detector, coinciding with the nominal interaction point (IP) where the proton beams collide. In this system, the radial distance r is measured in the $x - y$ plane, perpendicular to the z-axis (beam axis), and represents the distance from the z-axis to a point in the detector. The positive z-axis is defined as the direction in which the beam circulates clockwise when viewed from the ground. The azimuthal angle ϕ ranges from 0 to 2π radians and is measured counterclockwise from the x-axis in the $x-y$ plane, describing the rotation around the z-axis. The polar angle θ ranges from 0 to π radians and is measured from the positive z-axis to the radial vector pointing towards the point of interest in the $r - z$ plane.

In the ATLAS experiment, a fundamental concept used in particle analysis is rapidity y, which is defined in terms of the energy E and the momentum along the z-axis p_z of a particle:

$$y = \frac{1}{2} \ln \left(\frac{E + p_z}{E - p_z} \right). \tag{4.2}$$

Rapidity is advantageous in particle physics as rapidity under a Lorentz boost along the beam axis adds a constant and therefore, the differences in rapidity between two particles are invariant. This invariance makes rapidity a valuable measure for analyzing particle collisions. However, calculating rapidity becomes challenging when a particle's momentum along the z-axis is comparable to its energy ($p_z \approx E$). In such scenarios, pseudorapidity η, serves as a more practical alternative. Pseudorapidity is defined as a function of the polar angle θ:

$$\eta = -\ln \left(\tan \left(\frac{\theta}{2} \right) \right). \tag{4.3}$$

This definition is simpler to determine than rapidity as it leverages the detector's geometry and the particle's trajectory. Pseudorapidity approximates rapidity under the condition that the particle's momentum is significantly greater than its mass, a situation common for particles produced in the LHC. It is particularly useful for characterizing particle distributions. The selection criteria for analysis objects in the ATLAS experiment often include pseudorapidity, alongside other kinematic variables, due to these properties. In this analysis, the pseudorapidity range of interest is ($|\eta| < 1.37$) or ($1.52 < |\eta| < 2.47$).

In addition to these spatial coordinates, several kinematic variables are crucial for

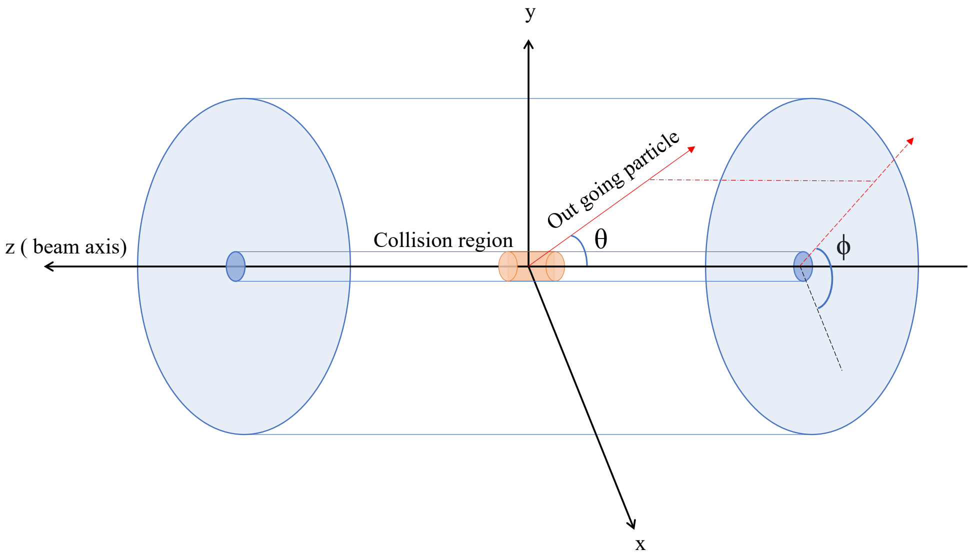

Figure 4.3: The coordinate system in ATLAS.

characterizing particle properties and analyzing the underlying physics processes in the ATLAS experiment. These variables include energy, momentum p, and transverse momentum p_T. Transverse momentum is defined as

$$p_T = \sqrt{p_x^2 + p_y^2} = p \cdot \sin(\theta)\,, \tag{4.4}$$

and represents the component of a particle's momentum perpendicular to the beam axis. Another important kinematic variable is the invariant mass ($M = \sqrt{\hat{s}}$) of all of outgoing particles, which is a Lorentz invariant quantity and can be used to identify resonances by reconstructing decay processes. The ATLAS coordinate system is graphically represented in Fig. 4.3. By employing the cylindrical coordinate system and these kinematic variables, the ATLAS experiment can record the positions and momentum of particles produced in collisions, reconstruct their trajectories through the various layers of the detector, and ultimately provide a wide range of physics data, for searches for BSM particles and interactions.

4.2.2 Tracking

The ATLAS detector provides good lepton identification, high momentum resolution covering a large range of psuedorapidity. The inner detector is immersed in a 2 T magnetic field generated by the central solenoid, bending the path of outgoing charged particles for momentum determination. The tracker in the inner detector includes a pixel detector, a semiconductor tracker and a transition radiation tracker that covers $|\eta| < 2.5$. There are about 1000 particles produced from the collision every 25 ns within this rapidity, creating tremendous track density. Typically, for each track, the pixel detector, semiconductor tracker and the transition radiation tracker contribute 3, 8, 36 tracking measurements respectively. The precision measurements mostly contributed by pixel detector and semiconductor tracker because of their segmentation and intrinsic accuracy. In the barrel region, they are segmented in azimuthal $(R - \phi)$ and axial (z) directions, whereas in the end-cap region, they are in disk shape and segmented in azimuthal $(R - \phi)$ and radial (R) directions. All pixel sensors are identical, the intrinsic accuracies in the barrel are 10 μm $(R - \phi)$ and 115 μm (z); in the end-cap are 10 μm $(R - \phi)$ and 115 μm (R). There are approximately 80.4 million readout channels. Whereas in semiconductor tracker, the intrinsic accuracies in the barrel are 17 μm $(R - \phi)$ and 580 μm (z); in the end-cap are 17 μm $(R - \phi)$ and 580 μm (R). There are approximately 6.3 million readout channels. The transition radiation tracker only covers $|\eta| = 2.0$ and it only provides $(R - \phi)$ information, which has an intrinsic accuracy of 130 μm. There are approximately 351,000 readout channels. Pattern recognition, momentum and vertex measurements, and charge particle identification are mostly achieved by the combination of three trackers. The precision of the tracker directly affects the data quality, specifically the reconstructed e. The invariant mass reconstructed from e^+e^- events rely on the precision of the tracker. To distinguish e from other charged particles, the tracker provides the information of the track curvature, the energy loss per unit length, and the transition radiation.

The information are used to construct a likelihood-based identification algorithm to identify e and other charged particles [43].

4.2.3 Calorimetry

The calorimetry system provides extra pseudorapidity coverage and granularity for the detection of physical objects. The design of the calorimetry system is specialized to cater to specific measurement requirements dictated by benchmark physics phenomena that were of predominant interest at the time of its construction. This includes not only the identification and measurement of particles associated with the Higgs boson but also extends to BSM physics, including KK excitations and extra dimensions [44]. The electromagnetic (EM) calorimeters are capable of capturing EM shower energy induced by outgoing electrons and photons with good containment. This is one of the important components to collect the e and γ data used in this thesis. When an electron or photon enters the calorimeter, it initiates a cascade of particles (an EM shower) that ionizes the liquid argon in the Liquid-Argon (LAr) forward calorimeter. The ionization charge is then collected on electrodes, giving a measure of the particle's energy. As seen in the layout of the inner detector in Fig. 4.4, the EM calorimetry is divided into a barrel part ($|\eta| < 1.475$) and two end-cap components ($1.375 < |\eta| < 3.2$). LAr calorimeters provide EM energy measurement and extend the geometric coverage to $|\eta| = 4.9$. The calorimeters are cylindrically symmetrical in azimuthal angle ϕ.

The hadronic calorimeter is designed to measure the energy of hadrons, which is important for the reconstruction of jets, a highly collimated grouping of particles formed by harmonization of outgoing partons. This measures the energy of hadronic particles like protons, neutrons, pions, and kaons that interact via the strong nuclear force.

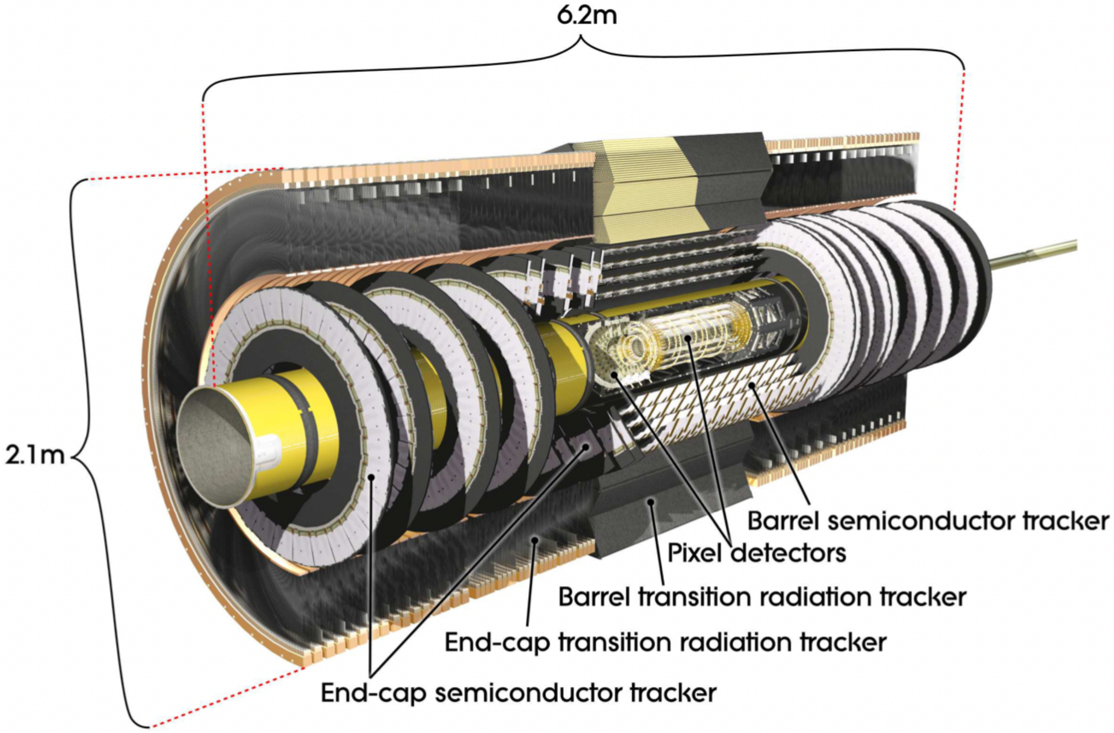

Figure 4.4: The cutview of the inner-detecor. Graphic from [41].

4.3 Triggering

As mentioned in Ch.1, there is a proton bunch crossing at a rate of 40 MHz in the LHC. The high volume of data produced by LHC is logistically impracticable to retain and scrutinize. Many events particularly events with low energy, or events with no interesting physics objects, are not conductive to meaningful physics analysis. Therefore, a trigger system is implemented to select events that are interesting for physics analysis, while discarding most of the others to allow the storage. The trigger hierarchically structured in three levels, Level-1 (L1), Level-2 (L2), and Event Filter (EF) [44]. L1 is a hardware based trigger, triggering decisions are made within 2.5 μs after the bunch-crossing, the maximum acceptance rate is 100 kHz. L1 trigger aims to identify objects with high transverse energy E_{T} of electrons, photons, muons and jets as well as large missing transverse energy $E_{\mathrm{T}}^{\mathrm{miss}}$. After an acceptance decision is made, L1 trigger sends the information as Region-of-Interest (RoI) to L2 trigger for seeding the HLT trigger system. L2 and EF are software based triggers, together they form the High-Level Trigger (HLT). They employed a list of physics signature, event reconstruction and selection algorithms to further filter the events in the RoI. The L2 trigger reduces the event rate to below 3.5 kHz, with an average event processing time of approximately 40 ms. This allows for a more nuanced selection and filtration of events based on various criteria such as energy deposition, momentum, or other particle track parameters. The EF, being the last stage of the triggering system, has more time and computational resources available to it. It can therefore afford to use more complex, precise algorithms for event selection, akin to those used in offline analysis. It reduces the average event rate to 200 Hz, with an average event processing time of approximately 4 s. Around a few GB to a hundred MB data were stored per second for offline analysis [44].

Chapter 5

Object and events selection

Object selection serves as a preliminary step within the analytical framework, focusing on the identification of specific physical objects that pertain to this particular study from a CW/LD perspective. Physical objects may encompass a variety of categories, including particles, jets, and missing transverse energy (MET). The criteria for object selection are meticulously planned to enhance both the integrity of the data and the fidelity of the MC simulations. For example, the selection may be restricted to photons or electrons within specific GeV energy scales to suit the requirements of the CW/LD model. After object selection, event selection is executed to further polish the quality of the data under examination. Although the guidelines for event cleaning are standardized across all ATLAS analyses, they are often not directly tailored to the needs of a specific study. The principal focus of this analysis is on events that yield the production of either two photons or an electron and a positron. The criteria for selection in the e^+e^- channel are adopted from the e^+e^- resonance search [7], whereas the criteria for the $\gamma\gamma$ channel are derived from the high-mass $\gamma\gamma$ resonance search [45]. The specifics of these criteria are tabulated in Table 5.1 for the e^+e^- channel and Table 5.2 for the $\gamma\gamma$ channel.

5.1 Electron and photon reconstruction

To distinguish e^+e^- and $\gamma\gamma$ events, one must identify $e^-e^+/\gamma\gamma$ pairs that forms a primary vertex in the vicinity of the collision point. The commencement of identification for these events relies on the reconstruction and identification of electrons and photons. The kinematic properties of e/γ are measured by the inner detector and the EM calorimeter through EM shower. They have very similar signature in the EM calorimeter, thus the reconstruction process are parallel [46]. It is not common to see multiples e/γ overlap signals in the detector, each signal has to be carefully reconstructed and isolated.

Therefore, the reconstruction process consists of three steps: track reconstruction, cluster reconstruction and track-cluster matching [43]. The e/γ decay from gravitons, and other EM candidates will first pass through the inner-detector and trigger the charged-particle track identification if charged. Information from the inner detector and transition radiation tracker at the outermost area of the inner detector are used by the pattern-recognition algorithm to reconstruct the track. The candidate enters the EM calorimeter, the exit point of the inner-detector is expected to be very close to the entry point of the EM calorimeter. Showering and energy depositing in the EM calorimeter will be recorded to construct an EM-energy cluster candidates using the sliding window algorithm [47]. Finally, the track-cluster matching investigate use the $\Delta\eta \times \Delta\phi$ difference between the inner detector exit and EM calorimeter entry, and the ratio of the cluster energy to the track momentum to identify the candidates.

To distinguish e and γ, further quality criteria, namely 'identification selections' are applied [48]. The identification selections of prompt e/γ relies on a likelihood-based method constructed from quantities measured in the inner detector and calorimeter. The variables used are chosen according to their most distinguishable physical signature. For example, electrons are likely to have non-trivial hit the innermost-pixel layer, and momentum lost by the track between perigee (point on the trajectory of a charged particle that is closest to the center of the detector) to the last measurement point. Contrary, photons have unique energy depositing patterns, which are characterized by the lateral and longitudinal shower shapes. For example, it uses the minimum energy deposition in the cell located in between the first and second maximum energy deposition cell.

For each identified object a vertex matching algorithms are used to match the track with the primary vertex. With additional requirements on the track quality and the vertex quality, a primary vertex is reconstructed, thus a $e^+e^-/\gamma\gamma$ event is identified.

5.2 Events selection

An event candidate has to pass a set of selection criteria to be considered as a reliable analysis event. Following the ATLAS data preparation internal guideline, the subsequent event selections were applied:

Good run list: Data must be obtained from the good run list (GRL). GRL is a list of runs and time-interval of recording that are considered good for physics analysis prepared by the Data Quality team of ATLAS [49]. Multiple criteria must be satisfied for a run to be considered good, including but not excluded to stable beam conditions, capture of the full detector readout, and proper functioning of the trigger and data acquisition systems.

LAr and Tile error: LAr calorimeter and tile calorimeter can sometimes experience a phenomenon known as a noise burst. This is when the detector records a high amount of spurious signals not caused by actual particle collisions. These noise bursts can create problems for data analysis as they can mimic or mask real signals. These issues might include electronic glitches, hardware malfunctions, or other unexpected problems. The corrupted events are removed.

SCT event upsets error: Events affected by the SCT event upsets are removed. An event upset is a change of state caused by ions or electromagnetic radiation striking a sensitive node in a microelectronic device. Event upsets are most commonly associated with bit flips in digital devices.

Incomplete events (CoreFlag Error): Events that are not fully recorded are removed.

Debug stream and duplicated events: Events that cause the high-level trigger to crash and event duplicates are checked, and are removed.

Primary vertex requirement: An event must have at least one primary vertex with at least two associated tracks. The primary vertex is the vertex with the highest sum of the squared transverse momenta of its associated tracks. This requirement is to ensure that the event is from a pp collision but not other sources.

5.3 Electron selection

The main physics object used in the e^+e^- resonant search are electrons [7].

5.3.1 Electron selection criteria

The electron selection criteria are chosen to ensure the quality of the electron candidates for this analysis which are listed in Table 5.1. Studies for this selection and other alternatives are described in the appendix of [17]. The data from calorimeter responses to electrons originating from $Z \rightarrow e^+e^-$ events are used to calibrate the energy scale and resolution model of electrons. The calibration version designated as es2017_R21_v1 is implemented for this purpose. During event reconstruction, it is common for the reconstructed track to exhibit deviations from the beamline. The nearest point between the reconstructed track and the beamline itself is called point of the closest approach. Two parameters are associated with this point:

Electron selection	
Feature	*Criteria*
Pseudorapidity range	$(\|\eta\| < 1.37) \,\|\|\, (1.52 < \|\eta\| < 2.47)$
Energy calibration	es2017_R21_v1 (ESModel)
Transverse momentum	$p_T > 30\,\mathrm{GeV}$
Object quality	Not from a bad calorimeter cluster From regions with EMEC bad HV (2016 data only)
Track to vertex association	$\|d_0(\sigma)\| < 5$, $\|\Delta z_0 \sin\theta\| < 0.5\,\mathrm{mm}$
Identification	LooseAndBLayerLLH (QCD fakes) MediumLLH (main selection)
Isolation	Gradient

Table 5.1: The chosen e^+e^- selection criteria.

- d_0 denotes the transverse impact parameter, defined as the shortest distance in the transverse plane between the primary vertex and the point of the closest approach.

- z_0 denotes the longitudinal distance separating the primary vertex from the point of closest approach.

Identification of electron uses a likelihood-based method, with configuration termed LooseAndBLayerLLH and MediumLLH. To determine whether an electron is prompt, a gradient based isolation method is employed. This isolation criterion is linearly dependent on the electrons's p_{T}.

5.3.2 Dielectron trigger

Events satisfying the selection criteria described above can be selected through triggering. The following trigger requirements are applied:

- 2015: `2e12_lhloose_L12EM10VH`

- 2016: `2e17_lhvloose_nod0`
- 2017–2018: `2e24_lhvloose_nod0`

The description of the trigger name `2eX` is two electrons with energy $\geq$ `X` GeV, `lhloose` indicates the loose quality. The quality of physics objects identification in ATLAS is categorized into three levels: loose, medium, and tight.

- Loose: High efficiency but also higher fake rate. It is commonly used when the cost of losing signal events is higher than the cost of including background events.
- Medium: Balanced efficiency and fake rate.
- Tight: Lowest efficiency but also very low fake rate. Useful when minimizing background events is more important than maximizing signal events.

The string after `L1` specify the L1 trigger requirement. `V` represents varying thresholds with η and `H` is the hadronic core isolation. `nod0` indicates that no transverse impact parameter (d_0) are required.

5.4 Photon selection

The main physics object used in $\gamma\gamma$ resonant search are photons [45].

5.4.1 Photon selection criteria

The photon selection criteria are chosen to ensure the quality of the photon candidates for this analysis which are listed in Table 5.2. Studies for this selection and other alternatives are described in the appendix of [17]. The isolation is more complicate and stated here. Two isolation variables were defined.

- In the EM calorimeter, within the cone $\Delta R = \sqrt{\Delta\eta^2 + \Delta\phi^2} \leq 0.4$ of a photon k, $(\sum_{i \neq k} E_{T_i}) - E_{T_k} < 0.022 E_{T_k} + 2.45$ GeV.

Photon selection	
Feature	*Criteria*
Pseudorapidity range	$(\lvert\eta\rvert < 1.37) \mid\mid (1.52 < \lvert\eta\rvert < 2.37)$
Energy calibration	es2017_R21_v1 (ESModel)
Transverse energy	$p_T > 25\,\mathrm{GeV}$
Track to vertex association	Photon pointing method and Neural network [50]
Identification	*Loose* and *tight*

Table 5.2: The chosen $\gamma\gamma$ selection criteria.

- Within the cone $\Delta R = \sqrt{\Delta\eta^2 + \Delta\phi^2} \leq 0.2$ of a photon k, $\left(\sum_{p_T > 1\mathrm{GeV}} p_T\right) < 0.05 E_{T_k}$

The description of the selection criteria are very similar to the electron case in section 5.3.1.

5.4.2 Diphoton trigger

The following trigger requirements are applied into $\gamma\gamma$ channel:

- 2015–2016: `HLT_g35_loose_g25_loose`
- 2017–2018: `HLT_g35_medium_g25_medium_L12EM20VH`

The description is similar to the e^+e^- trigger case, `HLT` is the High-level trigger and `g` is a photon.

5.5 Data sample

The e^+e^- and $\gamma\gamma$ data samples collected after the event selection are shown in Fig. 5.1. The range of invariant mass is given in Table 5.3.

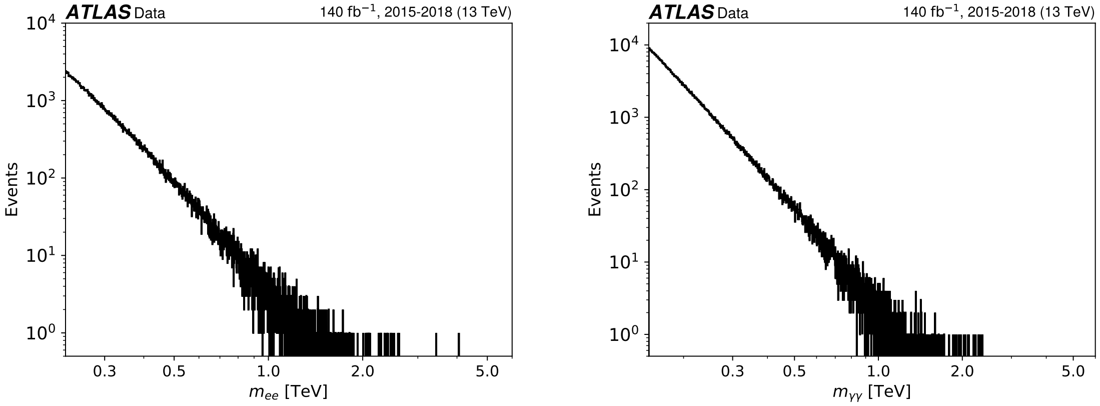

(a) e^+e^- data sample

(b) $\gamma\gamma$ data sample

Figure 5.1: The data samples used in the thesis. They are collected after the event selection, with the integrated luminosity of 140 fb^{-1} and $\sqrt{s} = 13$ TeV.

	e^+e^- channel	$\gamma\gamma$ channel
M_{min}	250 GeV	150 GeV
M_{max}	4182 GeV	2360 GeV

Table 5.3: The range of e^+e^- or $\gamma\gamma$ invariant mass in data samples.

Chapter 6

Modeling

This chapter discusses the Monte Carlo simulations of the CW/LD graviton productions and their decays. We will focus on e^+e^- and $\gamma\gamma$ channels, and discuss the modeling of the corresponding detector responses, and the SM background of these channels.

6.1 Signal modeling

This section discusses the MC simulations of the CW/LD signals with the particle physics processes simulator Pythia [51], and the detector responses for e^+e^- and $\gamma\gamma$ processes. Pythia is a general-purpose high energy physics event generator which performs $2 \to 2$ scattering processes and matrix element calculations. The signal waveforms are determined by the parton distribution functions (PDF) of incoming partons, the differential cross-section of the CW/LD, and the detector responses to the corresponding particles. The kinematics of the clockwork graviton which are used to simulate the graviton samples unaffected by the detector were discussed in Ch.3, we will only discuss the detector responses to our samples.

6.1.1 Monte Carlo simulations of CW/LD

The CW/LD model can be simplified into a function of two independent variables (k, M_5) [17]. We calculated the graviton narrow-width approximated cross-sections, and the number of events across the mass modes such that they added up to 100,000 events with standalone code. The graviton mass calculated has a Breit-Wigner width. We utilize Pythia to simulate graviton production, incorporating the Breit-Wigner resonance profile to characterize the graviton mass distribution. Separate simulations are performed for graviton decays into e^+e^- and $\gamma\gamma$. We evaluate the expectation values of signal s_i for the i-th bin in the graviton invariant mass spectrum. The spectrum will later be used to model the corresponding signals in e^+e^- and $\gamma\gamma$ channels. The ultimate goal for this search is to find new physics and determine the values of (k, M_5) using the data in ATLAS, naturally we need to search across the 2D space of (k, M_5). A grid of samples of different pairs of (k, M_5) are generated as our signal. According to the cross-section Eq. 3.5, the production energy combines with the PDF has dominant effect on the waveforms of number of gravitons at different modes. Computationally, the `NNPDF23_lo_as_130_qed` PDF set is used as the PDF set [52], `Cteq6l1` is separately used to verify the result from `NNPDF_lo_as_130_qed`. `NNPDF23_lo_as_130_qed` utilized the power of neural network for providing a flexible and data-driven approach to PDF determination. The methodology not only allows for robust uncertainty quantification, the independence of physics model also ensures minimal theoretical bias, thereby enhancing the accuracy and reliability of our CW/LD simulation.

6.1.2 Graviton generation

To search through the model parameter space of (k, M_5), we are required to generate a grid of graviton signal samples at various (k, M_5). This is done mainly in Pythia [51], version 8.244. It also handles the modeling of the parton shower, hadronization of SM daughters from the graviton decay. Hadronization and parton showering are particularly important in the context of high energy collision. Parton shower is a process that the initial partons collide together and radiate newly created partons, those partons undergo a series of successive branching or splitting, result in emission of many secondary partons. Hadronization is the process which the ‘isolated’ colored quarks and gluons confine into colorless baryons or mesons, due to the property of confinement. The transition is non-perturbative and not fully understood. It is described phenomenologically in the context of QCD inspired models. As the partons produced in the shower lose energy and separate from one another, they undergo hadronization to form hadrons. Pythia employs a simple shower algorithm [53] which is derived from Dokshitzer-Gribov-Lipatov-Altarelli-Parisi (DGLAP) evolution equations [54]; and for the hadronization algorithms, Lund-String model [55, 56] are employed. Even in the context of a generator, many physics processes are lacking complete understanding and must be implemented through a set of parameters. Those optimized parameters are called a tune, Pythia default tunes are used unless they are specified.

The LD/CW model is not programmed in Pythia, it is equivalent to a series of Randall-Sundrum (RS) gravitons (discussed in Ch.2) given that masses, coupling strengths, resonance widths and cross-sections are recalculated with the given (k, M_5) according to the CW/LD model. The RS model were already implemented in Pythia and documented in [57]. To set up the LD/CW model in Pythia, in each sample (k, M_5), and in each graviton mass mode n, the mass m_n, coupling strength Λ_n, cross-section σ_n, decay width Γ_n and the branching ratio are calculated with standalone code. The Pythia RS graviton model was modified with aforementioned parameters, with the coupling strength represented in terms of a parameter κ_n [57], which can be obtained using [17]

$$\kappa_n^2 = \frac{2}{\Lambda_n^2}. \tag{6.1}$$

The relative contributions of each production process can be deduced from Eq. 3.5, both are functions of m_n. They are shown in Fig. 6.1. For gg, the relative contribution is $\frac{3\mathcal{L}_{gg}}{3\mathcal{L}_{gg}+4\sum_q \mathcal{L}_{q\bar{q}}}$, the fraction increases from 4.2% with increasing mass. For $q\bar{q}$, the relative contribution is $\frac{4\sum_q \mathcal{L}_{q\bar{q}}}{3\mathcal{L}_{gg}+4\sum_q \mathcal{L}_{q\bar{q}}}$, the fraction decreases from 95.8% with increasing mass. Their contribution are equal at a graviton mass of 3.2 TeV, and the

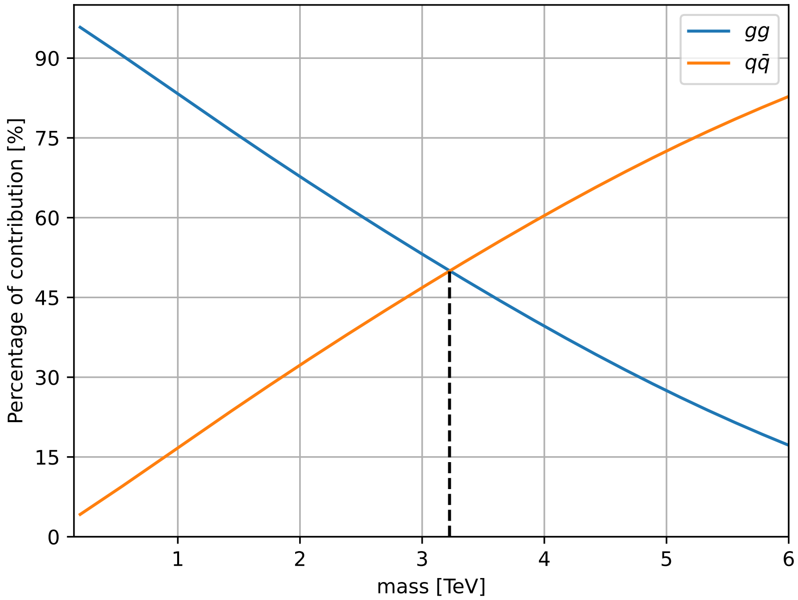

Figure 6.1: The relative contributions of gg and $q\bar{q}$ production processes as a function of graviton mass $m_n \in [150, 6000]$ GeV

$q\bar{q}$ contribution dominates at higher mass.

For each set of parameters (k, M_5), we generate in total 100,000 gravitons, the number of graviton for each mass mode is generated through $100{,}000 * \frac{\sigma_n(k,M_5)}{\sigma_{tot}(k,M_5)}$. This number does not reflect the actual expected number of gravitons that can be expected in LHC, however, it serves the purpose of investigating the signal strength and the signal shape, and uncertainty estimation.

The cascade decay effect is included in the simulation. As discussed in Ch.2, the process can be included by iterating from the highest mass mode to the lowest mass mode. The procedure is described graphically in Fig. 6.2 and also as follows:

1. Apply the procedure below from the highest mass modes to the lowest mass mode
2. For each graviton mass mode m, count the number of gravitons n_m
3. Apply the MC hit-and-miss method to all n_m gravitons to determine whether it decays to SM particles or two gravitons, but daughters' modes are not determined yet. It decays into SM particles or two gravitons depends on the branching ratio.
4. If two gravitons are produced, decrease n_m by 1, apply the hit-and-miss method again to the two gravitons to determine their decay modes k, l. Increase n_k by 1 and n_l by 1.
5. Iterate from step 2 until all mass modes are considered, the updated number of gravitons in each mass mode are the final result.

The results of 10000 MC simulations of the cascade decay for each (k, M_5) is shown in Fig. 3.8 and in Appendix D, but reproduced here for convenience. Multiple blue dots are presented at the same mode because all 10,000 MC simulations are plotted together, one single blue dot could contain multiple MC results and the blue dots at the same mode form a distribution. Unlike the analytical solutions, the MC results have integer increment or decrement, therefore ladder-like discrete dots in the same mode are shown in the graph. The black curve is the median of the MC results. The MC result is consistent with our analytical result.

For the scattering process, Pythia 8.244 is used. Modeling of gravitons decay, parton shower and hadronization are also performed in Pythia, with center of mass energy equivalent to the LHC RUN-2 colliding energy 13 TeV. The gravitons are

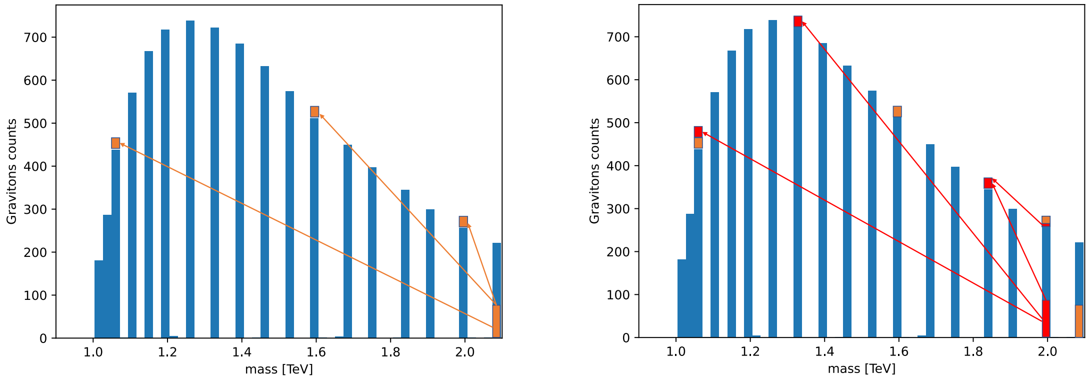

(a) (b)

Figure 6.2: A schematic demonstration (out of scale) of the cascade decays simulation process. In (a), fraction of gravitons at the highest mass mode, covered in orange color, decays to number of gravitons of smaller modes at the top of bars. Following the same procedure in second-highest mode in (b). The gravitons count is the sum of the original count covered in blue and the count that decayed from the higher mass mode covered in orange. Fraction of it decays into even smaller modes covered in red. The procedure is repeated until all modes are considered. The final count of gravitons in each mode is the remaining blue fraction in the figure.

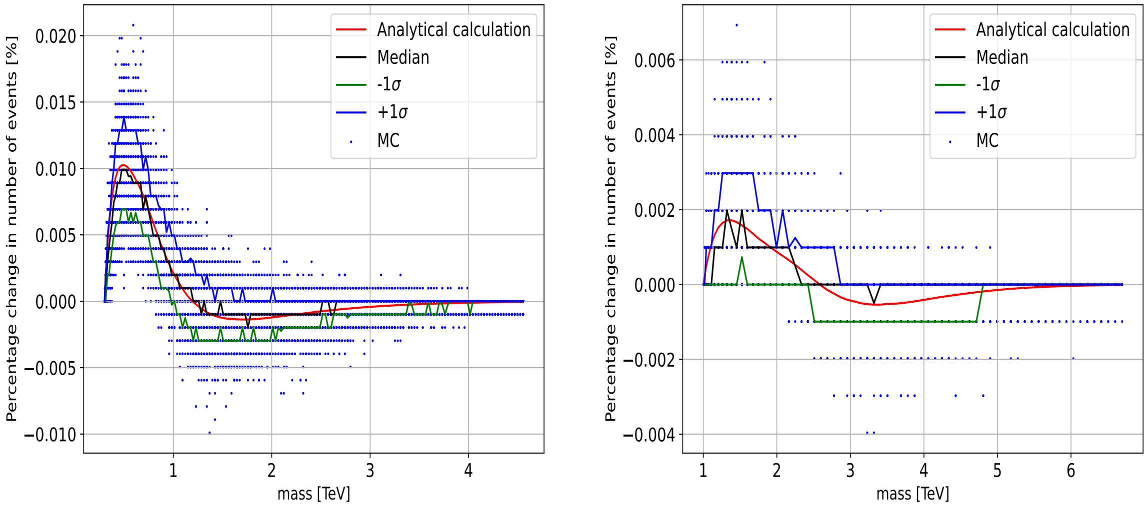

(a) $k = 0.3$ TeV $M_5 = 3.0$ TeV (b) $k = 1.0$ TeV $M_5 = 6.0$ TeV

Figure 6.3: Reproduced from Fig. 3.8. The cascade decay effect contributed to the number of event of gravitons. The analytical result and the MC simulations are presented.

stored in the LHE file format separately for each mass mode, a standard file format to store process and event information, primarily output from parton-level event generators for further use by general-purpose ones [58].

It is impractical to generate samples that continuous in the parameter space in (k, M_5). The grid point is chosen in a way to demonstrate the changes when varying k and M_5 independently, to provide ample information to cover the range for getting the exclusion limit. According to the cross-section Eq. 3.5 and coupling strength Eq. 3.4,

$$\sigma \propto \frac{1}{\Lambda_G^{(n)2}} \propto \frac{1}{M_5^3 R (1 - \frac{k^2}{m_n^2})^{-1}} \tag{6.2}$$

$$\propto \frac{1}{M_5^3 (\frac{1}{k} \ln(\frac{\sqrt{k}}{M_5^{3/2}}))} \propto \frac{1}{M_5^3 \ln M_5} \times \frac{k}{\ln(k)}, \tag{6.3}$$

where we applied $k \ll m_n$. We are more interested in varying the values of k as the cross-section is more sensitive to k than M_5. The dependence of $\sigma \propto 1/M_5^3$ leading to varying M_5 does not provide extra useful information other than suppressing the cross-section. Varying k would globally and locally change the shape of the cross-section profile particularly when k is comparable to the mass of the graviton $(\sigma \propto k\ (1 - \frac{k^2}{m_n^2})\ /\ \ln(k))$. In our study, we have chosen the following discrete values for the grid points. For e^+e^- channel,

- $k = [0.3, 0.5, 1, 1.5, 2.5, 3.0]$ TeV
- $M_5 = [1, 2, 3, 4, 5, 6]$ TeV

For $\gamma\gamma$ channel

- $k = [0.3, 0.5, 1, 1.5]$ TeV
- $M_5 = [1, 2, 3, 4, 5, 6]$ TeV

We consider all possible combinations of these values, resulting in a total of (24) 36 distinct grid points for $(\gamma\gamma)$ e^+e^- channel.

6.2 Transfer method

After generating the so-called truth samples with Pythia, where the graviton is created and before partons undergo hadronization, we obtained the perfect e^-e^+ and $\gamma\gamma$ invariant mass spectrums which are independent of the detector. However, it is mandatory to include the detector effect into our samples as the physical structure and the resolutions of the detector change the MC signal shape discussed above. We ought to find out how the detector responses to our MC graviton samples after the decay, hadronization and parton showering, particularly in our channels of interested. It is computationally expensive to do a full simulation to obtain satisfactory MC uncertainty so a semi-analytical approach is used. For both channels, we applied the transfer method (also known as the convolution method or the transform method) to obtain the MC samples after including the detector effects [59]. Here we provide the mathematical explanation with the experimental considerations.

We denote the distribution that our truth samples were drawn from the truth distribution as $f(\boldsymbol{x})$. The distribution depends on the values of (k, M_5), e^+e^- and $\gamma\gamma$ channels response differently towards the truth samples. And the $\boldsymbol{x}$ is the vector of graviton masses in our case. The observed distribution (also known as the smeared/-convoluted distribution) by its name, the distribution we observed in our detector, must be related to the truth distribution and the decay channel dependent detector effects, denote as $f'(\boldsymbol{x'})$. And the $\boldsymbol{x'}$ is again the mass of gravitons, however different from $\boldsymbol{x}$. They are the invariance mass axis in the observed spectrum, and in the truth spectrum respectively. Combining the ideas we obtain the mathematical description relating them.

$$f'(\boldsymbol{x'}) = \int_{-\infty}^{\infty} t(\boldsymbol{x}, \boldsymbol{x'}) f(\boldsymbol{x}) d\boldsymbol{x}. \tag{6.4}$$

The resolution function (or the kernel) $t(\boldsymbol{x}, \boldsymbol{x'})$, is the probability density that for a count locate at $\boldsymbol{x}$ there are $t(\boldsymbol{x}, \boldsymbol{x'})d\boldsymbol{x}$ chances to find the same count in interval $[\boldsymbol{x'}, \boldsymbol{x'} + \boldsymbol{dx'}]$. Practically, the function is bounded by physical constrains, we do not expect the truth values and the observed values to deviate from each other tremendously, we expect the functional form has $|\boldsymbol{x} - \boldsymbol{x'}|$ dependence and contributes the most when $|\boldsymbol{x} - \boldsymbol{x'}|$ is small; approach 0 when $|\boldsymbol{x} - \boldsymbol{x'}|$ is large.

However, Eq. 6.4 does not include a phenomenon that not all produced gravitons can be detected. We have to amend Eq. 6.4 by including acceptance and efficiency caused by the detector and analysis selections. Two experiment effects are isolated from detector effects in discussions because they were influencing different parts in the analysis. In general, detector effects are about uncertain measurements of the quantitative event, acceptance and efficiency are about the fraction of measurable events and the fraction of measurements passing the selection criteria over the total number of events. Not all particles created in a collider can be detected, which happens to be the case where particles enter an area of the detector that is not instrumented.

$$f'(\boldsymbol{x'}) = \int_{-\infty}^{\infty} t(\boldsymbol{x}, \boldsymbol{x'}) f(\boldsymbol{x}) A(\boldsymbol{x}) \epsilon(\boldsymbol{x}) d\boldsymbol{x}, \tag{6.5}$$

where A is the acceptance, and ϵ is the efficiency. We unavoidably discretize the above theory into bins since we are working with histograms.

$$A(x_i) = \left.\frac{\text{events passing acceptance criteria}}{\text{events in MC samples}}\right|_{\text{within bin } x_i}, \tag{6.6}$$

$$\epsilon(x_i) = \left.\frac{\text{events passing selection criteria}}{\text{events passing acceptance criteria}}\right|_{\text{within bin } x_i}. \tag{6.7}$$

That is, their product $A(\boldsymbol{x}) \times \epsilon(\boldsymbol{x})$ describe the probability that an event passes the detector physical constrain and the selections at invariant mass $\boldsymbol{x}$. The contexts below discuss the resolution function construction and the best fitted analytical model for both channels. The transferred functions are validated with the ATLAS reconstructed MC samples prepared in [17].

6.2.1 Transfer method for e^-e^+

The full details of the transfer method for e^-e^+ are described in [60]. The resolution function is obtained through convoluting a functional form towards their e^+e^- MC samples, until the convoluted samples agree with the data. The physics processes of producing e^-e^+ are well studied in theories and experiments, numerous functional forms of resolution function have been studied and proposed thoroughly, taking into account the available knowledge and experimental considerations. Eq. 6.8 shows the best fit functional form for the resolution function.

$$t(\mathcal{R}) = \kappa \times \mathrm{CB}(\mathcal{R}|\mu_{CB}, \sigma_{CB}, \alpha_{CB}, n_{CB}) + (1-\kappa) \times \mathrm{Gauss}(\mathcal{R}|\mu_G, \sigma_G), \tag{6.8}$$

$$\mathcal{R} = \frac{M_r - M_t}{M_t}. \tag{6.9}$$

CB is the Crystal-Ball function, it consists a Gaussian core and a power-law low-end tail, having an asymmetric shape where one side of the distribution is longer, and describes the tails of the detector response. The mathematical form is given by:

$$CB(x;\mu,\sigma,\alpha,n) = N \cdot \begin{cases} \exp\left(-\frac{(x-\mu)^2}{2\sigma^2}\right), & \text{if } \frac{x-\mu}{\sigma} > -\alpha \\ A\left(B - \frac{x-\mu}{\sigma}\right)^{-n}, & \frac{x-\mu}{\sigma} \le -\alpha \end{cases} \tag{6.10}$$

where the factors A, B are determined by the continuity of the function at α. N is the normalization factor. They are given by:

$$A = \left(\frac{n}{|\alpha|}\right)^n \exp\left(-\frac{|\alpha|^2}{2}\right) \tag{6.11}$$

$$B = \frac{n}{|\alpha|} - |\alpha| \tag{6.12}$$

$$N = \frac{1}{\sigma}\left[\frac{n}{|\alpha|} \cdot \frac{1}{n-1} \cdot \exp\left(-\frac{|\alpha|^2}{2}\right) + \sqrt{\frac{\pi}{2}}\left(1 + \mathrm{erf}\left(\frac{|\alpha|}{\sqrt{2}}\right)\right)\right]^{-1}. \tag{6.13}$$

The erf is the Gauss error function defined as $\mathrm{erf}(x) = \frac{2}{\sqrt{\pi}}\int_0^x e^{-t^2}dt$. The Gauss is the normal distribution, it describes the main peak of the response distribution. The M_t and the M_r are the truth e^+e^- invariant mass value and the reconstructed mass value respectively. The fitting parameters manifest the following properties:

- μ_{CB} and μ_G are the mean value of the Gaussian core of the CB and the Gaussian, as we parametrized the resolution function with dimensionless variable $\mathcal{R}$ in Eq. 6.9, $\mu_{CB} \approx 0$ for any bin was expected to have good agreement between theoretical values and measurement.

- σ_{CB} and σ_G are the width of the Gaussian core of the CB and Gaussian corresponding to the relative uncertainty of the responses. For e^-e^+ the uncertainty decreases with the energy of the outgoing dielectrons [48].
- α_{CB} is the transition threshold between the Gaussian core and the power-law tail for the Crystal-Ball function. Above the threshold the Gaussian is replaced by a power-law. The function is continuous at α_{CB} for the zeroth and the first derivative. No strong M_t dependence is expected.
- n_{CB} is the exponent in the power-law component in the Crystall-Ball function. No strong M_t dependence is expected.
- κ is the fraction of the Crystall-Ball function in the resolution function. The M_t dependence of this parameter should reflect the relative importance of the tail.

The truth invariant mass dependence of the functional form for the fitting parameters are listed in Table 6.1, and are shown in Fig. 6.4. The behavior of κ reflects the relative importance of the CB function in the resolution function, also reflects the importance of the tail. The tail is mainly given by QED radiation in the e^+e^- case.

The functional description of $A\epsilon_{ee}(M_t)$ is given below and graphically shown in Fig. 6.5.

$$\begin{aligned} A\epsilon_{ee}(M_t) &= 0.871626 - 183.574/M_t + 63470.4/M_t^2 - 1.24022 \cdot 10^7/M_t^3 \\ &+ 4.89 \times 10^8/M_t^4 + 7.09022 \cdot 10^{10}/M_t^5 - 2.71992 \cdot 10^{-5} M_t \\ &+ 1.40882 \cdot 10^{-9} M_t^2. \end{aligned} \tag{6.14}$$

The functional description was determined through full-simulation MC which were done in [60]. The uncertainty of the functional form is evaluated through bootstrapping technique. In this method, bootstrapped samples are generated by randomly

Parameter M_t dependence	Fit results
$\mu_{CB}(M_t) = p_1 + p_2/ln(M_t) + p_3 \cdot ln(M_t) + p_4 \cdot ln(M_t)^4$	$p_1 = 0.13287$
	$p_2 = -0.410663$
	$p_3 = -0.0126743$
	$p_4 = 2.9547 \cdot 10^{-6}$
$\sigma_{CB}(M_t) = \sqrt{p_1^2 + (p_2/\sqrt{M_t})^2 + (p_3/M_t)^2}$	$p_1 = 0.0136624$
	$p_2 = 0.230678$
	$p_3 = -0.00298312$
$\alpha_{CB}(M_t) = p_1$	$p_1 = 1.59112$
$n_{CB}(M_t) = p_1 + p_2 \cdot e^{-p_3 \cdot M_t}$	$p_1 = 1.13055$
	$p_2 = 0.76705$
	$p_3 = 0.00298312$
$\mu_{CB}(M_t) = p_1 + p_2/M_t + p_3 \cdot M_t + p_4 \cdot ln(M_t)^3 + p_5/M_t^2 + p_6 \cdot M_t^2$	$p_1 = -0.00402708$
	$p_2 = 0.814172$
	$p_3 = -3.94281 \cdot 10^{-7}$
	$p_4 = 7.97076 \cdot 10^{-6}$
	$p_5 = -87.6397$
	$p_6 = -1.64806 \cdot 10^{-11}$
$\sigma_G(M_t) = \sqrt{p_1^2 + (p_2/\sqrt{M_t})^2 + (p_3/M_t)^2}$	$p_1 = 0.00553858$
	$p_2 = 0.140909$
	$p_3 = 0.644418$
$\kappa(M_t) = p_1 + p_2 \cdot e^{-p_3 \cdot M_t} + p_4 \cdot M_t + p_5 \cdot M_t^3$	$p_1 = 0.347003$
	$p_2 = 0.135768$
	$p_3 = -0.00372497$
	$p_4 = -2.2822 \cdot 10^{-5}$
	$p_5 = 5.06351 \cdot 10^{-13}$

Table 6.1: Descriptions of the M_t dependence for the fitting parameters in Eq. 6.8 in the e^+e^- channel.

selecting observations from the original data set, each sample having the same number of events as the original. The standard deviation of the distribution of these bootstrapped samples serves as an estimate of the uncertainty.

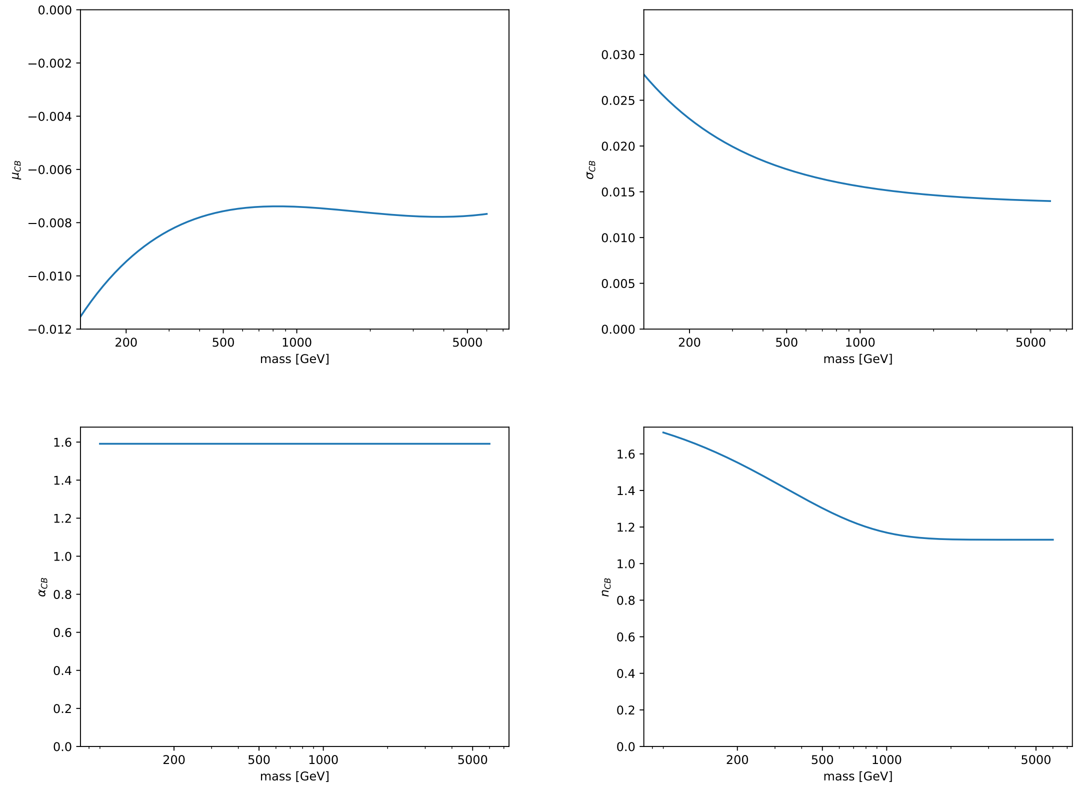

Figure 6.4: The truth invariant mass dependence of the fitting parameters for the e^+e^- transfer function. (Continued on a subsequent page).

Applying the transfer function to the truth samples, we obtain the MC samples that include the detector effects, which is shown in Fig. 6.6.

The validation of the transfer function is shown in Fig. 6.7. Different k values were chosen, M_5 is fixed at 6 TeV. The χ^2 test is performed to determine the fidelity of the transfer function. A rule of thumb is that the χ^2 value should be less than the number of bins in the histogram. Therefore, χ^2/degree of freedom less than 1 is considered good matching between two histograms. The χ^2/degree of freedom values are around 10^{-2}, indicating good agreement between the transferred samples and the ATLAS reconstructed MC samples.

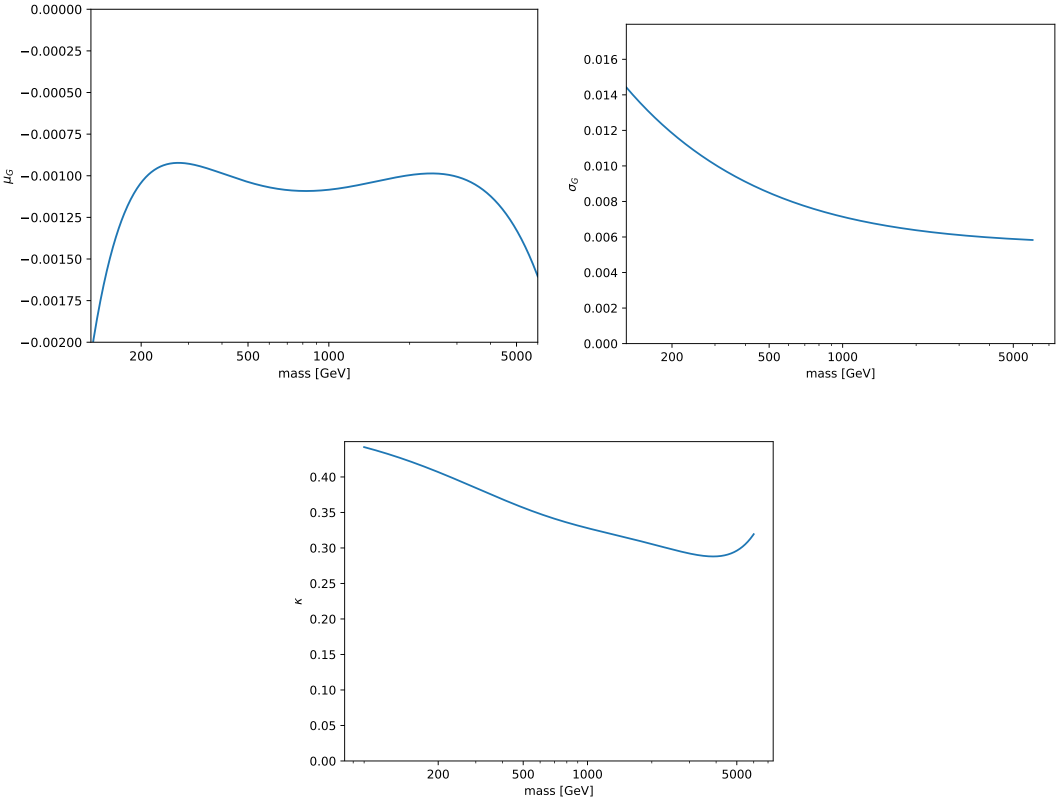

Figure 6.4: Continued.

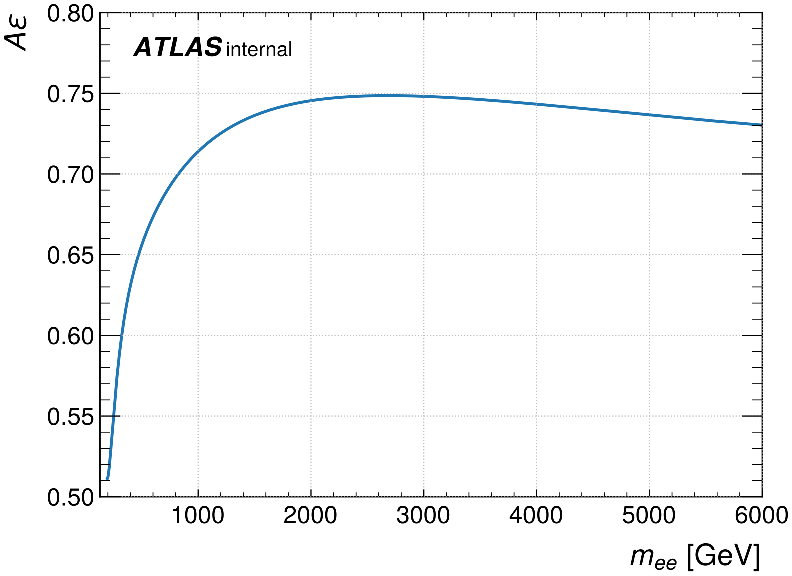

Figure 6.5: The efficiency×acceptance M_t dependence between 90 GeV to 6 TeV. The highest probability of obtaining a detectable event that past the selections is around 2 TeV.

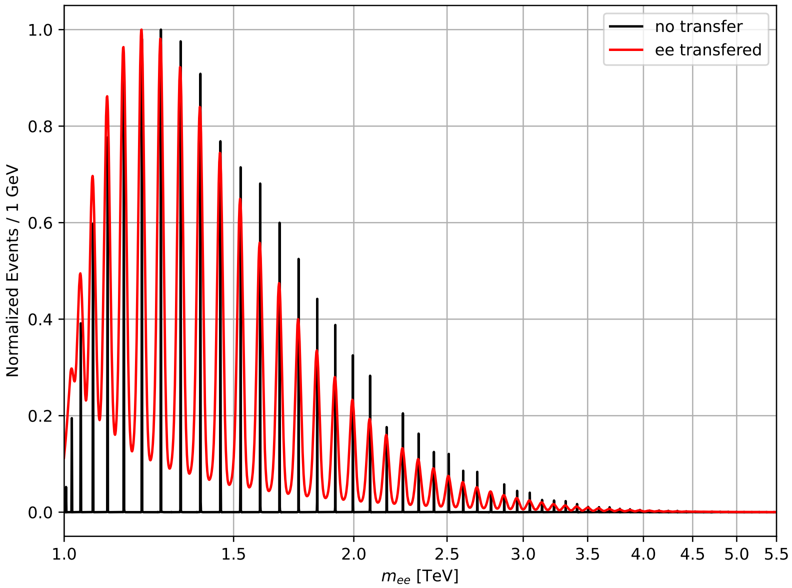

Figure 6.6: Comparison of truth sample with the transferred sample in e^+e^- invariant mass spectrum, where $k = 1$ TeV, $M_5 = 6$ TeV.

6.2.2 Transfer method for $\gamma\gamma$

The full details of the transfer method for $\gamma\gamma$ channel can be found in [61]. The signal modeling strategy is common for the scalar and graviton analyses for $\gamma\gamma$ channel. The narrow-width signal can be regarded as a delta function, and can be modeled with double-sided Crystal Ball function (DSCB). The interpretation of this section is similar with the e^+e^- case. The function describes the narrow-width signal across wide range of the mass spectrum, and is defined as:

$$F_{NW}(t;\alpha_l,n_l,\alpha_h,n_h) = N\cdot\begin{cases}\left(\frac{n_l}{\alpha_l}\right)^{n_l}\cdot\left(\frac{n_l}{\alpha_l}-\alpha_l-t\right)^{-n_l}\cdot e^{-\alpha_l^2/2}, & \text{for } t>\alpha_l\\ e^{-t^2/2}, & \text{for } -\alpha_l\le t\le\alpha_h\\ \left(\frac{n_h}{\alpha_h}\right)^{n_h}\cdot\left(\frac{n_h}{\alpha_h}-\alpha_h+t\right)^{-n_h}\cdot e^{-\alpha_h^2/2}, & \text{for } t<-\alpha_h\end{cases} \tag{6.15}$$

where $t = (m_{\gamma\gamma} - \mu)/\sigma$ and μ and σ are the mean and standard deviation of the Gaussian core, respectively. The parameters α_l and α_h are the locations of the low and high transitions between the Gaussian core and the power-law tails, respectively. The parameters n_l and n_h are the power parameters of the low and high tails, respectively. The normalization factor N is chosen such that the integral of the function is equal

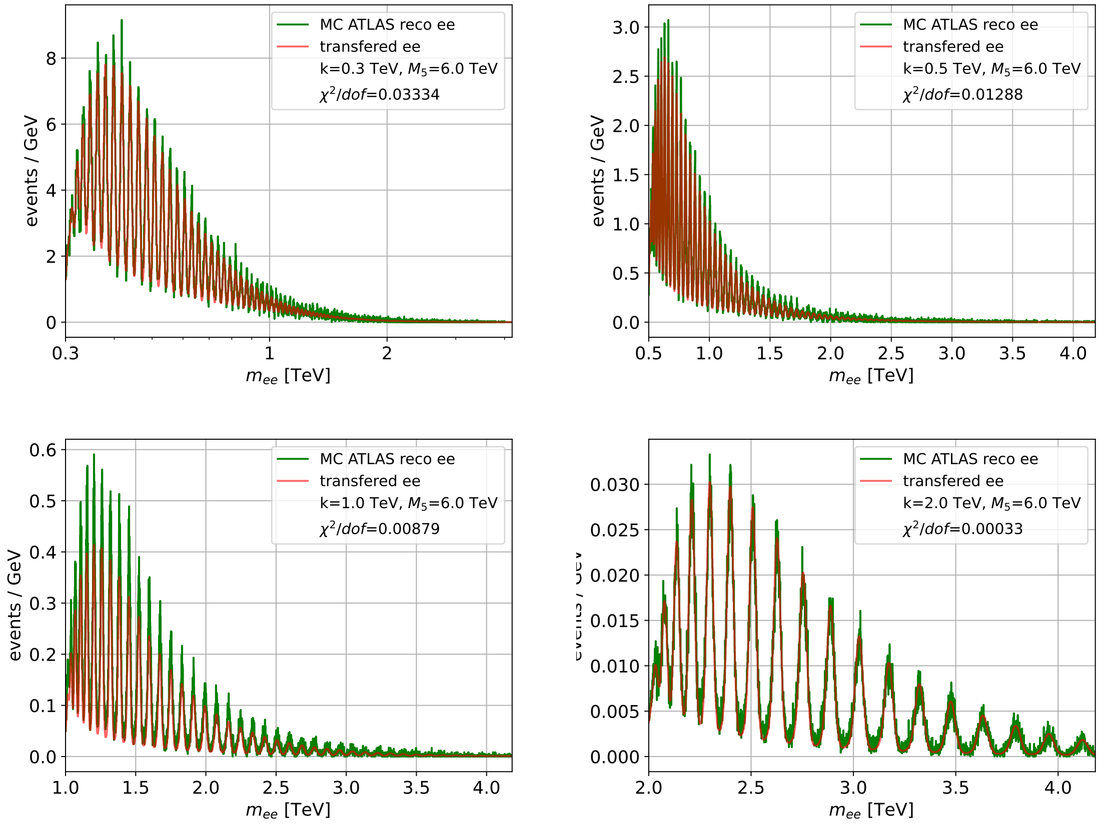

Figure 6.7: The validation of the transfer function in e^+e^- channel. χ^2 test is performed between the transferred samples and the ATLAS reconstructed MC samples.

to unity, and is given by:

$$
\begin{aligned}
N^{-1} = \sigma \Bigg\{ & \sqrt{\frac{\pi}{2}} \left[\operatorname{erf}\left(\frac{\alpha_l}{\sqrt{2}}\right) + \operatorname{erf}\left(\frac{\alpha_h}{\sqrt{2}}\right) \right] \\
& + \frac{1}{n_l - 1} \left(\frac{n_l}{\alpha_l}\right)^{n_l} e^{-\frac{\alpha_l^2}{2}} + \frac{1}{n_h - 1} \left(\frac{n_h}{\alpha_h}\right)^{n_h} e^{-\frac{\alpha_h^2}{2}} \Bigg\}.
\end{aligned}
\tag{6.16}
$$

The values of the parameters are determined differently from the e^+e^- case. The parameters were preliminarily determined from the fit to the MC simulation at each mass point. Then the parameters were fitted with a linear function of the mass, and updated repeatedly to obtain a better description of the mass dependence. The fitting result was applied broadly across all (k, M_5). One would argue that such fitting approach for the DSCB function is not a good approximation for the signal with different (k, M_5). The mean and standard derivation which were supposed to capture gravitons' properties are now mass dependent for generalization across (k, M_5), it is plausible to have the fitting parameter depends on (k, M_5) instead. Here we argue that this approach is valid for the following reason and conditions. First, the M_t dependence comes from the (k, M_5) dependence of the mean and standard derivation of the Gaussian core. They are implicitly related, and the degree of dependence is tested by the fitting result. Second, the generalization is possible because the main difference between different (k, M_5) gravitons are the mass to width ratio. As long as the narrow-width approximation is applicable, the resonance is essentially a delta function, the mass of a resonance is well-defined at one point, and the fitting result is applicable to other grid points. The narrow-width approximation is indeed true in our scope of search. This can be seen from section 3.2, and from the following algebraic manipulation. Using Eq. 3.7 and Eq. 3.4

$$\frac{\Gamma_{\gamma\gamma}}{m_n} = \frac{1}{M_5^3}\frac{m_n^2}{80\pi M_5^3 R}\left(1 - \frac{k^2}{m_n^2}\right) = \frac{1}{80\pi M_5^3}\left(\frac{m_n^2 - k^2}{R}\right) = \frac{1}{80\pi M_5^3}\left(\frac{k(m_n^2 - k^2)}{kR}\right). \tag{6.17}$$

Expressing all variable in the unit of GeV, the factor $80\pi M_5^3$ is of $\mathcal{O}(10^{11})$, the k dependent factor is $\mathcal{O}(10^5)$ to $\mathcal{O}(10^9)$ in this search. Narrow-width condition is ensured given that we work in mass mode smaller than $\mathcal{O}(10^3)$. Table 6.2 shows the final values of the parameters and their mass dependence [17], and are shown in Fig. 6.8.

DSCB parameters	M_t dependence
$\Delta M_t = \mu - M_t$	$0.327 - 0.834 \cdot 10^{-3} M_t$
σ	$1.211 + 6.330 \cdot 10^{-3} M_t$
α_l	$1.395 - 6.827 \cdot 10^{-5} M_t$
α_h	$1.693 + 0.912 \cdot 10^{-5} M_t$
n_l	19.7 (constant)
n_h	12.1 (constant)

Table 6.2: Description of the M_t dependence for the fitting parameters in Eq. 6.15 in the $\gamma\gamma$ channel.

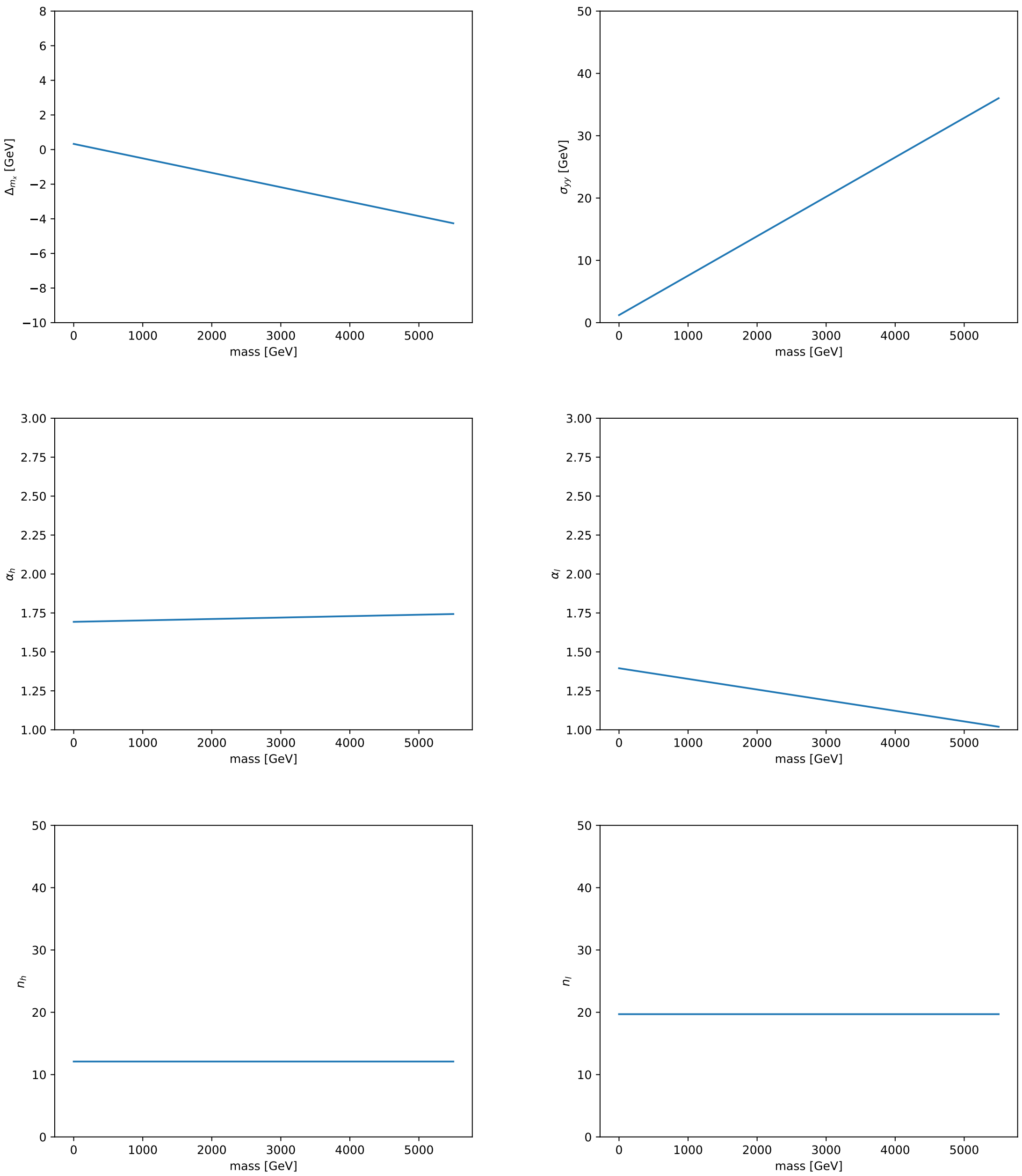

Figure 6.8: The truth invariant mass dependence of all fitting parameters for the $\gamma\gamma$ transfer function.

The functional description of $A\epsilon_{\gamma\gamma}(M_t)$ is given below [17] and graphically shown in Fig. 6.9.

$$A\epsilon_{\gamma\gamma}(M_t) = -6.514 - 0.329e^{-1.84\cdot 10^{-3}\cdot M_t} + 6.996e^{1.2\cdot 10^{-7}\cdot M_t}. \tag{6.18}$$

Applying the transfer function to the truth samples, we obtain the MC samples that

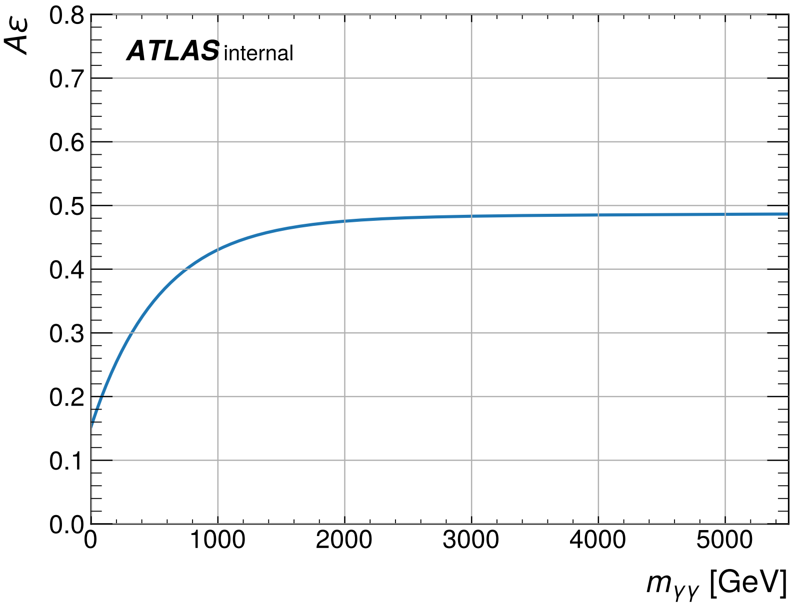

Figure 6.9: The efficiency×acceptance M_t dependence between 0 TeV to 5.5 TeV. The probability of obtaining a detectable event that past the selections is increasing throughout.

include the detector effects, which is shown in Fig. 6.10.

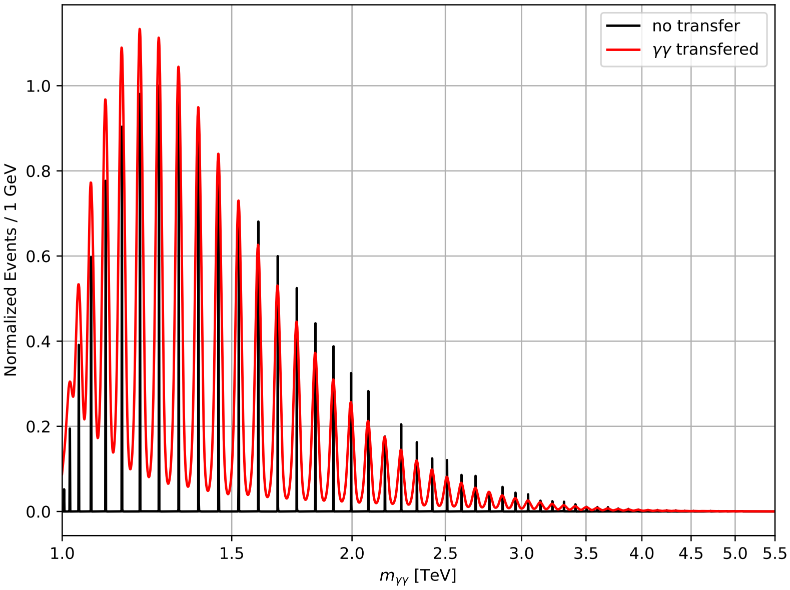

Figure 6.10: Comparison of truth sample with the transferred sample in $\gamma\gamma$ invariant mass spectrum, where $k = 1$ TeV, $M_5 = 6$ TeV.

The validation of the transfer function is shown in Fig. 6.11. Different k values were chosen, M_5 is fixed at 6 TeV. The χ^2 test is performed to determine the fidelity of the transfer function. The χ^2/degree of freedom values are around 10^{-1}, indicating good agreement between the transferred samples and the ATLAS reconstructed MC samples.

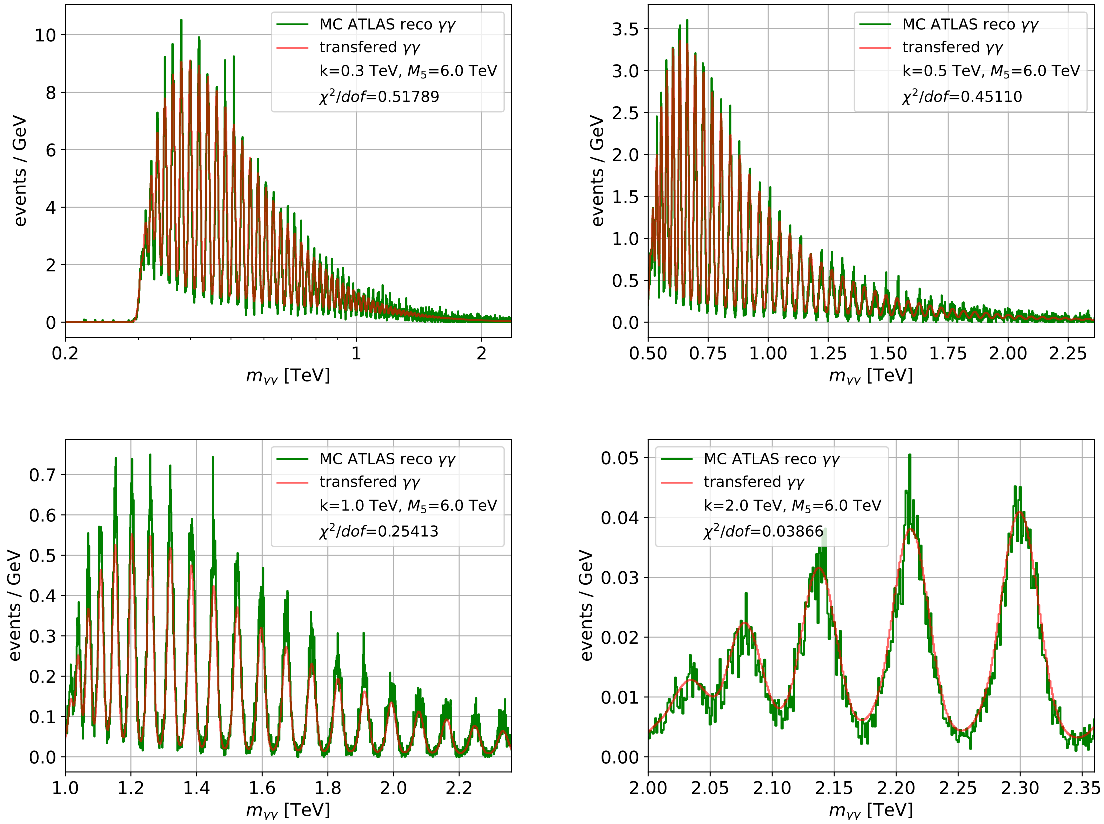

Figure 6.11: The validation of the transfer function in $\gamma\gamma$ channel. χ^2 test is performed between the transferred samples and the ATLAS reconstructed MC samples.

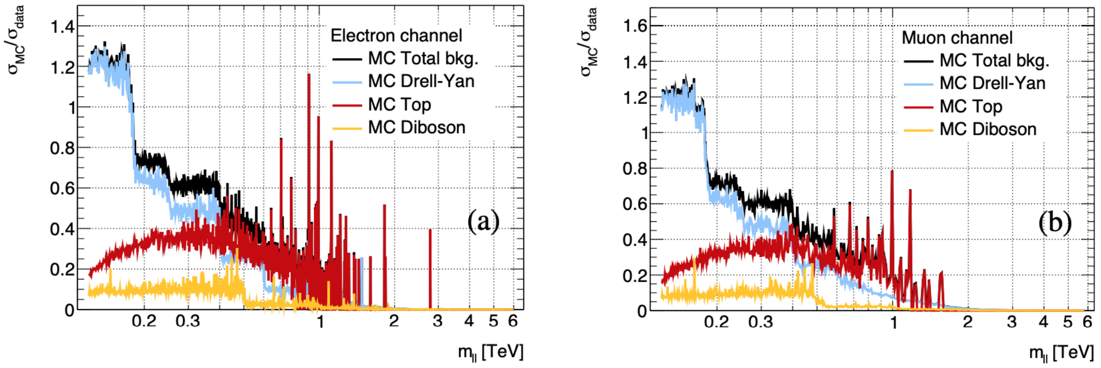

(a) e^+e^-

(b) $\mu^+\mu^-$

Figure 6.12: The binned ratio of statistical errors between MC and data vs dilepton mass in [62].

6.3 Background modeling

To model the background, a data-driven method is applied to both the e^+e^- and $\gamma\gamma$ channels as suggested in [7] and in [45]. The background estimation is obtained by fitting a functional form to the data distribution. The limited MC statistics for RUN-1 dataset caused a level of compromised sensitivity for narrow resonance searches. As shown in Fig. 6.12, the accuracy decreases with the dilepton masses. More MC samples are needed to obtain the same statistical error as data. These results are transferable to this work as dilepton final states are studied in the reference and this paper To reduce the MC over data statistical error ratio to 10% for 36 fb^{-1} data, an additional number of $\mathcal{O}(10^9)$ extra MC events are required, which is impractical. A heuristic solution, fitting functional form approach is chosen to avoid expensive computation thus improve the overall sensitivity particularly at low mass. However, this heuristic approach introduces a layer of model dependence, as the chosen functional form may not fully encapsulate the true background behavior. The functional form is affected by the systematic and statistical error of the data. On the contrary, with unlimited computational resource, the MC simulation can hypothetically reduce the statistical error of the background model.

6.3.1 Dielectron data-driven background estimation

The e^+e^- background is mostly contributed by Drell-Yan process, top-quark ($t\bar{t}$), single-top-quark and diboson productions [7]. The functional form we have chosen exhibits good stability during extrapolation, meaning does not behave nonphysically when applying. The functional form is given by:

$$\begin{aligned} f_{ee}\left(M_{\text{reco}}\right) &= N \cdot f_{\text{BW},Z}\left(M_{\text{reco}}\right) \cdot (1-x)^b \cdot x^{p_0+p_1\cdot\ln(x)+p_2\cdot\ln(x)^2+p_3\cdot\ln x^3}, \\ f_{\text{BW},Z}\left(M_{\text{reco}}\right) &= \frac{\Gamma_Z}{\left(M_Z-M_{\text{reco}}\right)^2+\Gamma_Z^2}, \end{aligned} \tag{6.19}$$

$x = M_{\text{reco}}/\sqrt{s}$ is the fractional energy possessed by the reconstructed particle with $\sqrt{s} = 13$ TeV, $f_{\text{BW,Z}}(M_{\text{reco}})$ is the non-relativistic Breit-Wigner function of Z boson with $M_Z = 91.1876$ GeV and $\Gamma_Z = 2.4952$ GeV. For more examples of other functional forms candidates and the selection processes, please refer to the Appendix of [7]. The form $\sum_{i=0}^{3} x^{p_i\cdot\ln x^i}$ is originally used by searches for new physics in dijet final states, it is also shown the form is flexible to fit other physics-motivated distributions [50]. The term $(1-x)$ constrains the background fit evaluates to zero when the M_{reco} approach center of mass energy, ensure the fitting do not exceed expected collision energy. The fitting parameters for Eq. 6.19 we used are $N = 0.24547$, $b = 1.5$, $p_0 = -12.38$, $p_1 = -4.29$, $p_2 = -0.919$ and $p_3 = -0.0845$. A bin width of 1 GeV is used in both data and simulation [7]. The functional fit to and that with Poisson fluctuation can be seen in Fig. 6.13.

6.3.2 Diphoton data-driven background estimation

The $\gamma\gamma$ background can be categorized as *reducible* and *irreducible* background. The irreducible background are represented by $\gamma\gamma$ events containing two prompt photons originated from SM production directly. The reducible background is represented by $\gamma\gamma$ events containing one reconstructed photon and one prompt photon; or two reconstructed photons. The reconstructed photon candidates are from different physics objects, mainly from jets [45]. In high-mass searches, it can be greatly reduced by suit-

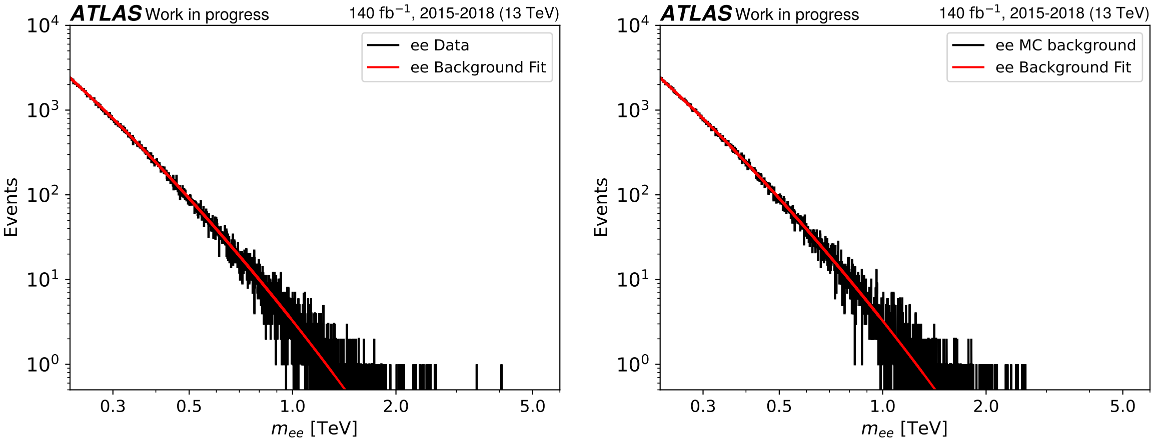

(a) (b)

Figure 6.13: (a) The e^+e^- data fit with invariant mass between 225 GeV and 6 TeV obtained from Eq. 6.19. (b) The data driven background estimate is obtained by Poisson fluctuation to the fit function.

able choices of photon identification and isolation selections [63]. The non-resonance production of photon pairs ($\gamma\gamma$) form the largest background, followed by a photon with a misidentified photon (γj) and two misidentified photon (jj). To model the total background shape, we first modeled the reducible background shape with MC simulations, then estimated the relative fraction between reducible and irreducible background. Due to the nature of limited statistics, different methods are applied to reducible and irreducible background separately. MC simulations are used to estimate the shape of irreducible background; data-driven method is used to estimate that of the reducible background. The relative proportionality of two background can be estimated with 2x2D sideband decomposition method, a data-driven method to evaluate the $\gamma\gamma$ signals, background yields and the fake rates [63]. It extrapolates the background from control regions located in the sidebands of identification and isolation to the signal region, forming a 2D variables plane. The amount of signal and background in the signal region can be modeled as a function of signal efficiencies, background fake rates and correlations, in addition, the aforementioned proportionality can be determined.

The simulation procedure is recorded in [17]. SHERPA 2.2.4 is used to generate reducible signals with the default tune setting, neglecting any resonance signal ($X \rightarrow \gamma\gamma$) interference. The γj events were modeled up to next-to-leading order(NLO) in the strong coupling constant α_s, and the jj events were modeled up to leading order (LO) in the SHERPA parton shower according to the MEPS@NLO procedure [64]. NNPDF3.0 NNLO parton distribution function set is used [65].

Full simulation of the detector responses to the very large MC samples are computationally expensive, an approach namely fast simulation is applied [66]. In this approach, the detector responses towards the MC samples are replaced with a functional form with parametrization [67]. Partial full-simulation samples are created to verify the fast-simulation results. The samples cover the mass range of 175-2000 GeV, around 35 millions events are generated. The functional form used to fit the background is:

$$f(x) = N \cdot (1 - x^{1/3})^b x^{\sum_{i=0}^{n} p_i (log x)^i}. \tag{6.20}$$

The physical interpretation is similar to the e^+e^- case. The best fit parameter values are $N = 2.36$, $b = 10.468$, $p_0 = -1.8375$, $p_1 = 0.1378$. The functional fit to data and that with Poisson fluctuation can be seen in Fig. 6.14.

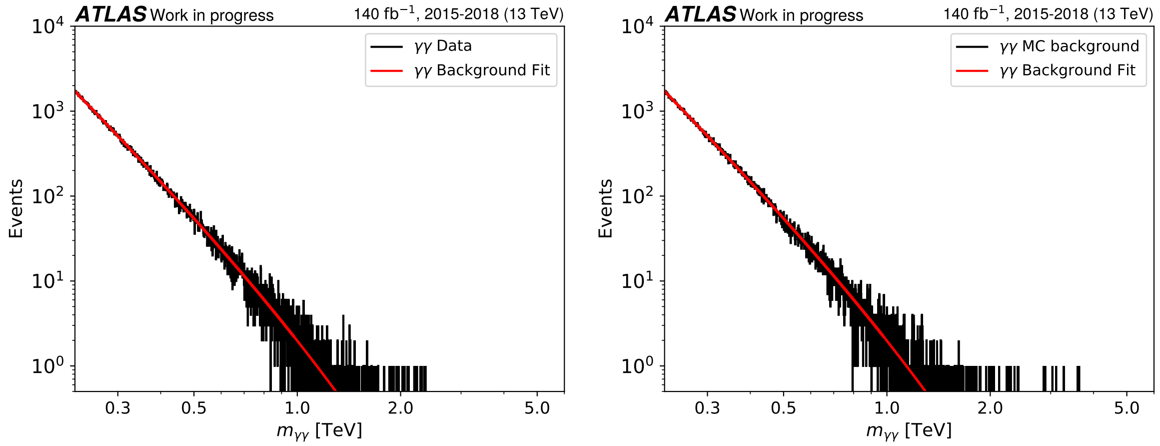

(a) (b)

Figure 6.14: (a) The $\gamma\gamma$ data fit with invariant mass between 225 GeV and 6 TeV obtained from Eq. 6.20. (b) The data background estimate is obtained by Poisson fluctuation to the fit function.

Chapter 7

Fourier Transform

In this section, we discussed key aspect of the Fourier transform (FT) and its application in this analysis. The FT analysis on the MC signals are described as mentioned in Ch. 6. FT analysis is used because the signal invariant mass spectra show three unique properties which can be encapsulated by a FT. First, there are multiple resonance peaks in the invariant mass spectrum. Even if the spectrum is not truly periodic ($\mathcal{F}(x+a) = \mathcal{F}(x)$) for all invariant mass x and period a, the signals after including detector effects show oscillation properties which are measurable if strong enough. Second, the resonance peaks are 'localized' in the invariant mass spectrums. The peaks are not spread over the whole spectrum, but are concentrated in a small region. If the FT is applied to a non-oscillating region where signals do not exist (*i.e.,* the region x where $x < k$) the amplitude of the FT is expected to be smaller, thus offering a primitive distinguishing power on the minimal values of k. Thirdly, the unique mass separation between gravitons of different mode are determined in Eq. 2.10. The mass separation between the nth and $(n-1)$th peaks is $(n^2 - (n-1)^2)/R^2$ where n is an integer. The compactification radius R can be solved when the unique frequency determined.

7.1 Fourier Transform methodology

The FT is a mathematical operation that transform a signal into its frequencies components, providing insight into its frequency domain characteristics, applicable to both continuous and discrete signals.

Our focus lies in the power spectrum, which is the square of the magnitude of the Fourier Transform, $P(\xi) = |\mathcal{F}(\xi)|^2$, and provides insights into the distribution and strength of frequencies in the original signal.

For a continuous distribution, with limited range $[x_{min}, x_{max}]$, the power spectrum becomes:

$$P(\xi) = |\mathcal{F}(\xi)|^2 = \left| \frac{1}{\sqrt{2\pi}} \int_{x_{min}}^{x_{max}} f(x) e^{-i2\pi x\xi}\, dx \right|^2 . \tag{7.1}$$

Applying the power spectrum equation to our invariant mass spectrum, where the signal function is represented by the differential cross-section $d\sigma/dm$, the frequency is $1/T$ and the period is T, we obtain

$$P(T) = \left| \frac{1}{\sqrt{2\pi}} \int_{m_{min}}^{m_{max}} \frac{d\sigma}{dm} \exp\left(i \frac{2\pi g(m)}{T} \right) dm \right|^2 . \tag{7.2}$$

An arbitrary function $g(m)$ is purposely used instead of m, as discussed above, the mass spectra peak amplitudes are not constantly spaced, and the period is not constant, hence not truly periodic. Due to the nature of measurement in the detector, the invariant mass spectra can only be shown as histogram, thus a binned histogram will be used, discretization of Eq. 7.2 is needed. A practical use of Eq. 4.1 is $N = \sigma\epsilon AL$ where n is the number of observed event in the detector, A is the acceptance and ϵ is the efficiency of detector and decay channels discussed in Ch.4. Substitute $\sigma = n/(AL\epsilon)$ into Eq. 7.2 we obtain:

$$P(T) \sim \left| \int_{m_{min}}^{m_{max}} dm \frac{1}{L} \frac{dN/(\epsilon A)}{dm} \exp\left[i \frac{2\pi g(m)}{T} \right] \right|^2 , \tag{7.3}$$

the overall constants are removed, and the discretized form is

$$P(T) \sim \left| \sum_{i_{min}}^{i_{max}} N_i \exp\left[i \frac{2\pi g(m_i)}{T} \right] \right|^2 , \tag{7.4}$$

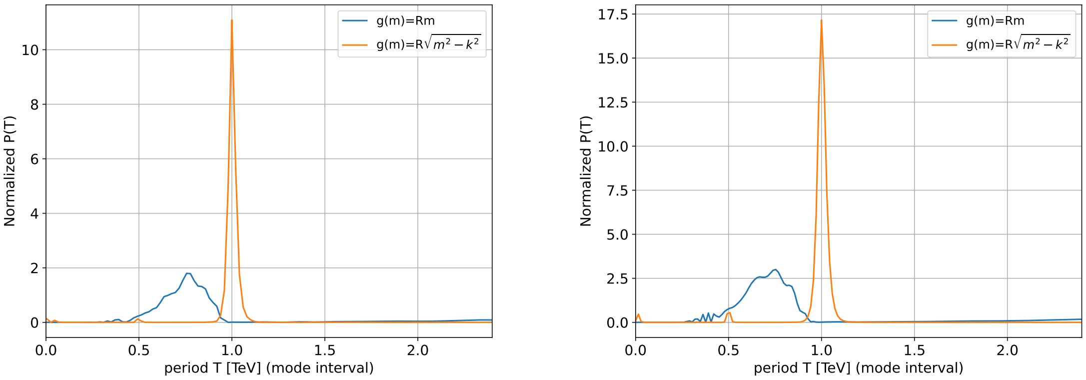

$k = 0.5$ TeV $\quad M_5 = 6$ TeV

$k = 1$ TeV $\quad M_5 = 6$ TeV

Figure 7.1: A performance comparison of the normalized power spectrum in the model-independent search and the model-dependent search in e^+e^- channel. The model-independent function is $g(m) = m$, and the model-dependent function is $g(m) = R\sqrt{m^2 - k^2}$. The period of the signal is defined in the 'mode' space instead of the invariant mass spectrum. Background subtraction is applied to both cases.

normalizing to unity by dividing the sum of squares of the number of events, and the final form is:

$$P(T) = \frac{\left|\sum_{i_{min}}^{i_{max}} N_i \exp\left[i\frac{2\pi g(m_i)}{T}\right]\right|^2}{\sum_i N_i^2}. \tag{7.5}$$

Different choices of $g(m)$ could improve the sensitivity of the power spectrum without losing the insight of the FT. The physical interpretation of period T depends on the choice of $g(m)$. Applying the FT to the signal spectra are expected to obtain a peak at T the period of the signal. The peaks are expected to be narrower and with higher amplitude if the signal is distinct and strong. Two choices of $g(m)$ are discussed in this thesis, the model-independent search (section 7.1.1) and the model-dependent search (section 7.1.2). To enhance the sensitivity of the method, either model-dependent or model-independent, a background subtraction is applied. Every MC signal plus background sample has the background subtracted before applying the FT. The difference between with and without background subtraction is discussed later.

7.1.1 Model-independent Fourier transform

For the model-independent search, one can follow the standard FT and define $g(m) = m$ or $g(m) = m - k$ for better visibility. It is still model-independent because shifting the mass spectrum will not affect the frequencies of the waveform. The peak in the power spectrum of the graviton signals are expected to widen, as the gaps between peaks in the invariant mass spectrum is increasing throughout the spectrum, the period of the signals are not well-measured. Hence, inducing uncertainty to the corresponding (k, M_5). The accuracy of information that can be extracted from the power spectrum is not optimized.

Its validity is tested by injecting pure sinusoidal waves into the e^+e^- background only MC sample. Invariant mass range of [150, 2360] GeV is considered. Different mass periods are used to create the sinusoidal signals, and the DFT is applied to the sample. Fig. 7.2 shows the result of the injection test. The model independent FT is sensitive to the sinusoidal signals, waves with small period can be captured accurately. Also, when the period of the waves approaches the range of the invariant mass, the sensitivity is lost as expected. The performance of model-independent transform of MC graviton signals is shown in Fig. 7.1. The sensitivity of model-independent approach is clearly lower than the model-dependent approach. The discovery significance and exclusion limit do not use this approach, but still some testings are done in the following discussions.

7.1.2 Model-dependent Fourier transform

For the model-dependent search, we utilize the equation of mass spectrum Eq. 2.10 and define $g(m) = R\sqrt{m^2 - k^2}$. Such definition provides physical meaning to the period T, making T live in the 'mode space' instead of the 'mass space'. It allows an increment of integer 1 when calculating $g(m_{n+1})$ from $g(m_n)$, where m_n is the nth resonance peak. Since the peaks in the spectrum are contributed only by the resonances at different modes, the gap between the peaks are integer multiples of

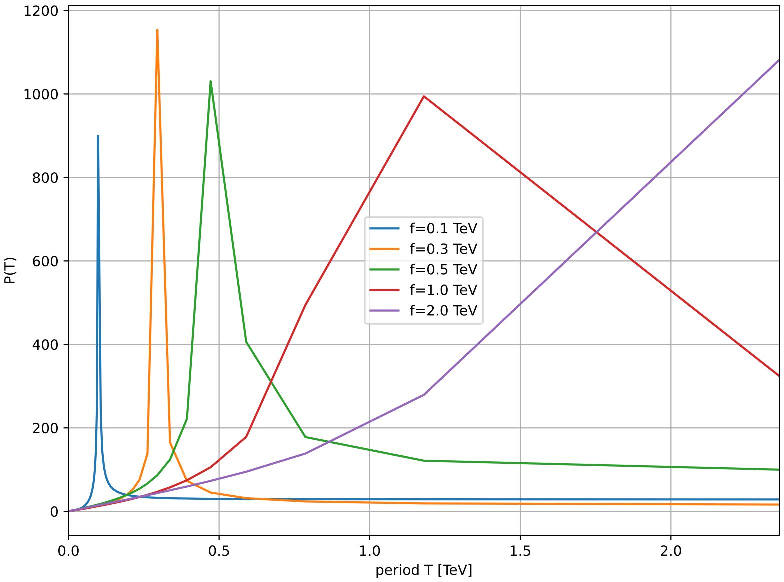

Figure 7.2: The injection test of the model-independent FT. The sinusoidal waves are injected into the e^+e^- background only MC sample. The DFT is applied to the sample.

the fundamental frequency $1/T$. That is, a peak at $T = 1$ in the power spectrum is expected. The performance analysis in the normalized power spectrum is shown in Fig. 7.1. In the $k = 1$ TeV case, we also observe the effect of aliasing in the model-dependent FT. Aliasing occurs at $T = j$ where j is an integer but $j \neq 1$, this is a well-known issue that arises when a signal is insufficiently sampled, leading to the misrepresentation of higher frequencies as lower ones. However, they are unimportant as the fundamental frequency always dominate the spectrum, we can focus in the vicinity of $T = 1$. It is not observed in model-independent case due to the fact that the signal is not periodic in the $g(m) = m - k$ model, no clearly defined frequency is present in the power spectrum and aliasing cannot be observed.

A stand-alone program is written and discrete Fourier Transform (DFT) is employed instead of Fast Fourier Transform (FFT). One requirement to apply FFT is that the signal counts are binned evenly. Fig. 7.3(a) shows the signal distribution in the $g(m)$ space. During the employment of $g(m) = R\sqrt{m^2 - k^2}$, the signal counts are no longer binned evenly in the mode space, but rather more concentrated at higher

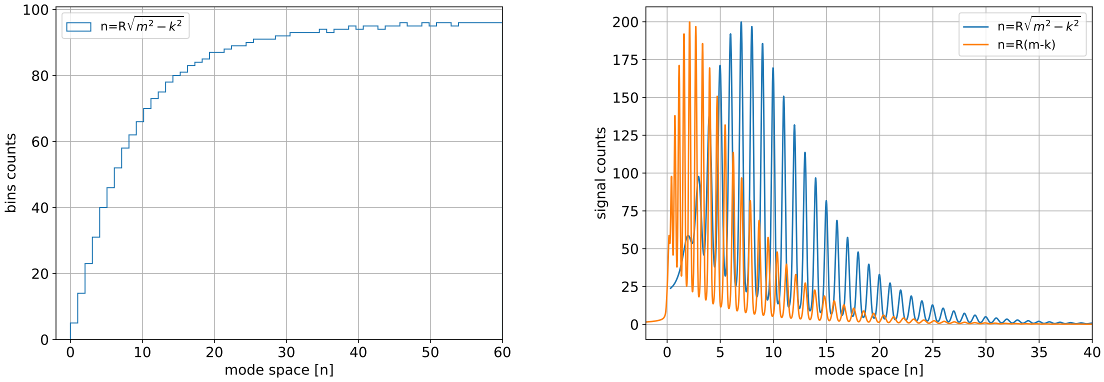

(a)

(b)

Figure 7.3: (a) A demonstration of the non-uniform sampling in the mode space when model is applied. (b) A comparison of signal profile shape after employing different models, $(k, M_5) = (1, 6)$ TeV is used for both figures.

masses, and dispersed at lower masses. The signal profile shape of different models is shown in Fig. 7.3(b) to demonstrate the difference gap spacing between peaks.

Fig. 7.4 demonstrate the results of the power spectrum of the transferred MC simulated signals at $k = 1$ TeV and $M_5 = 6$ TeV. The peak position determines

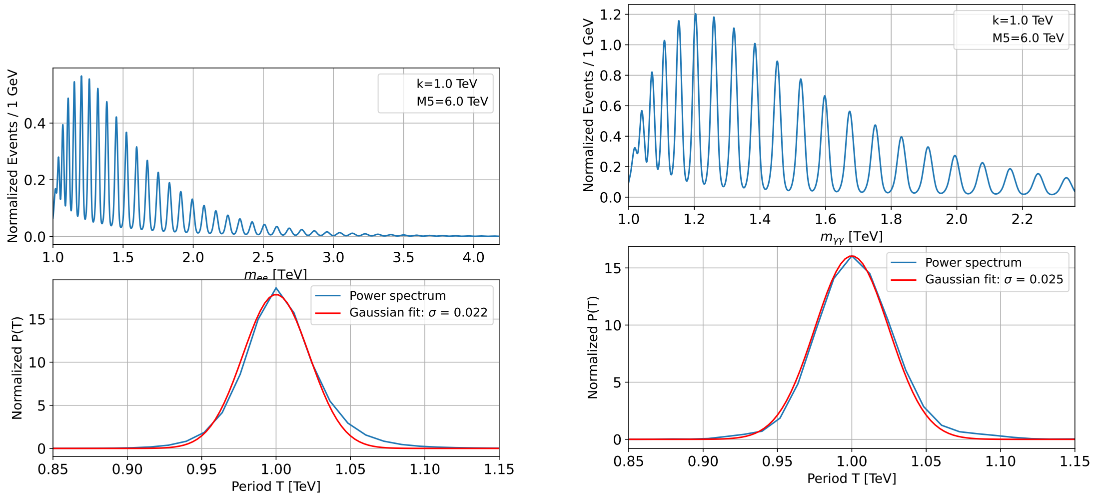

(a) e^+e^-

(b) $\gamma\gamma$

Figure 7.4: Example plots of the power spectrum and the Gaussian fit of the MC signals at $k = 1$ TeV and $M_5 = 6$ TeV.

the period in the mode space, and the width of the peak determines the uncertainty of the period. The width characterized the uncertainty of period because a wider width is equivalent to the peak is less distinguishable along the frequency axis, the power spectrum is more flatten. After the Poisson fluctuation is implemented into the MC samples, a more flattened power spectrum has higher chance to peak at position other than $T = 1$. They are generally encapsulated at vicinity of the peak with very limited number of points, a fitting approach is used to smoothen the curve and obtain the peak position and width. We fit the power spectrum with a Gaussian function $f(x) = \frac{A}{\sqrt{2\pi}\sigma} e^{\frac{-(x-\mu)^2}{2\sigma^2}}$, where the μ is the peak position fixed at 1; σ is the width of the peak, to obtain period and uncertainty correspondingly, and the amplitude A. One may argue that a possible way to obtain the amplitude A is to search for the maximum amplitude while not fixing the peak position μ at 1, then the uncertainty can be quantified with $\delta\mu$ from the fitting. Indeed, fixing $\mu = 1$ introduced statistical bias to the amplitude A, but this is a trade-off between the variance of the peak position and the amplitude. If μ is not fixed, the variance of peak position will be very large, and even end up losing its physical meaning in the CW/LD model. The search will be nullified if the variance is too large, therefore a trade-off between bias and variance is needed. σ is a nuisance parameter that is not affected by the bias, it is not as important as μ in the analysis. The width of the MC signal becomes versatile after Poisson fluctuation, σ can capture the uncertainty of that particular sample. However, it was later found that in high energy region $m \leq 2$ TeV, little samples in data are available, interpretation of the width is questionable. There are two approaches to address the low statistics issue in data at high energies, one is to use the MC signal width to fix the width of the Gaussian fit in data, the other is to leave the width as a free parameter in the fit. Both methods were found to potentially and incorrectly fit the data resulting a wrong Gaussian amplitude, either through strong bias if width is fixed, or large variance if width is free. The width of the Gaussian fit is free in this analysis. An improvement is possible by fixing the widths using MC simulated data.

MC experimental result is obtained by normalizing the samples to the luminosity, cross-section and the branching fraction, which is also shown in Fig. 7.4. Fig. 7.5 shows a comparison of the power spectrum with the same model with and without the detector effect. The graph is obtained by applying the model-dependent FT on the MC signals at different values of (k, M_5). To have better comparison, we normalized the MC signals, and scale down the power spectrum with a coefficient obtained by fitting a Gaussian at vicinity of $T = 1$. The graph shows that the smearing effect due to the detector widen the width around the peak, causing a higher uncertainty of

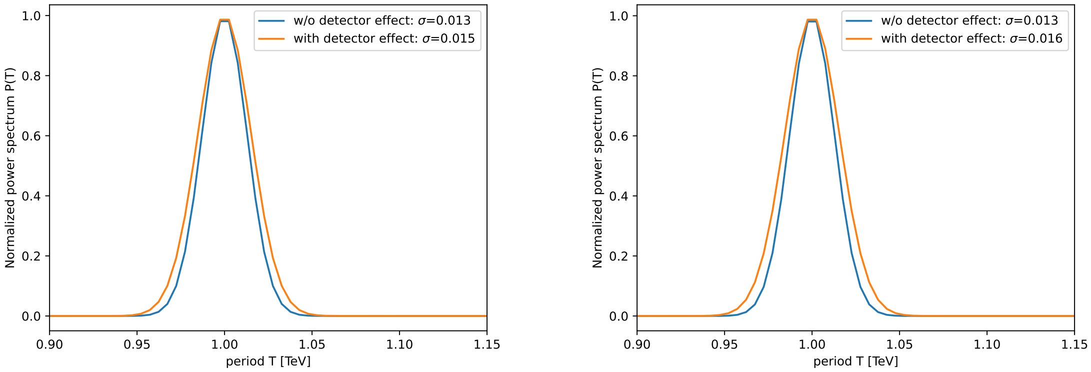

$k = 0.3$ TeV $M_5 = 1$ TeV

$k = 0.3$ TeV $M_5 = 6$ TeV

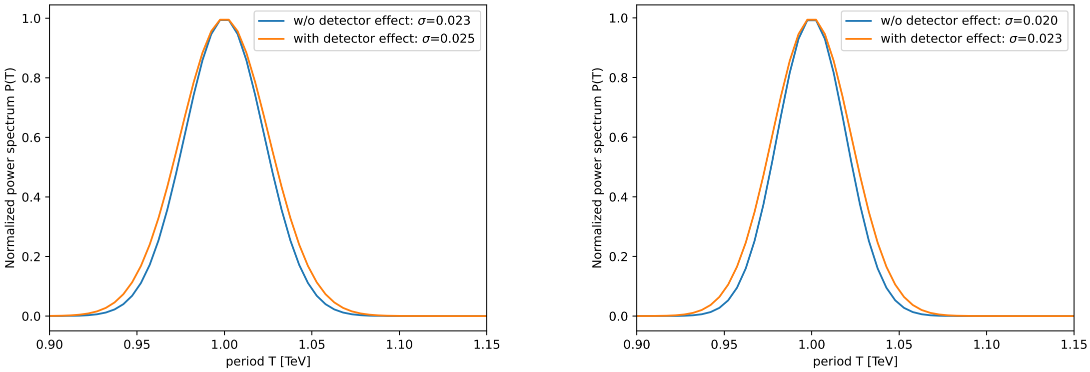

$k = 1$ TeV $M_5 = 1$ TeV

$k = 1$ TeV $M_5 = 6$ TeV

Figure 7.5: The normalized power spectrum model-dependent $(g(m) = R\sqrt{m^2 - k^2})$ FT of the MC signals at different values of (k, M_5). We focused at T=1 $\pm$ 0.15 TeV, and the Gaussian width σ is listed in the legend.

the period. We also observe that wider Guassian widths in higher k as there are less resonance peaks. In Fig. 7.5 we can see the power spectrum the resonance is wider as k increases. It is more difficult to detect the graviton signals and its properties at high k with FT analysis.

7.2 Fourier transform with background subtraction

Here we first discuss the effect of with and without background subtraction. Fig. 7.6 shown the comparison of the transform result with and without the nominal background subtraction. We see the power spectrum with background subtraction has a narrower width, thus less statistical uncertainty.

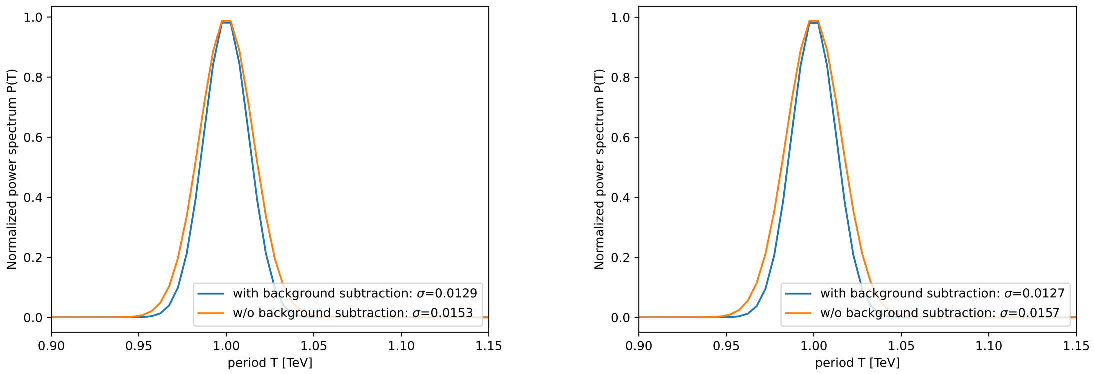

$k = 0.3$ TeV $M_5 = 1$ TeV $\quad$ $k = 0.3$ TeV $M_5 = 6$ TeV

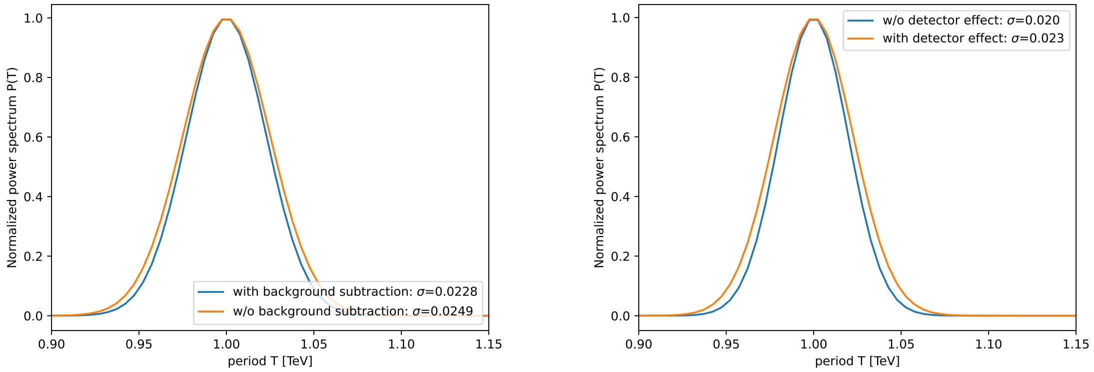

$k = 1$ TeV $M_5 = 1$ TeV $\quad$ $k = 1$ TeV $M_5 = 6$ TeV

Figure 7.6: This shows that the background subtraction can reduce the statistical uncertainty. The normalized power spectrums of the MC signals at different values of (k, M_5) are plotted. The Gaussian width σ is listed in the legend.

Chapter 8

Statistical methods

This section discusses the general statistical methodology to compare the CW/LD model predicted with data. We introduce the concepts of the test-statistics, local p-value, global p-value and hypothesis test. The methodology will be employed to establish the discovery potential of the model and the exclusion limit at a 95% confidence level based on frequentist statistics.

8.1 Hypothesis test

Hypothesis testing is a statistical method used to determine whether a hypothesis is consistent with the data using the likelihood function L [59]. The likelihood function on its own cannot conclusively validate or refute a hypothesis since the value of it can be arbitrarily large or small. Therefore, this function is extended to compare the agreement between two or more hypotheses and experimental measurements. A null hypothesis H_0 is defined for the background expectation (SM), and an alternative hypothesis H_1 for the expectation of the signal plus background (BSM). According to the Neyman-Pearson lemma [69], the likelihood ratio: $\lambda = -2\ln\left(\frac{L(H_1)}{L(H_0)}\right)$ is an optimized quantity that indicates the distinction of two hypotheses. This ratio froms the basis of the test statistic t, which follows a probability distribution function under each hypothesis.

Fig. 8.1 provides a schematic plot of two test statistic distributions base on H_0 and

H_1. This illustrates how two hypotheses change the distribution of t. In hypothesis testing, t is chosen to minimize the probability (α also known as *Type I Errors*) of rejecting H_0 when it is preferred, and the probability (β also known as *Type II Errors*) of fail to reject H_0 when it is unfavored and H_1 is preferred. Eq. 8.1 shows the mathematical definition of α and β.

$$\begin{aligned}
&P\left(t \in \kappa | H_0\right) = \alpha, \\
&P\left(t \notin \kappa | H_0\right) = 1 - \alpha, \\
&P\left(t \in \kappa | H_1\right) = 1 - \beta, \\
&P\left(t \notin \kappa | H_1\right) = \beta.
\end{aligned} \tag{8.1}$$

For a given threshold, α is defined with respect to H_0, and β are defined with respect to H_1. The rejection of H_0 only suggests data inconsistency with H_0, not necessarily indicating consistency with H_1, only relatively in favor to H_1. Conversely, failing to reject H_0 due to insufficient evidence does not automatically validate H_1. Additionally, α and β are not independent; choosing a test statistic involves a trade-off between these two error types.

For this search, H_0 is defined as the SM only background and H_1 as the clockwork model with given (k, M_5) with the SM background. A discovery is predicated on defining a critical region in the PDF ($t > \kappa \mid H_0$) for a specific κ. If t resides within this critical region, H_0 is rejected. This leads to the definition of the p-value. Assuming that $t = t_\nu$ is found, the p-value equals the area in the PDF where ($t > t_\nu$).

The principles discussed above are applicable to our binned sample. We assumed the bin content is independent on any other bins thus following a Poisson distribution. The definition of the test statistics will be discussed in the next section, here we assume it is obtained from MC using the search techniques discussed in Ch. 9. Adding Poisson fluctuations to the MC samples generates a PDF that follows $f(t|\mu, \vec{\theta})$. Suppose a measurement yields a single value of t_{obs}, the measurement can be obtained from MC simulated data, data or the median of the PDF ($\int_{t_0}^{\infty} f(t|\mu = 0, \vec{\theta}) dt = 0.5$).

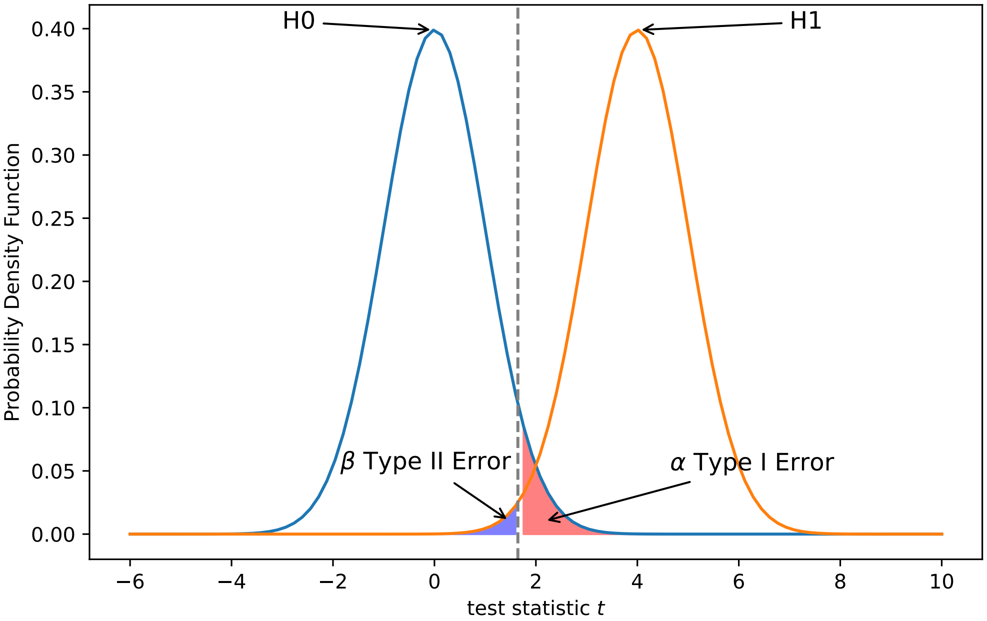

Figure 8.1: Schematic plot of two test statistics distributions base on H_0 and H_1, where α and β are the probability of rejecting H_0 when it is preferred and the probability of fail to reject H_0 when it is unfavored, respectively.

The p-value of the measurement is given by

$$P_{\text{obs}} = \int_{t_{\text{obs}}}^{\infty} f(t|\vec{\mu} = 0, \vec{\theta})dt. \tag{8.2}$$

Referring to the situation in Fig. 8.1, the smaller the P_{obs} value, the more inconsistent the measurement is with H_0, suggesting favor towards H_1.

8.1.1 Discovery potential

The established framework for hypothesis testing serves two critical purposes in this investigation. Firstly, it sets a discovery potential, and secondly, it establishes an exclusion limit on the parameter space of the CW/LD model. For a discovery, H_0 must be rejected, and the probability which H_0 is rejected when it is preferred should be minimized, *i.e.*, $p_{\text{obs}} < \alpha$. Conventionally, the p-value is expressed in terms of Gaussian standard deviations, equivalently degree of significance, Z. Significance is defined as the inverse of the cumulative distribution function to find the z-score corresponding to a given p-value in a standard normal distribution.

$$Z = \Phi^{-1}(1 - p_{\text{obs}}), \tag{8.3}$$

where Φ is the cumulative distribution function of the standard normal distribution, the Z value is also known as the significance of the measurement. In the thesis, the p-value obtained with above method is denoted as local p-value. It does not take into account an effect namely look-elsewhere effect [70]. The look-elsewhere effect becomes important when scanning through a range of parameters, in our cases, a range of invariant masses. Probabilistically, there will be one out of twenty mass bins potentially significant regardless the physics if we set the threshold $\alpha = 0.05$. One straight forward way to estimate the look elsewhere effect is simply calibrated the p-value with the distribution obtained by running background only MC simulations, and find the test statistics with the largest fluctuation that could be mistaken for true signal. However, to collect 5σ of effects, (10^7) MC simulations has to be conducted solely for this purpose. Sidak correction [71] is another way to estimate the look elsewhere effect, which is a native but effective approach. Intuitively, the global p-value is the probability of observing at least one significant excess anywhere in the range, and it is related to the local p-value by:

$$\text{global } p = 1 - (1 - \text{local } p)^N, \tag{8.4}$$

where N is the degrees of freedom, in the simplest case where every bin is independent, it is the number of bin. The meaning of N in this thesis will be discussed in Chapter 9.

8.1.2 Exclusion limit

Often, the significance of a possible signal is not high enough to claim a discovery, but also insufficient to exclude the H_1 hypothesis. In such scenarios, we aim to determine how likely the measurement aligns with the H_1, and identify the range of parameters $(\mu, \vec{\theta})$ for the theory that are consistent with the search. The procedure of constructing the exclusion limit is known as Neyman construction or CL_{s+b} [72]. Given that the hypothesis test enables quantifying the measurement's consistency with the background-only hypothesis, it can also be utilized inversely to determine the consistency of the measurement with the signal-plus-background hypothesis. Remember the statistical interpretation of β, which is the probability of failing to reject H_0 when it is false, and H_1 is true. The aim is to identify μ_{cut} for each (k, M_5) such that there is a $\beta = \beta_{\text{cut}}$ chance that H_1 is consistent with the measurement, given the threshold t_{obs} We can also illustrate a $1 - \beta_{\text{cut}}$ confidence interval on μ, indicating that the correct value of μ lies within the interval $(0 \leq \mu \leq \mu_{\text{cut}})$ with a $1 - \beta_{\text{cut}}$ probability. To circumvent the introduction of human bias in the MC simulation stage, the data is not used to draw the threshold. Instead, we set t_{obs} as the median of the PDF $f(t|\mu = 0, \vec{\theta})$, assuming the data is a realization of H_0. In ATLAS, β_{cut} is set to be 0.05, and a 95% confidence interval is used to establish the 95% expected (upper) exclusion limit.

The expected limit and its corresponding upper/lower bound are essentially a measure of the experiment's sensitivity. The boundary can be set by finding the corresponding μ_{cut} when t_{obs} is set to be the $\pm 1\sigma$ or $\pm 2\sigma$ of the median of the PDF $f(t|\mu = 0, \vec{\theta})$. If the observed limit from data is significantly stronger or weaker than the expected limit, it suggests a few possible explanations. The divergence between observed and expected results could be attributable to various factors, such as random variations in the data, inaccuracies in error estimation, or overlooked systematic errors. Therefore, it is imperative to subject any such discrepancies to thorough examination.

Conversely, if the observed limit aligns with the expected limit, this indicates that the data behaves as expected under the null hypothesis. The terminology used in this discussion adheres to statistical conventions. Physicists determine the exclusion limit by setting H_0 as $L(\mu)$ and H_1 as $L(0)$, and look for the $1 - \alpha$. This is equivalent to the Type II error in our discussion, which can be discerned by swapping H_0 with

H_1 in Eq. 8.1. A limit on μ is subsequently used in conjunction with a model which predicts μ for a given parameter set. Therefore, a limit on μ effectively establish a limit on the parameters of the model.

8.2 Test statistics t of the FT analysis

The test-statistic t is defined as the amplitude of the Gaussian fit to the FT result at the period of $T = 1$ and no constraint on the width, denoted as below:

$$t_{\mu}^{(k,M_5)} = \log\left(A_{b+\mu s}^{(k,M_5)}(T=1)\right) \tag{8.5}$$

where μ is the signal strength, and background-only test-statistics can be denoted as t_0. The logarithm is taken for convenience and without any loss of generality. To evaluate the statistical uncertainty, we included Poisson fluctuation of all MC signal plus background samples, and subtract with nominal background only samples. The t_0 distributions for different $(k, M_5 = 6)$ TeV are shown in Fig. 8.2.

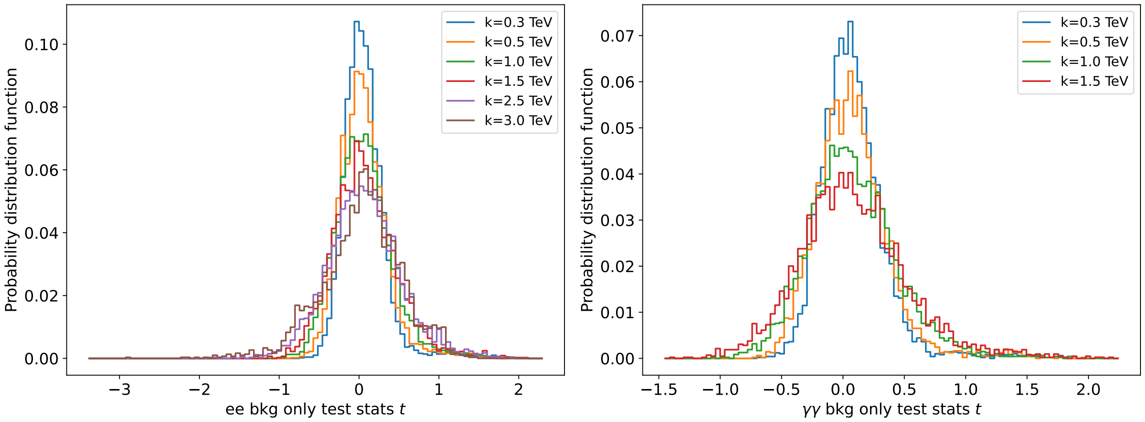

(a) e^+e^- (b) $\gamma\gamma$

Figure 8.2: The test-statisticsistics t of the (fluctuated) background only hypothesis for different k values.

Chapter 9

Analysis

This section shows the results for the model-dependent and the model-independent approach discussed in Ch. 7. Discovery significance for both approaches are discussed. The exclusion limits are discussed for model-dependent approach only. 95 % confidence level exclusion limit of the ATLAS data in ee and $\gamma\gamma$ channels are presented with the expected limit, $\pm 1\sigma$ and $\pm 2\sigma$ statistical uncertainty that obtained from SM background only pseudo-data. Only statistical uncertainties are considered, systematic uncertainties are ignored.

9.1 Discovery significance

Here we demonstrate the discovery power of the method. First we study the difference between the model-dependent and model-independent FT on background-only hypothesis. A pseudo-experiment is conducted and shown in Fig. 9.1. The sample used is the fluctuated background only minus the nominal background, shown in the top panel. The power spectrum of the sample for both model-dependent and model-independent is shown in the middle panel. For this specific experiment, $(k, M_5) = (1, 6)$ TeV is used, other (k, M_5) results are similarly concluded. Each point in the spectrum can be used to calculate t. In the bottom panel, t is used calculate the local p-value of the background-only hypothesis, which is done by comparing the t of the pseudo-experiment and the distribution of t_0 with Eq. 8.2. To calculate the global p-value, we need to determine the degrees of freedom N, it is closely related to the number of bins in the period T. We have to determine the sampling rate of the FT. One might immediately think that as the sampling rate $\frac{1}{\Delta m}$ is 1 GeV^{-1} where Δm is the sampling gap which is also the invariant mass histogram bin width, the Nyquist frequency is then $\frac{1}{2\Delta m} = 1/2$ GeV^{-1}. This is indeed true in the model-independent case, but not in the model-dependent case. To apply FT correctly, the sampling gap should be $\Delta g(m_i) = \Delta g(m_i + 1) - \Delta g(m_i)$. However, as mentioned before and in Fig. 7.3, the sampling after applying model is not uniform. Sampling gap $\Delta g(m_i)$ is not constant, and the Nyquist frequency is not constant either. Here we took the safest approach, using the lowest sampling rate so that the Nyquist frequency is the lowest, which can be obtained from the first two bins after applying the model into the invariant mass spectrum. The sampling rate is 0.88 GeV^{-1} for both channels, the corresponding Nyquist frequency is 0.44 GeV^{-1}. Since we are working with the period T, the minimum T one can probe is $\lceil 1/0.44 \rceil = 3$ GeV, which is the inverse of the Nyquist frequency (highest frequency), And the maximum T (lowest frequency) is $\lfloor 3932/2.27 \rfloor = 1732$ GeV for e^+e^- channel; $\lfloor 2210/2.27 \rfloor = 974$ GeV for $\gamma\gamma$ channel. For this pseudo experiment, the minimal local p-value for e^+e^- is 0.00159 (3.16σ), the corresponding global p-value is 0.934 (0.08σ); the minimal local p-value for $\gamma\gamma$ is 0.00120 (3.24σ), the corresponding global p-value is 0.689 (0.40σ). We can conclude that in this pseudo-experiment, no significant excess is observed for both methods, and the local p-value is consistent with the background-only hypothesis. We have proven the background only hypothesis does not result in a significant spurious signal. Here demonstrate that the FT is sensitive to the signal through signal injection test. Another psuedo-experiment is conducted, where the CW/LD signal is injected to the background only sample, and the FT is applied to the sample. The $(k, M_5) = (1, 6)$ TeV is chosen, signal strength is set to be $\mu = 0.5$ for comparison purpose. The result is shown in Fig. 9.2. Interpretation of graph is similar to Fig. 9.1. A very sharp peak can be observed at $T = 1$, which is the injected signal. This shows

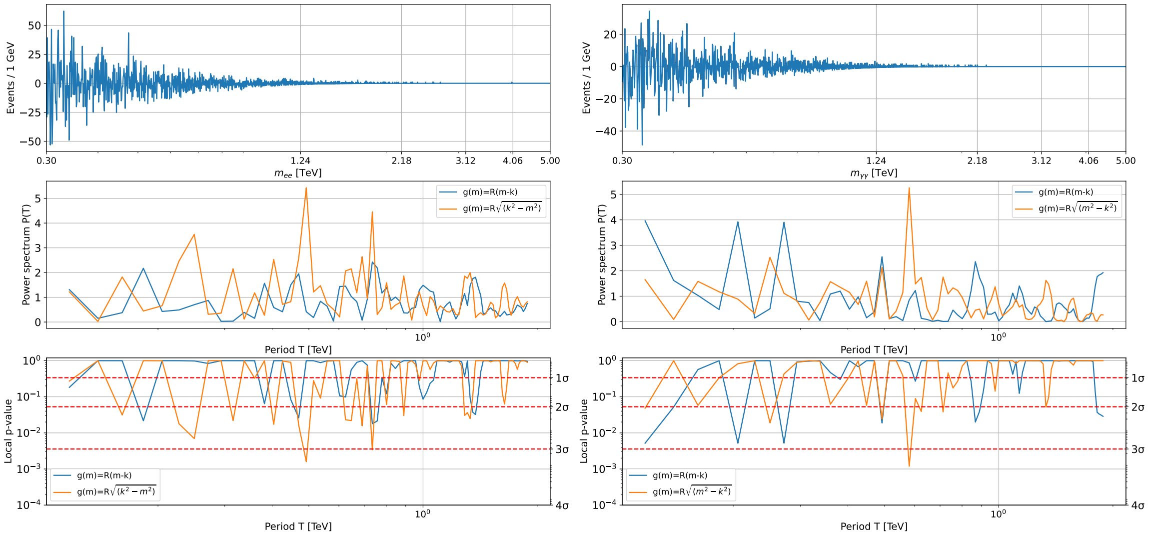

(a) e^+e^-

(b) $\gamma\gamma$

Figure 9.1: The local p-value of the background-only hypothesis. Top panel: Fluctuated background only minus the nominal background only. Middle panel: The power spectrum of the sample. Bottom panel: The corresponding local p-value of the sample.

that the model-dependent FT is sensitive to the CW/LD signal, thus focusing on the vicinity of $T = 1$ is reasonable. Furthermore, it again shows that the model-dependent FT outperforms the model-independent FT.

We also want to show that the FT is most sensitive to the CW/LD signals at matching (k, M_5), and the sensitivity decreases as the (k, M_5) deviates from the matching point. This can be demonstrated by fixing the injected signal samples, and analyze it with different (k, M_5) CW/LD model, particularly focusing around matching points. Fig. 9.3 shows the result of the test. $(k, M_5) = (1, 6)$ TeV is chosen to be the signal model, and we scan through different values k with M_5 unchanged as the CW/LD analysis model. The background fluctuation greatly affects the result, the probability of matching model but with poor statistics is not excluded completely. Therefore, the test results are obtained by running 1000 pseudo-experiments for each point of interest, and taking the medium values of the significance. The analysis method is then statistically most sensitive when the analysis model matches the signal model,

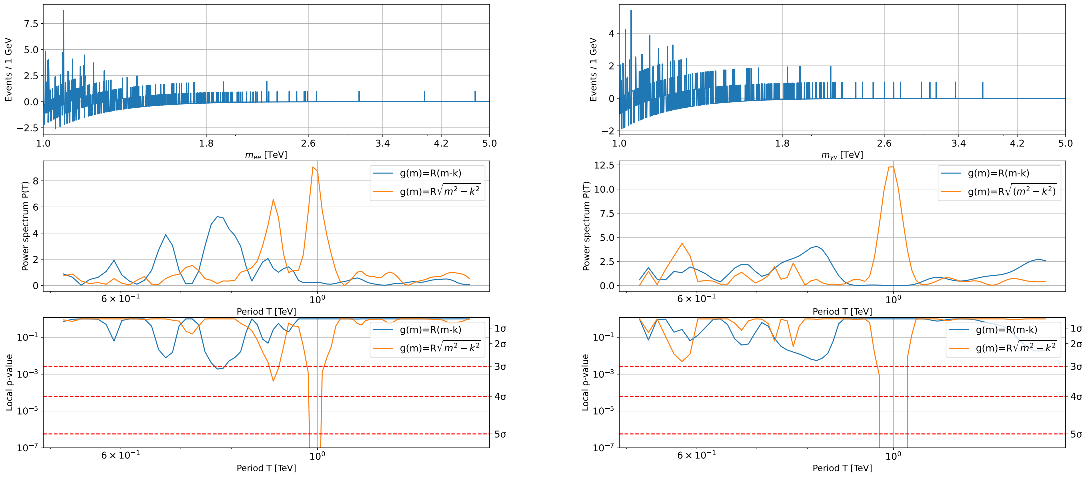

(a) e^+e^-

(b) $\gamma\gamma$

Figure 9.2: The local p-value of the injection test, $(k, M_5) = (1, 6)$ TeV is used. Top panel: Fluctuated signal plus background with nominal background subtraction. Middle panel: The power spectrum of the sample. Bottom panel: The corresponding local p-value of the sample.

and the sensitivity decreases as the analysis model deviates from the signal model.

We have proven the discovery power of the method with MC simulations. We ought to see the discovery statistics of the data in ATLAS. Fig. 9.4 shows the power spectrum of the data in e^+e^- and $\gamma\gamma$ channel, where $(k, M_5) = (1, 6)$ TeV is used. Other results are collectively shown Fig. 9.5. $\pm\sigma$ and $\pm2\sigma$ of the background only t_0 are shown for comparison purpose. The results show that the values of k which the most excess signal is detected. In e^+e^- channel, at k=1 TeV a minimal local p-value of 0.00126 (3.225σ) is observed with a period of 1 TeV, the corresponding global p-value is 0.887 (0.142σ). In $\gamma\gamma$ channel, also at k=1 TeV a minimal local p-value of 0.001897 (3.107 σ) is observed with a period of 0.57 TeV, the corresponding global p-value is 0.843 (0.198σ). For other M_5 values, the results are shown in Appendix G and Appendix H. At all point of interests, none of the observed significance exceeds the 5σ level, thus a discovery cannot be claimed. However, we can still set an upper limit on the signal strength μ at 95 % confidence level.

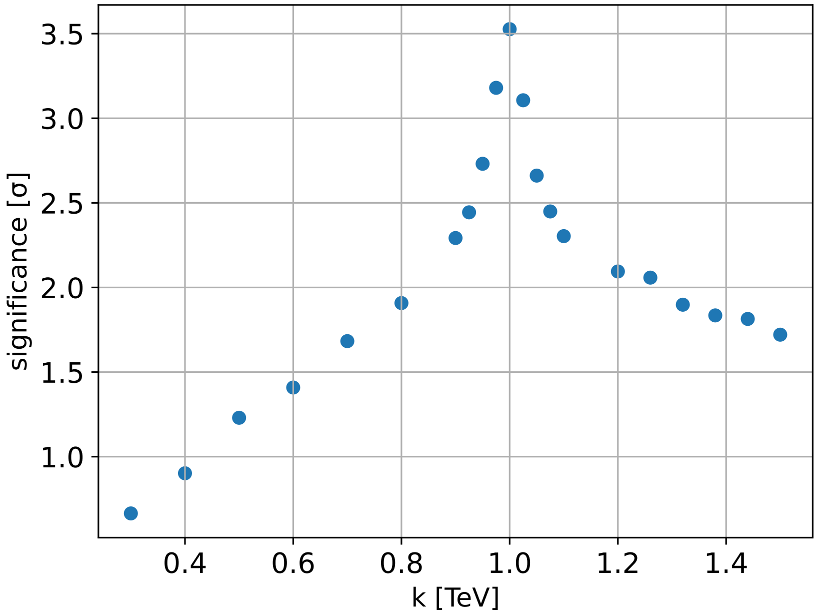

Figure 9.3: The k scanning injection test for CW/LD models. The signal model is $(k, M_5) = (1, 6)$ TeV, and the analysis model is $(k, M_5) = (k, 6)$ TeV. Only e^+e^- channel is shown.

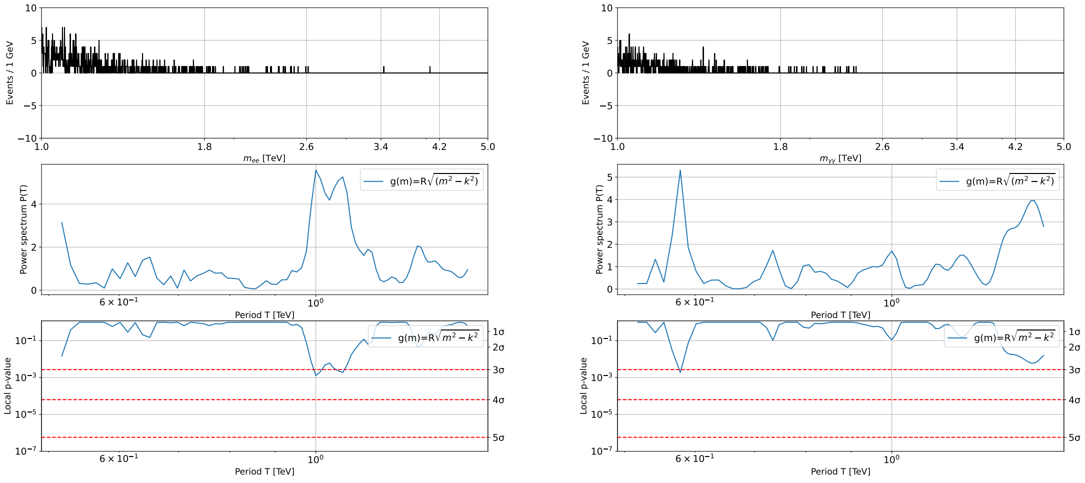

(a) e^+e^-

(b) $\gamma\gamma$

Figure 9.4: The local p-values of the e^+e^- and $\gamma\gamma$ data in ATLAS, $(k, M_5) = (1, 6)$ TeV is used. Top panel: Data with nominal background subtraction. Middle panel: The power spectrum of the sample. Bottom panel: The corresponding local p-value of the sample.

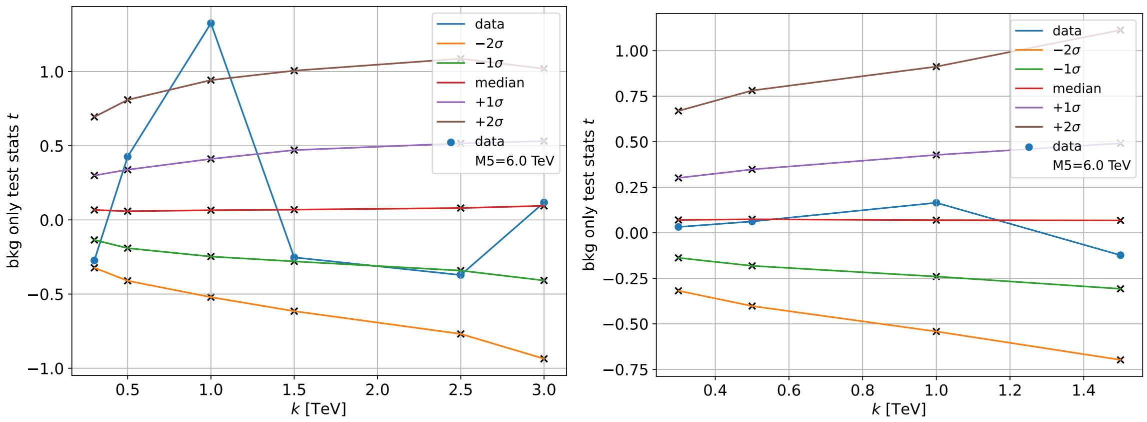

(a) e^+e^-

(b) $\gamma\gamma$

Figure 9.5: The quantiles of distribution of t of the (fluctuated) background only hypothesis for different k values.

9.2 Exclusion limits

Using the statistical method described in section 8.1.2, the results of the exclusion limits using the FT approach are seen in Fig. 9.6 and Fig. 9.7. From the $\gamma\gamma$ invariant mass spectrum, we exclude the values of M_5 below 8 TeV for k of [0.3, 1.5] TeV. Combining with result from the e^+e^- invariant mass spectrum, we exclude the M_5 below 6 TeV to 3 TeV from k of [1.5, 3.0] TeV. Only statistical uncertainty is considered, and the systematic uncertainty is not included. Here we list a few sources of systematic uncertainty, including the uncertainty of the background model, the uncertainty of the signal model, the uncertainty of the detector effect and the uncertainty on the choice of PDF. A non-perturbative region is highlighted in red, where $k \geq M_5$. The result is obtained by searching across the signal strength μ. For each μ, 1000 pseudo-experiments are conducted, a distribution of t_μ is obtained. Referring to the background only t_0 distribution (Fig. 8.2), and the corresponding quantiles (Fig. 9.5), the upper limit of μ is set when the Type II error β is 0.05 at each quantile. Meaning at that signal strength, there are only 5 % chance of failing to reject SM background when the CW/LD model is preferred. We have 95 % confidence that higher signal strength are rejected because they do not agree with the background model that drawn from the data. Increasing the μ would indeed decrease the Type II error, however, we also set a very strict limit on the CW/LD model, leaving no room for further study. The Type I error α also increases as a trade-off.

We converted the upper limit of μ against k to lower limits of M_5 against k ($M_5^3 \propto 1/\mu$) for better interpretation of the dependence between k and M_5. In addition, the interpretation becomes at that M_5, we have 95 % confidence that lower M_5 are rejected because they do not agree with the background model that drawn from the data. The data exclusion limits are consistent with the expected exclusion limits within $\pm 2\sigma$. The $+2\sigma$ are partially cropped out because it offers little information to the result. Although we are setting a limit on the M_5 of the CW/LD model by scanning through different k, the model is unavoidably using M_5 or R which is also M_5 dependent. There is evidence to support the assumption that the M_5 does not affect the exclusion limit intrinsically. In Appendix G and Appendix H, we see the quantile of different M_5 is almost identical, and the M_5 dependence is negligible. Therefore, the background hypothesis is not affected. However, we also see in Fig. 9.6 and Fig. 9.7 that the M_5 observed indeed changed with different M_5 in CW/LD model, but the difference is still within $\pm 2\sigma$. Since the background distribution is not affected by the M_5, the only explanation to the difference is the MC simulated signal used to draw the exclusion limit. The MC signals especially at higher k suffers high statistical uncertainty in signal alone, at higher M_5 signal shape is not affected but the signal amplitude decreases. At lower k and high M_5, the signal is hidden in the large background. The random nature of the fluctuated signal plus background sample has extended to the signal strength μ. The granularity of the signal strength changes vastly because the range of the signal strength is very large, we have to search μ as small as $\mathcal{O}(10^{-4})$ to as big as $\mathcal{O}(10^{2})$. This vast range of granularity makes the $M_5^3 \propto 1/\mu$ dependence very sensitive to the statistical fluctuation.

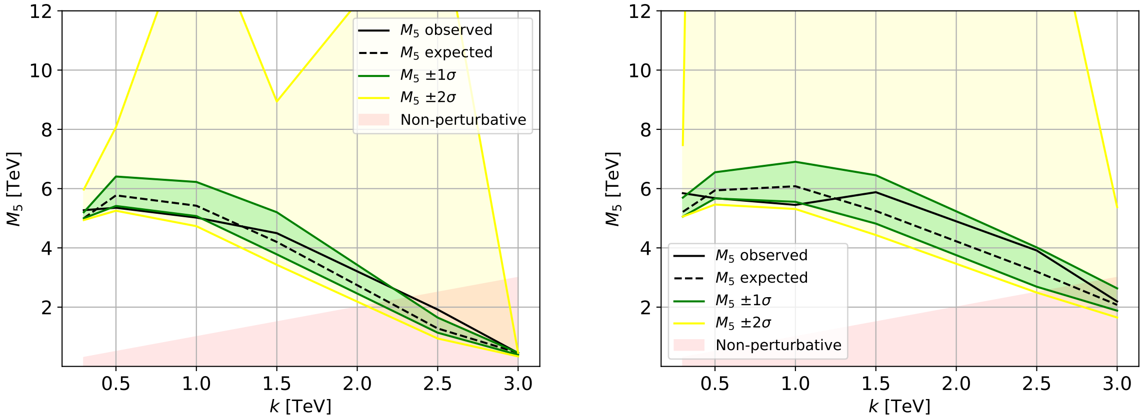

$M_5 = 1.0$ TeV

$M_5 = 2.0$ TeV

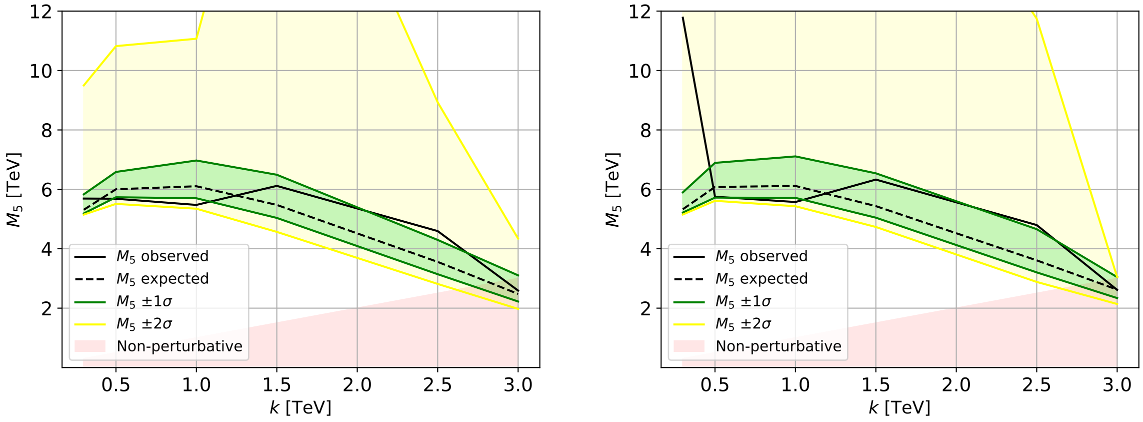

$M_5 = 3.0$ TeV

$M_5 = 4.0$ TeV

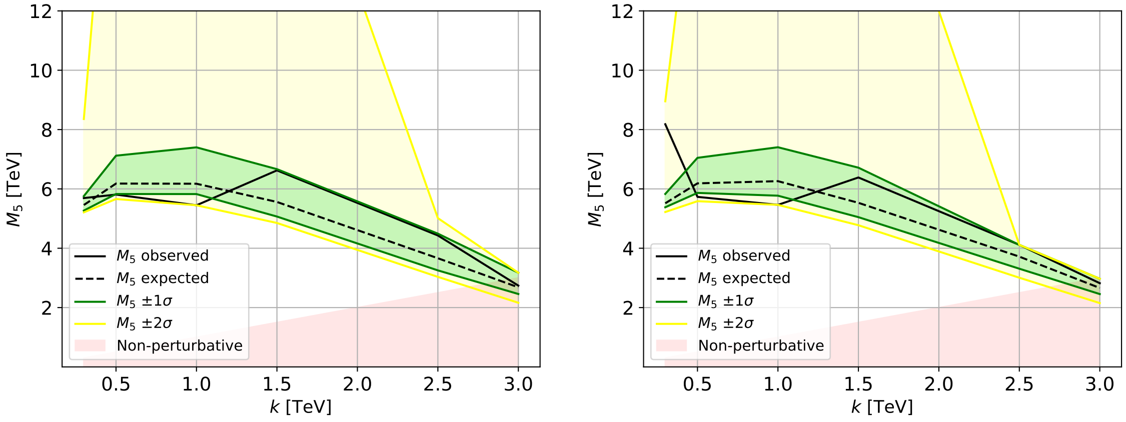

$M_5 = 5.0$ TeV

$M_5 = 6.0$ TeV

Figure 9.6: The expected lower limit exclusion at 95% confidence level using model dependent FT in e^+e^- channel. Data is plotted in black, it is consistent with the expected limit drawn from the background model.

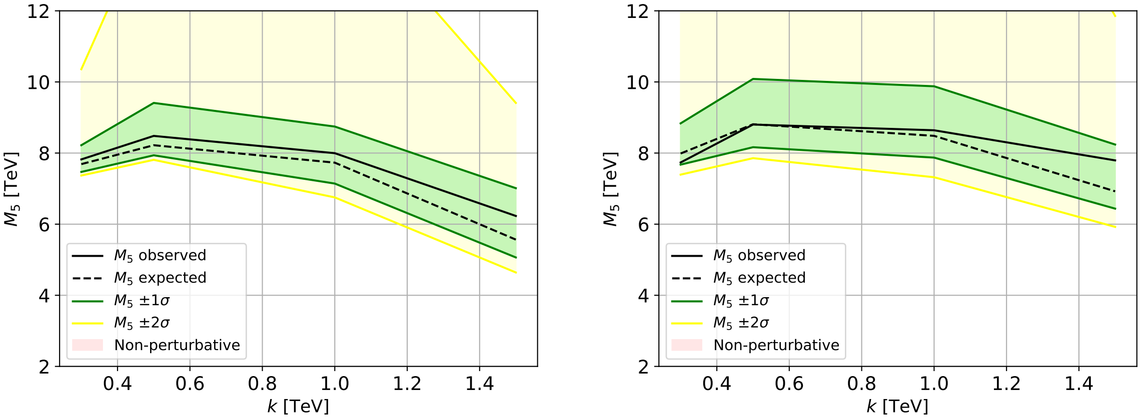

$M_5 = 1.0$ TeV $M_5 = 2.0$ TeV

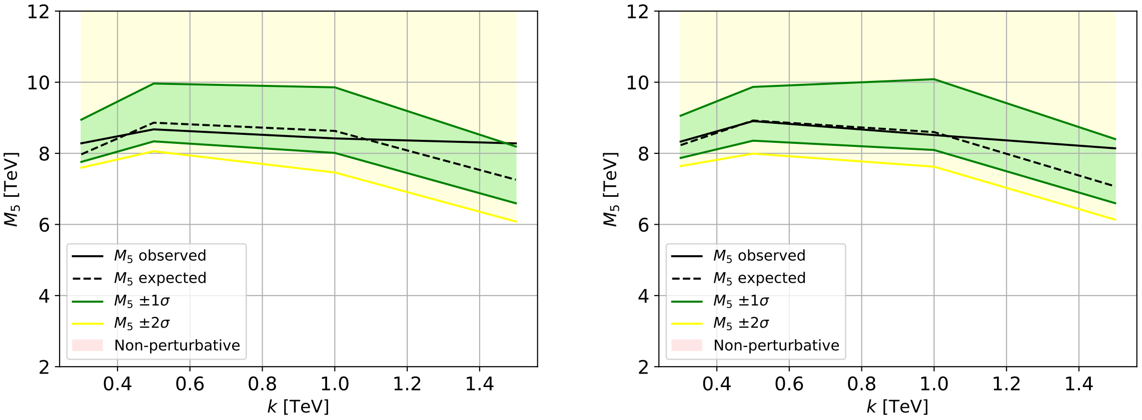

$M_5 = 3.0$ TeV $M_5 = 4.0$ TeV

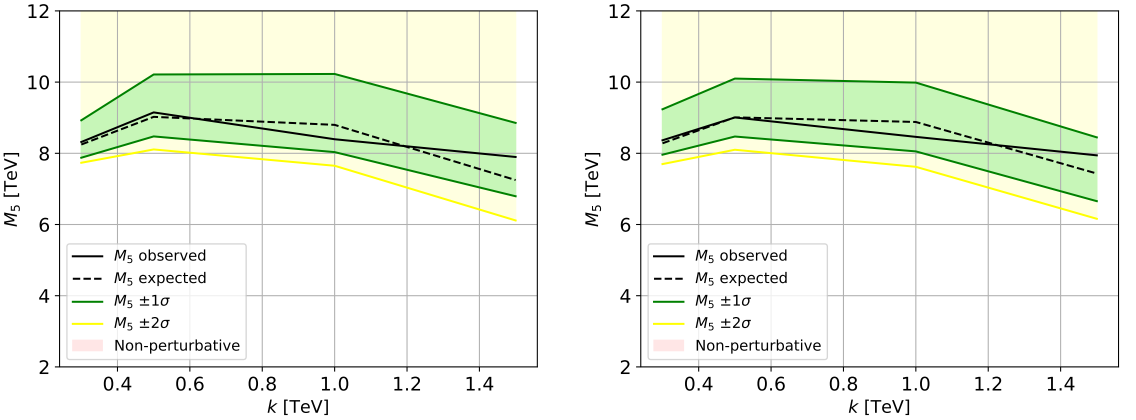

$M_5 = 5.0$ TeV $M_5 = 6.0$ TeV

Figure 9.7: The expected lower limit exclusion at 95% confidence level using model dependent FT in $\gamma\gamma$ channel. Data is plotted in black, it is consistent with the expected limit drawn from the background model.

Chapter 10

Summary

The data used in this analysis was collected between 2015 and 2018, corresponding to an integrated luminosity of 140 fb^{-1}, at $\sqrt{s} = 13$ TeV with the ATLAS detector at the LHC. Both model independent and model dependent searches were performed for graviton resonances in the e^+e^- and $\gamma\gamma$ invariant mass spectrum. An invariant mass range of [250, 4182] GeV for e^+e^-, and [150, 2360] GeV for $\gamma\gamma$ has been searched.

The model independent analysis applied a standard Fourier transform across the available invariant mass range to search for evenly spaced resonances. The model dependent analysis is specifically designed for the CW/LD model's quasi-periodic signal hypothesis, and a specialized Fourier transform is applied across the mass range to examine spacing of [3, 1732] GeV for e^+e^- channel, and [3, 974] GeV for $\gamma\gamma$ channel. In both e^+e^- and $\gamma\gamma$ invariant mass spectrums, the observed data is in good agreement with SM background predictions. For periodic signals in the e^+e^- invariant mass, the most notable enhancement appears with a period of 1 TeV, with a global p-value of 0.887, and a significance of 0.142σ. In the $\gamma\gamma$ channel, the most notable enhancement appears with a period of 0.57 TeV, with a global p-value of 0.843, and a significance of 0.198σ.

Consequently, we calculate exclusion limits on the signal strength. The results exclude values of M_5 below 8 TeV for k of [0.3, 1.5] TeV at the 95 % confidence level using the $\gamma\gamma$ channel, and exclude M_5 below 6 TeV to 3 TeV from k of [1.5, 3.0] TeV at 95 % confidence level using the e^+e^- channel.

Previous searches have been performed by CMS and ATLAS collaborations [16, 17]. The CMS search was limited to only the $\gamma\gamma$ graviton decay, treated as a continuous invariant mass distribution. The ATLAS search used a neural network approach while we used a discrete Fourier transform approach. We conducted a comprehensive study of the cascade decay effect, which is not considered in either the CMS and ATLAS searches.

Bibliography

[1] W. N. Cottingham and D. A. Greenwood, *An Introduction to the Standard Model of Particle Physics*, 2nd ed. Cambridge University Press, 2007.

[2] N. Arkani–Hamed, S. Dimopoulos, and G. Dvali, “The hierarchy problem and new dimensions at a millimeter,” *Physics Letters B*, vol. 429, no. 3-4, pp. 263–272, 1998.

[3] I. Antoniadis, N. Arkani-Hamed, S. Dimopoulos, and G. Dvali, “New dimensions at a millimeter to a fermi and superstrings at a TeV,” *Physics Letters B*, vol. 436, no. 3-4, pp. 257–263, 1998.

[4] G. Gabadadze, *Ictp lectures on large extra dimensions*, 2003. arXiv: hep-ph/0308112 `[hep-ph]`.

[5] L. Randall and R. Sundrum, “Large mass hierarchy from a small extra dimension,” *Physical Review Letters*, vol. 83, no. 17, pp. 3370–3373, 1999.

[6] L. Randall and R. Sundrum, “An alternative to compactification,” *Physical Review Letters*, vol. 83, no. 23, 4690–4693, Dec. 1999.

[7] ATLAS Collaboration, “Search for new high-mass phenomena in the dilepton final state using 36 fb-1 of proton-proton collision data at $\sqrt{s}$=13 TeV with the ATLAS detector,” *Journal of High Energy Physics*, vol. 2017, no. 10, 2017.

[8] Fermilab, “Search for new dielectron resonances and Randall-Sundrum gravitons at the collider detector at Fermilab,” *Physical Review Letters*, vol. 107, no. 5, p. 051 801, Jul. 2011. arXiv: 1103.4650 `[hep-ex]`.

[9] CMS Collaboration, “Search for high-mass diphoton resonances in proton-proton collisions at 13 TeV and combination with 8 TeV search,” *Physics Letters B*, vol. 767, pp. 147–170, Apr. 2017. arXiv: 1609.02507 `[hep-ex]`.

[10] CMS Collaboration, “Search for high-mass resonances in dilepton final states in proton-proton collisions at $\sqrt{s} = 13$ TeV,” *Journal of High Energy Physics*, vol. 2018, no. 6, p. 120, Jun. 2018. arXiv: 1803.06292 `[hep-ex]`.

[11] The D0 Collaboration and Abazov, V., “Search for Randall-Sundrum gravitons in the dielectron and diphoton final states with 5.4 fb^{-1} of data from $p\bar{p}$ collisions at $\sqrt{s}$=1.96 TeV,” *Physical Review Letters*, vol. 104, no. 24, p. 241 802, Jun. 2010. arXiv: 1004.1826 `[hep-ex]`.

[12] G. F. Giudice and M. McCullough, “A clockwork theory,” *Journal of High Energy Physics*, vol. 2017, no. 2, 2017.

[13] P. Cox and T. Gherghetta, “Radion dynamics and phenomenology in the linear dilaton model,” *Journal of High Energy Physics*, vol. 2012, no. 5, p. 149, May 30, 2012.

[14] M. Berkooz, M. Rozali, and N. Seiberg, “Matrix description of m-theory on T^4 and T^5,” *Physics Letters B*, vol. 408, no. 1–4, 105–110, Sep. 1997.

[15] N. Seiberg, “New theories in six dimensions and matrix description of m-theory on T^5 and T^5/Z_2,” *Physics Letters B*, vol. 408, no. 1–4, 98–104, Sep. 1997.

[16] CMS Collaboration, “Search for physics beyond the standard model in high-mass diphoton events from proton-proton collisions at $\sqrt{s} = 13$ TeV,” *Physical Review D*, vol. 98, no. 9, p. 092 001, Nov. 2018. arXiv: 1809.00327 `[hep-ex]`.

[17] ATLAS Collaboration, “Search for periodic signals in the dielectron and diphoton invariant mass spectra using 139 fb^{-1} of pp collisions at $\sqrt{s} = 13$ TeV with the ATLAS detector,” no. arXiv:2305.10894, May 2023. arXiv: 2305.10894 `[hep-ex]`.

[18] R. P. Feynman, “The behavior of hadron collisions at extreme energies,” in *Special Relativity and Quantum Theory: A Collection of Papers on the Poincaré Group*, M. E. Noz and Y. S. Kim, Eds., Dordrecht: Springer Netherlands, 1988, pp. 289–304.

[19] G. ’t Hooft, “Naturalness, chiral symmetry, and spontaneous chiral symmetry breaking,” 1979.

[20] G. F. Giudice, “Naturally speaking: The naturalness criterion and physics at the LHC,” in *Perspectives on LHC Physics*, World Scientific, 2008, pp. 155–178.

[21] R. L. Workman and Others, “Review of Particle Physics,” *PTEP*, vol. 2022, p. 083C01, 2022.

[22] G. F. Giudice, Y. Kats, M. McCullough, R. Torre, and A. Urbano, “Clockwork/linear dilaton: Structure and phenomenology,” *Journal of High Energy Physics*, vol. 2018, no. 6, 2018.

[23] O. Aharony, M. Berkooz, D. Kutasov, and N. Seiberg, “Linear Dilatons, NS5-branes and Holography,” *Journal of High Energy Physics*, vol. 1998, no. 10, pp. 004–004, Oct. 5, 1998. arXiv: hep-th/9808149.

[24] M. Baryakhtar, “Graviton Phenomenology of Linear Dilaton Geometries,” *Physical Review D*, vol. 85, no. 12, p. 125 019, Jun. 18, 2012. arXiv: 1202.6674 `[hep-ph]`.

[25] R. Brustein, *The role of the superstring dilaton in cosmology and particle physics*, May 1994. arXiv: hep-th/9405066.

[26] D Bailin and A Love, “Kaluza-klein theories,” *Reports on Progress in Physics*, vol. 50, no. 9, p. 1087, 1987.

[27] N. Arkani-Hamed, A. G. Cohen, and H. Georgi, “(De)Constructing Dimensions,” *Physical Review Letters*, vol. 86, no. 21, pp. 4757–4761, May 2001. arXiv: hep-th/0104005.

[28] J. Goldstone, A. Salam, and S. Weinberg, “Broken symmetries,” *Phys. Rev.*, 1962.

[29] D. Naegels, “An introduction to goldstone boson physics and to the coset construction,” Oct. 2021.

[30] A. Blasi and N. Maggiore, “Massive gravity and Fierz Pauli theory,” *The European Physical Journal C*, vol. 77, no. 9, p. 614, 2017.

[31] N. A. Hamed, S. Dimopoulos, and G. Dvali, “The hierarchy problem and new dimensions at a millimeter,” *Physics Letters B*, vol. 429, no. 3-4, pp. 263–272, 1998.

[32] M. Baryakhtar, “Graviton Phenomenology of Linear Dilaton Geometries,” *Physical Review D*, vol. 85, no. 12, p. 125 019, Jun. 2012. arXiv: 1202.6674 `[hep-ph]`.

[33] D. Berdine, N. Kauer, and D. Rainwater, “Breakdown of the narrow width approximation for new physics,” *Physical Review Letters*, vol. 99, no. 11, 2007.

[34] G. Das, C. Degrande, V. Hirschi, F. Maltoni, and H.-S. Shao, “NLO predictions for the production of a spin-two particle at the LHC,” *Physics Letters B*, vol. 770, pp. 507–513, 2017.

[35] CMS Collaboration, “Measurements of differential Z boson production cross sections in proton-proton collisions at $\sqrt{s} = 13$ TeV,” *Journal of High Energy Physics*, vol. 2019, no. 12, 2019.

[36] ATLAS Collaboration, “Standard Model Summary Plots February 2022,” 2022.

[37] S. Y. Choi and J. H. Jeong, “Selection rules for the decay of a particle into two identical massless particles of any spin,” *Physical Review D*, vol. 103, no. 9, p. 096 013, May 2021.

[38] L. Evans and P. Bryant, “LHC machine,” *Journal of Instrumentation*, vol. 3, no. 08, S08001–S08001, 2008.

[39] ATLAS Collaboration, *Luminosity determination in pp collisions at $\sqrt{s} = 13$ TeV using the ATLAS detector at the LHC*. Geneva, 2019.

[40] O. Brüning, H. Burkhardt, and S. Myers, “The large hadron collider,” *Progress in Particle and Nuclear Physics*, vol. 67, no. 3, pp. 705–734, 2012.

[41] ATLAS Collaboration, *ATLAS detector and physics performance: Technical Design Report, 1* (Technical design report. ATLAS). Geneva: CERN, 1999.

[42] ATLAS Collaboration, “The ATLAS experiment at the CERN large hadron collider,” *Journal of Instrumentation*, vol. 3, no. 08, S08003–S08003, 2008.

[43] ATLAS Collaboration, “Electron reconstruction and identification in the ATLAS experiment using the 2015 and 2016 LHC proton-proton collision data at $\sqrt{s} = 13$ TeV,” Aug. 2019.

[44] ATLAS Collaboration, “The ATLAS Experiment at the CERN Large Hadron Collider,” en, *Journal of Instrumentation*, vol. 3, no. 08, S08003, Aug. 2008.

[45] ATLAS Collaboration, "Search for new phenomena in high-mass diphoton final states using 37 fb^{-1} of proton-proton collisions collected at $\sqrt{s} = 13$ tev with the ATLAS detector," *Physics Letters B*, vol. 775, pp. 105–125, 2017.

[46] ATLAS Collaboration, "Measurement of the photon identification efficiencies with the ATLAS detector using LHC Run 2 data collected in 2015 and 2016," Mar. 2019, arXiv:1810.05087 [hep-ex].

[47] W Lampl *et al.*, "Calorimeter Clustering Algorithms: Description and Performance," 2008.

[48] ATLAS Collaboration, "Electron and photon performance measurements with the atlas detector using the 2015-2017 LHC proton-proton collision data," *Journal of Instrumentation*, vol. 14, no. 12, S12006–S12006, 2019.

[49] ATLAS Collaboration, "ATLAS data quality operations and performance for 2015–2018 data-taking," *Journal of Instrumentation*, vol. 15, no. 04, P04003–P04003, 2020.

[50] ATLAS Collaboration, "Measurement of higgs boson production in the diphoton decay channel at center of mass energies of 7 and 8 TeV with the ATLAS detector," *Physical Review D*, vol. 90, no. 11, 2014.

[51] T. Sjöstrand *et al.*, "An introduction to pythia 8.2," *Computer Physics Communications*, vol. 191, pp. 159–177, 2015.

[52] R. D. Ball *et al.*, "Parton distributions with QED corrections," *Nuclear Physics B*, vol. 877, no. 2, pp. 290–320, 2013.

[53] B. Cabouat and T. Sjöstrand, "Some dipole shower studies," *The European Physical Journal C*, vol. 78, no. 3, 2018.

[54] A. D. Martin, "Proton structure, Partons, QCD, DGLAP and beyond," 2008. arXiv: 0802.0161 `[hep-ph]`.

[55] T. Sjöstrand, "Jet fragmentation of multiparton configurations in a string framework," *Nuclear Physics B*, vol. 248, no. 2, pp. 469–502, 1984.

[56] B. Andersson, G. Gustafson, and B. Söderberg, "A general model for jet fragmentation," *Zeitschrift für Physik C Particles and Fields*, vol. 20, no. 4, pp. 317–329, Dec. 1, 1983.

[57] J. Bijnens, P. Eerola, M. Maul, A. Månsson, and T. Sjöstrand, "QCD signatures of narrow graviton resonances in hadron colliders," *Physics Letters B*, vol. 503, no. 3-4, pp. 341–348, 2001.

[58] J. Alwall *et al.*, "A standard format for Les Houches event files," *Computer Physics Communications*, vol. 176, no. 4, pp. 300–304, 2007.

[59] G. Bohm and G. Zech, *Introduction to Statistics and Data Analysis for Physicists*. Hamburg: DESY, 2014.

[60] D. K. Abhayasinghe *et al.*, "Search for new high-mass phenomena in the dilepton final state using the full run-2 proton-proton collision dataset at $\sqrt{s}$ =13 tev with the atlas detector," 2018.

[61] I. Nomidis *et al.*, "Supporting note: High-mass diphoton resonance search using 139 fb-1 of 13 tev pp collision data with the atlas detector," 2019.

[62] M. Zinser *et al.*, "Search for new high-mass resonances in the dilepton final state using proton-proton collisions at $\sqrt{s} = 13$ TeV with the ATLAS detector," 2016.

[63] ATLAS Collaboration, "Measurement of the isolated diphoton cross section in pp collision at $\sqrt{s} = 7$ tev with the ATLAS detector," *Physical Review D*, vol. 85, no. 1, 2012.

[64] S. Hoche, F. Krauss, M. Schonherr, and F. Siegert, "QCD matrix elements parton showers. the NLO case," *Journal of High Energy Physics*, vol. 2013, no. 4, 2013.

[65] R. D. Ball *et al.*, "Parton distributions for the LHC run II," *Journal of High Energy Physics*, vol. 2015, no. 4, 2015.

[66] ATLAS Collaboration, "The ATLAS simulation infrastructure," *The European Physical Journal C*, vol. 70, no. 3, pp. 823–874, 2010.

[67] ATLAS Collaboration, "The simulation principle and performance of the atlas fast calorimeter simulation fastcalosim," 2010.

[69] J. Neyman, E. S. Pearson, and K. Pearson, "Ix. on the problem of the most efficient tests of statistical hypotheses," *Philosophical Transactions of the Royal Society of London. Series A, Containing Papers of a Mathematical or Physical Character*, vol. 231, no. 694-706, pp. 289–337, 1933.

[70] E. Gross and O. Vitells, "Trial factors for the look elsewhere effect in high energy physics," *The European Physical Journal C*, vol. 70, no. 1-2, pp. 525–530, Nov. 2010. arXiv: 1005.1891 `[hep-ex, physics:physics]`.

[71] Z. Sidak, "Rectangular confidence regions for the means of multivariate normal distributions," *Journal of the American Statistical Association*, vol. 62, no. 318, pp. 626–633, 1967.

[72] J. Neyman, "Outline of a theory of statistical estimation based on the classical theory of probability," *Philosophical Transactions of the Royal Society A*, vol. 236, pp. 333–380, 1937.

Appendix A: Cross-sections plots

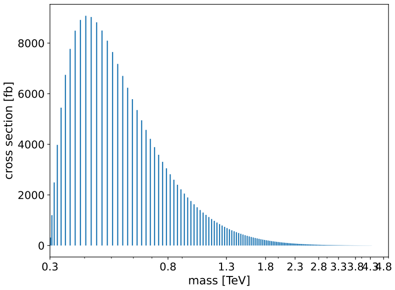

k=0.3 TeV, M_5=1.0 TeV

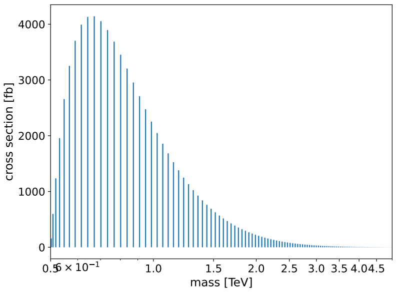

k=0.5 TeV, M_5=1.0 TeV

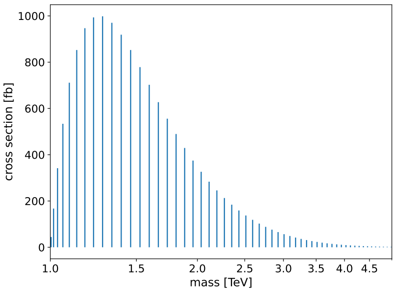

k=1.0 TeV, M_5=1.0 TeV

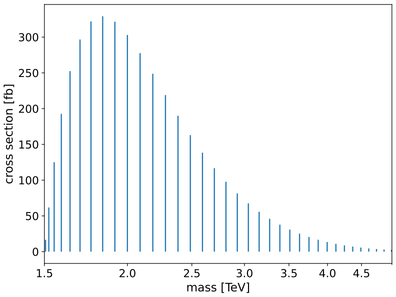

k=1.5 TeV, M_5=1.0 TeV

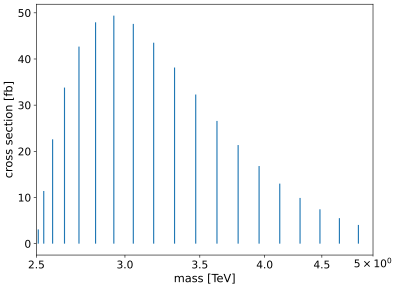

k=2.5 TeV, M_5=1.0 TeV

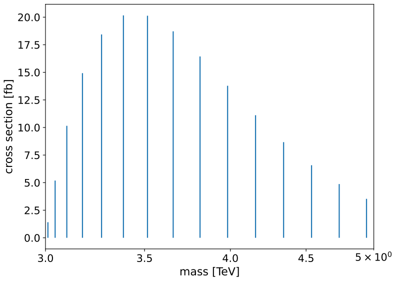

k=3.0 TeV, M_5=1.0 TeV

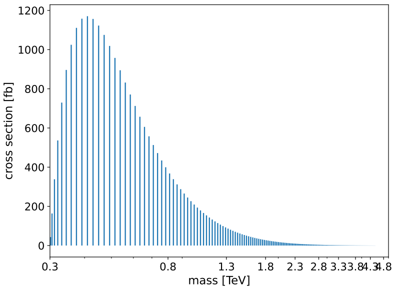

k=0.3 TeV, M_5=2.0 TeV

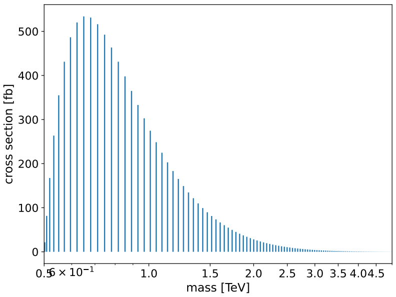

k=0.5 TeV, M_5=2.0 TeV

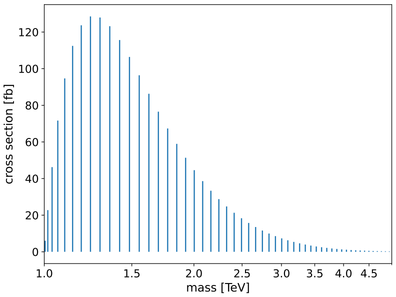

k=1.0 TeV, M_5=2.0 TeV

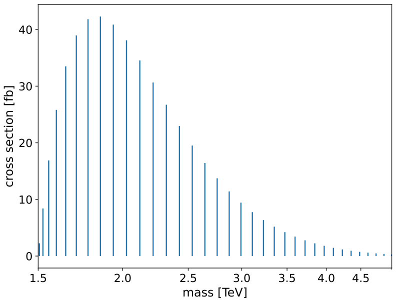

k=1.5 TeV, M_5=2.0 TeV

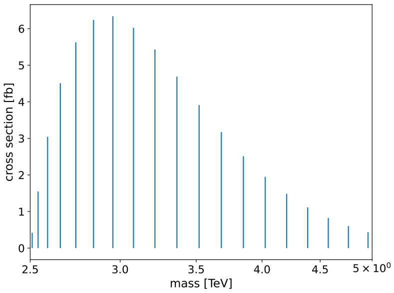

k=2.5 TeV, M_5=2.0 TeV

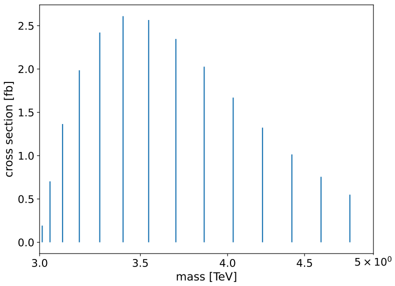

k=3.0 TeV, M_5=2.0 TeV

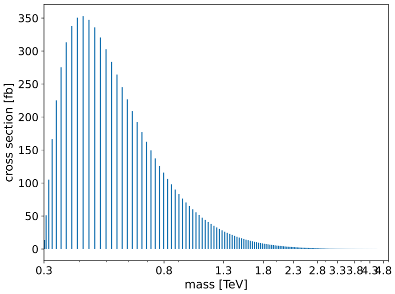

k=0.3 TeV, M_5=3.0 TeV

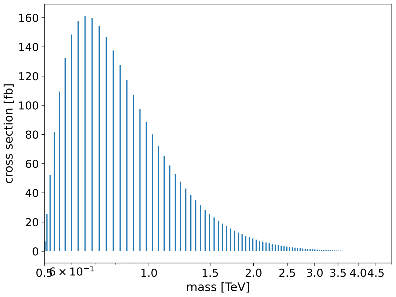

k=0.5 TeV, M_5=3.0 TeV

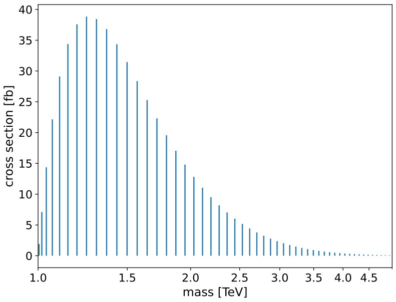

k=1.0 TeV, M_5=3.0 TeV

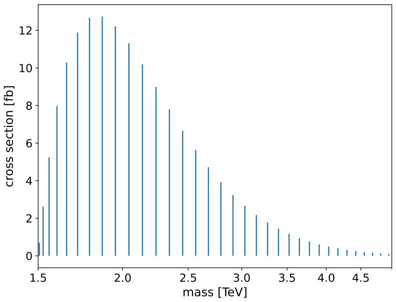

k=1.5 TeV, M_5=3.0 TeV

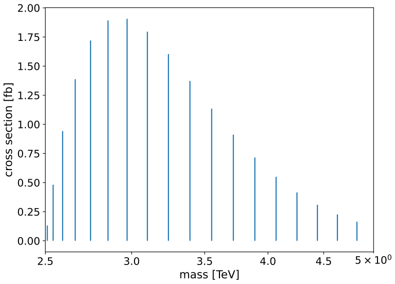

k=2.5 TeV, M_5=3.0 TeV

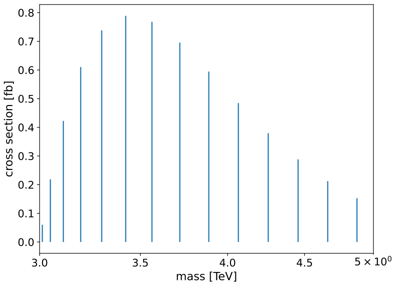

k=3.0 TeV, M_5=3.0 TeV

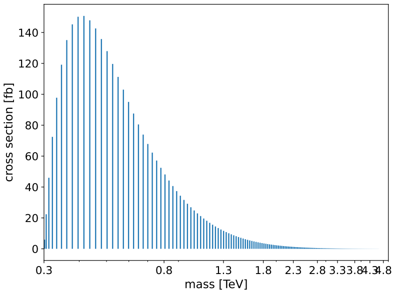

k=0.3 TeV, M_5=4.0 TeV

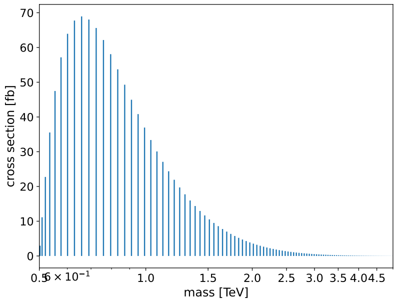

k=0.5 TeV, M_5=4.0 TeV

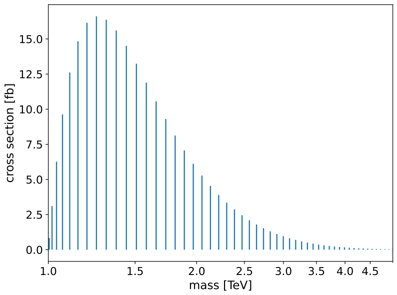

k=1.0 TeV, M_5=4.0 TeV

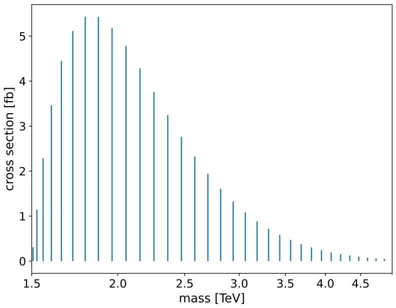

k=1.5 TeV, M_5=4.0 TeV

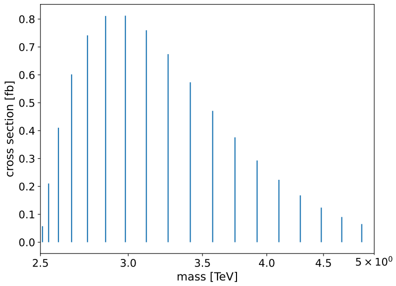

k=2.5 TeV, M_5=4.0 TeV

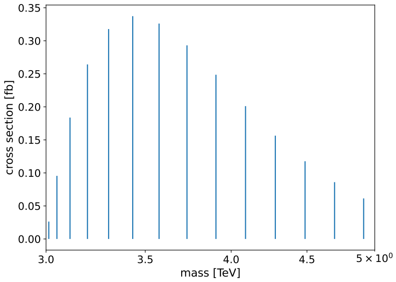

k=3.0 TeV, M_5=4.0 TeV

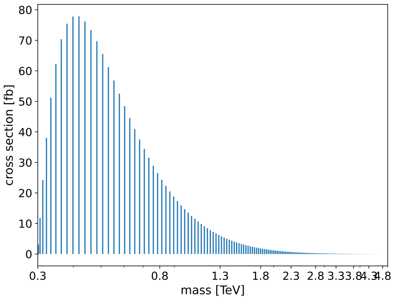

k=0.3 TeV, M_5=5.0 TeV

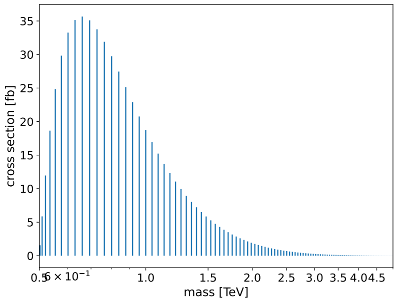

k=0.5 TeV, M_5=5.0 TeV

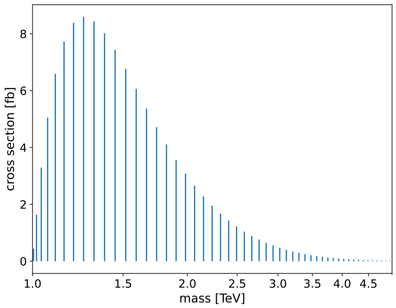

k=1.0 TeV, M_5=5.0 TeV

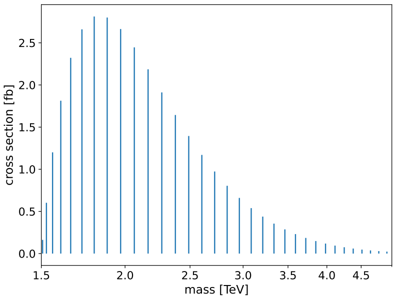

k=1.5 TeV, M_5=5.0 TeV

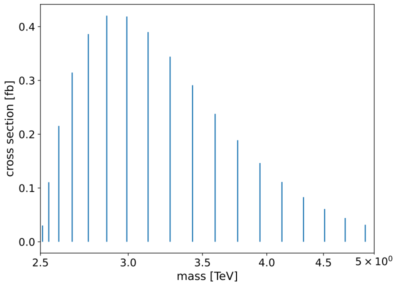

k=2.5 TeV, M_5=5.0 TeV

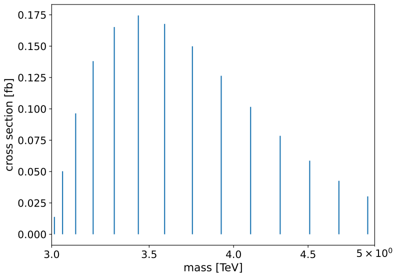

k=3.0 TeV, M_5=5.0 TeV

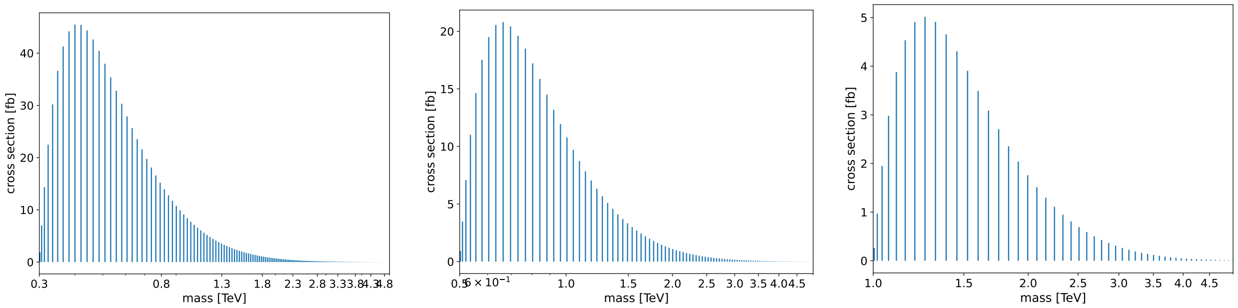

k=0.3 TeV, M_5=6.0 TeV   k=0.5 TeV, M_5=6.0 TeV   k=1.0 TeV, M_5=6.0 TeV

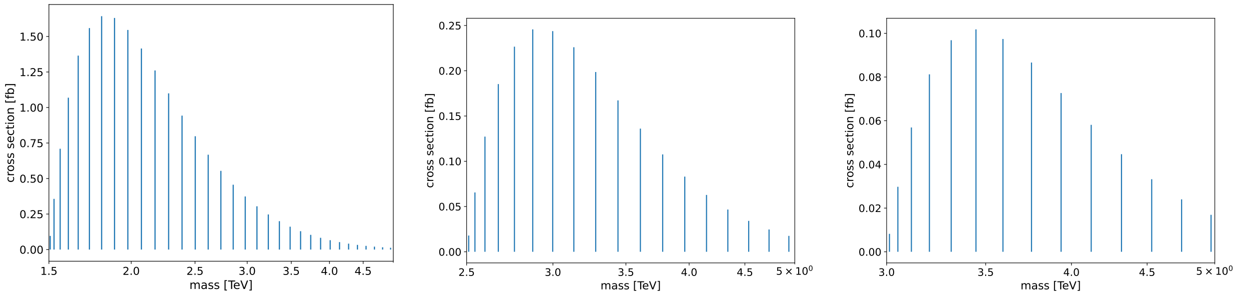

k=1.5 TeV, M_5=6.0 TeV   k=2.5 TeV, M_5=6.0 TeV   k=3.0 TeV, M_5=6.0 TeV

Fig.A: A collection of the graviton production cross-section plots. Higher M_5 mainly affect the overall magnitude; higher k results in a wider gap between resonances.

Appendix B: Decay width plots

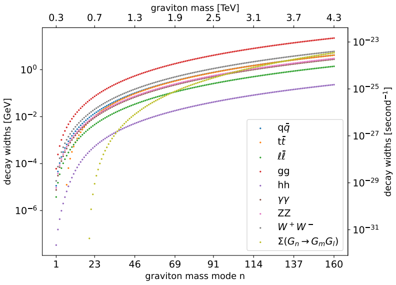

k=0.3 TeV, M_5=1.0 TeV

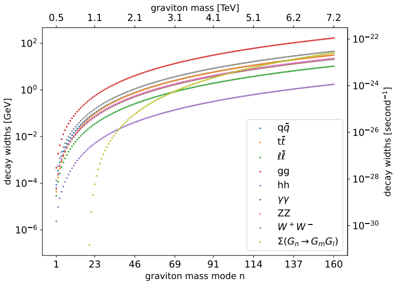

k=0.5 TeV, M_5=1.0 TeV

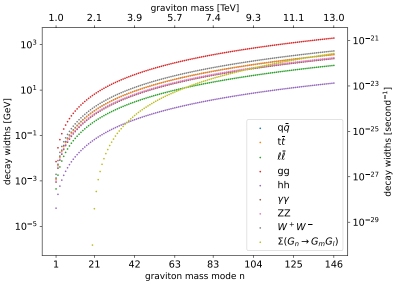

k=1.0 TeV, M_5=1.0 TeV

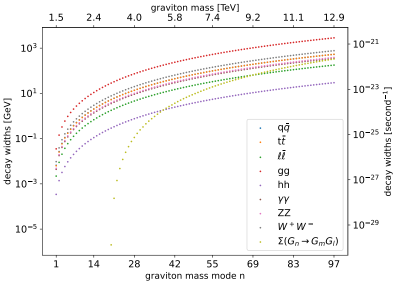

k=1.5 TeV, M_5=1.0 TeV

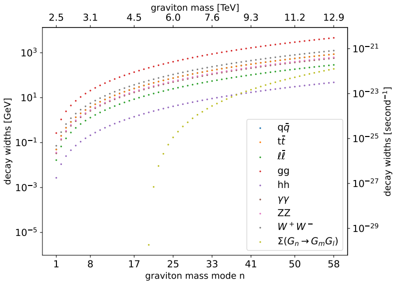

k=2.5 TeV, M_5=1.0 TeV

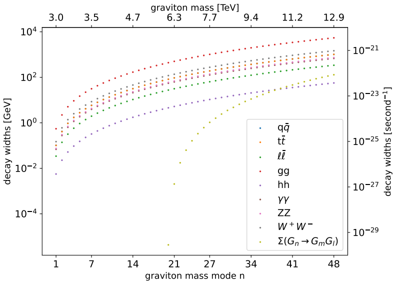

k=3.0 TeV, M_5=1.0 TeV

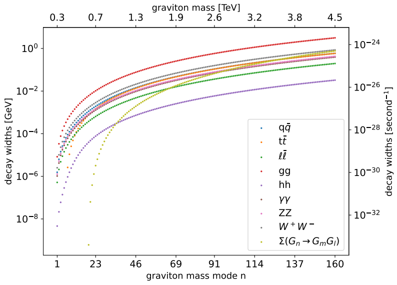

k=0.3 TeV, M_5=2.0 TeV

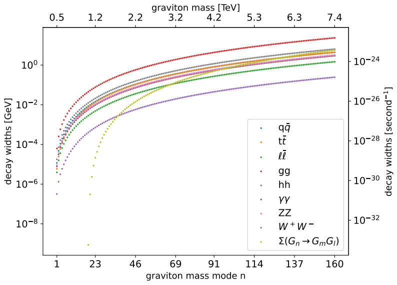

k=0.5 TeV, M_5=2.0 TeV

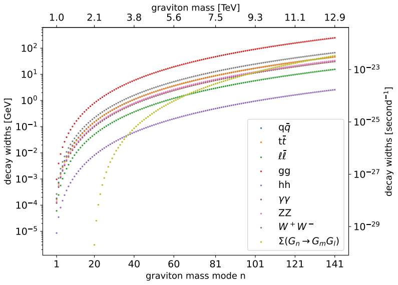

k=1.0 TeV, M_5=2.0 TeV

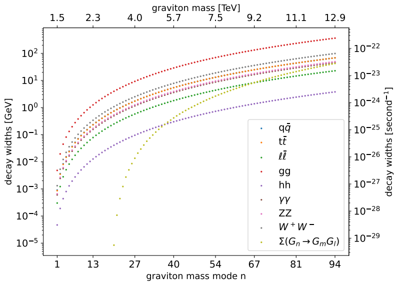

k=1.5 TeV, M_5=2.0 TeV

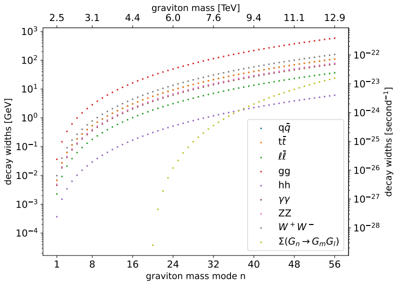

k=2.5 TeV, M_5=2.0 TeV

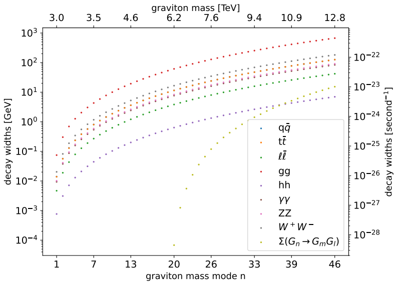

k=3.0 TeV, M_5=2.0 TeV

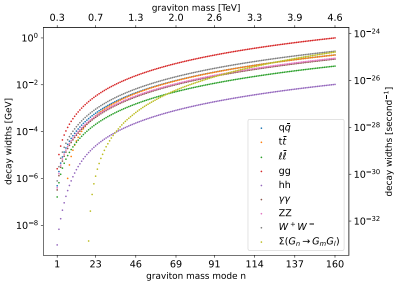

k=0.3 TeV, M_5=3.0 TeV

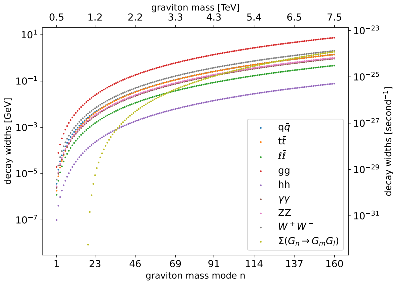

k=0.5 TeV, M_5=3.0 TeV

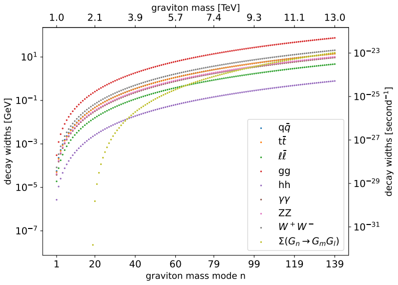

k=1.0 TeV, M_5=3.0 TeV

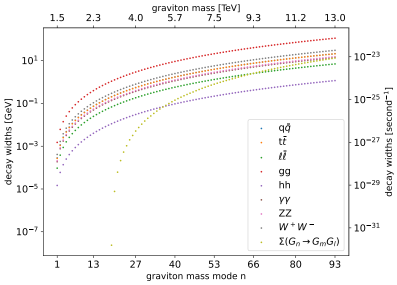

k=1.5 TeV, M_5=3.0 TeV

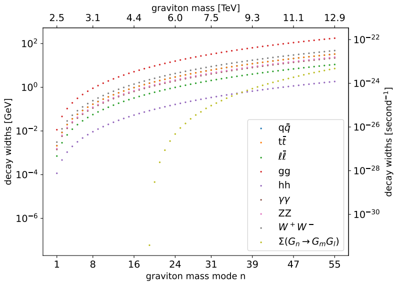

k=2.5 TeV, M_5=3.0 TeV

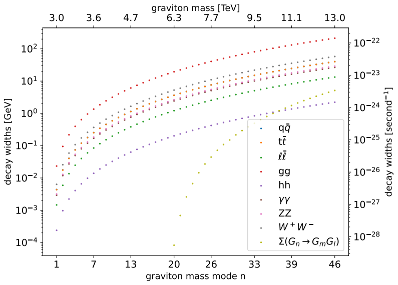

k=3.0 TeV, M_5=3.0 TeV

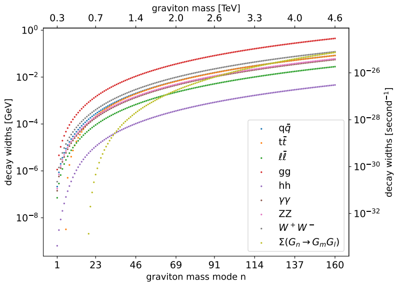

k=0.3 TeV, M_5=4.0 TeV

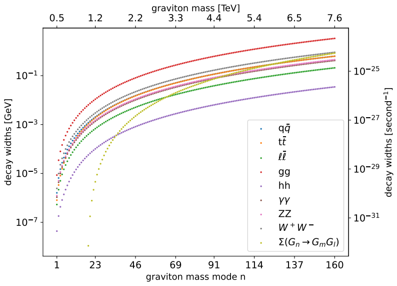

k=0.5 TeV, M_5=4.0 TeV

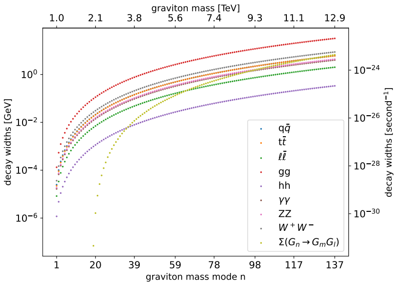

k=1.0 TeV, M_5=4.0 TeV

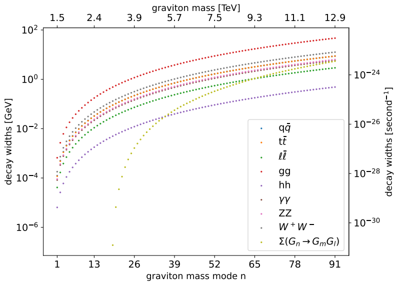

k=1.5 TeV, M_5=4.0 TeV

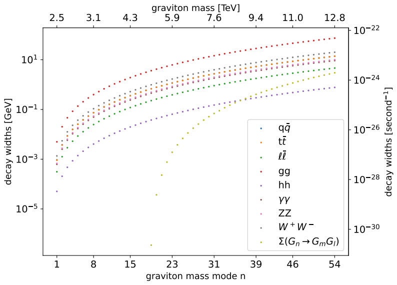

k=2.5 TeV, M_5=4.0 TeV

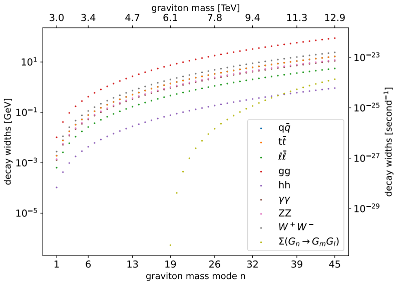

k=3.0 TeV, M_5=4.0 TeV

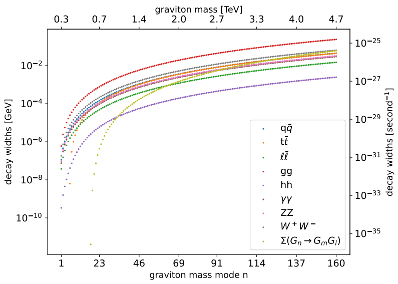

k=0.3 TeV, M_5=5.0 TeV

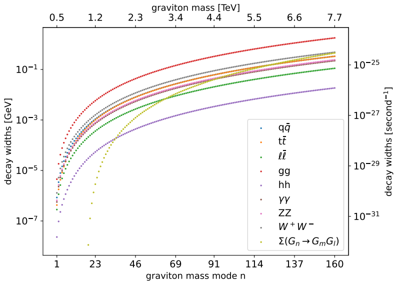

k=0.5 TeV, M_5=5.0 TeV

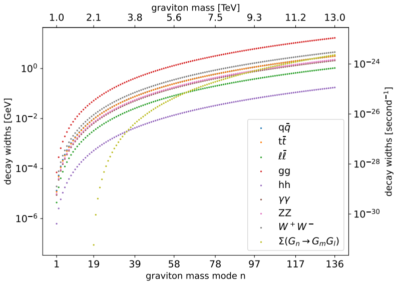

k=1.0 TeV, M_5=5.0 TeV

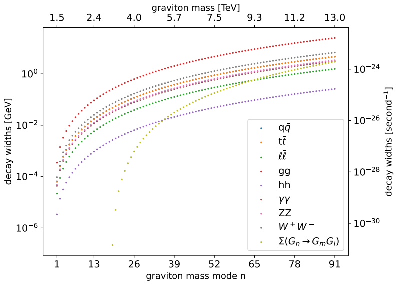

k=1.5 TeV, M_5=5.0 TeV

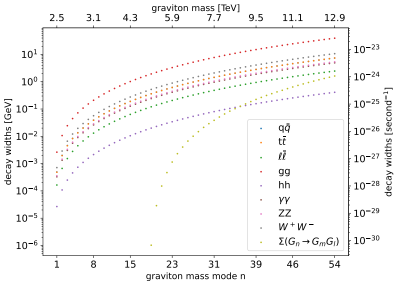

k=2.5 TeV, M_5=5.0 TeV

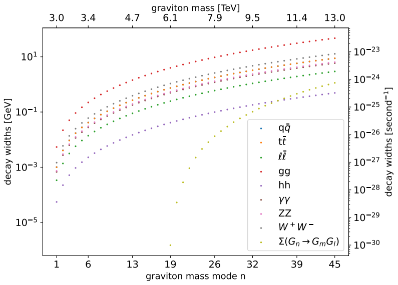

k=3.0 TeV, M_5=5.0 TeV

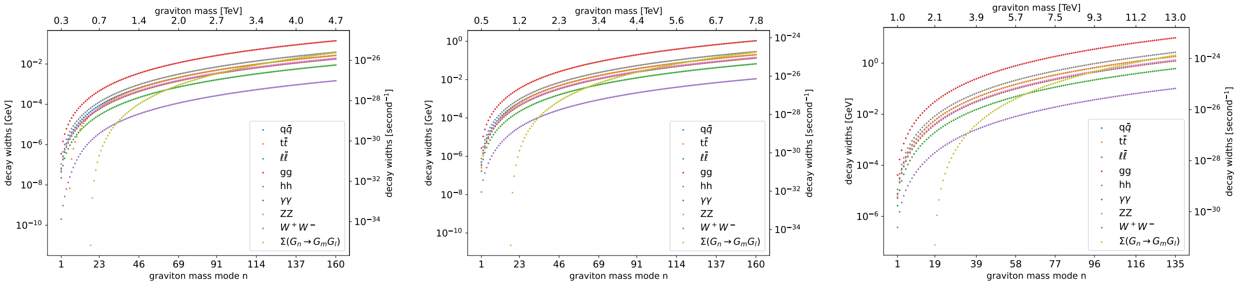

k=0.3 TeV, M_5=6.0 TeV

k=0.5 TeV, M_5=6.0 TeV

k=1.0 TeV, M_5=6.0 TeV

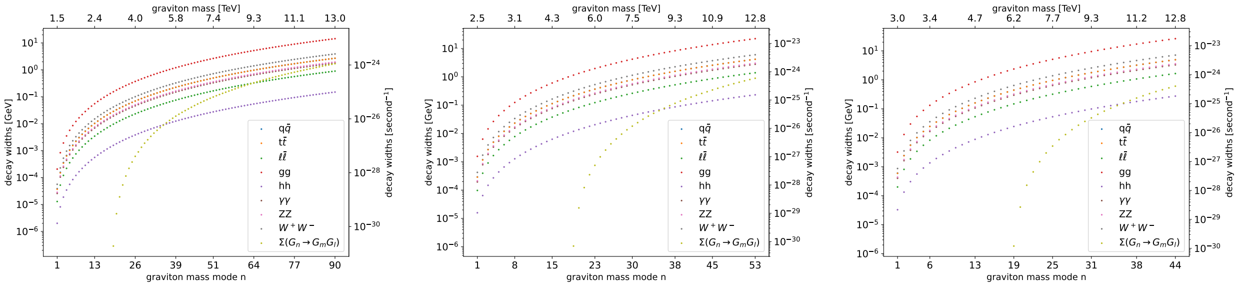

k=1.5 TeV, M_5=6.0 TeV

k=2.5 TeV, M_5=6.0 TeV

k=3.0 TeV, M_5=6.0 TeV

Fig.B : A collection of the graviton decay widths plots. Higher M_5 results in a narrower decay width; higher k results in a wider decay width.

Appendix C: Branching ratios plots

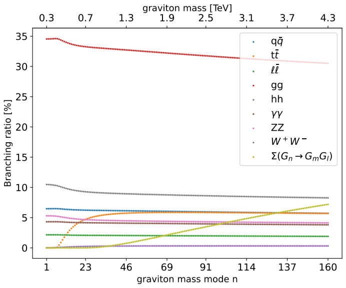

k=0.3 TeV, M_5=1.0 TeV

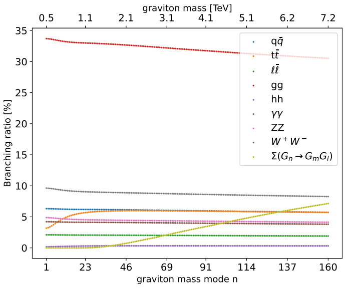

k=0.5 TeV, M_5=1.0 TeV

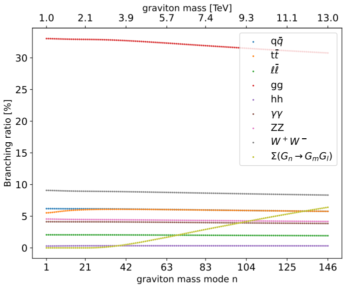

k=1.0 TeV, M_5=1.0 TeV

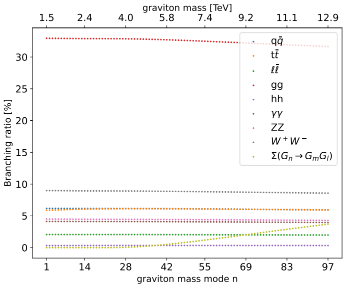

k=1.5 TeV, M_5=1.0 TeV

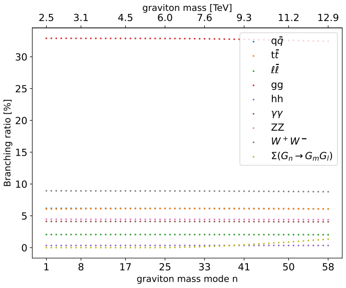

k=2.5 TeV, M_5=1.0 TeV

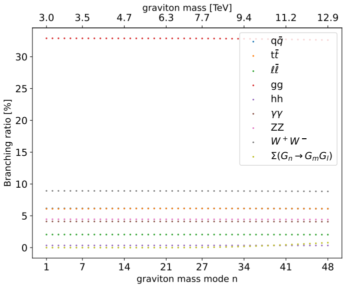

k=3.0 TeV, M_5=1.0 TeV

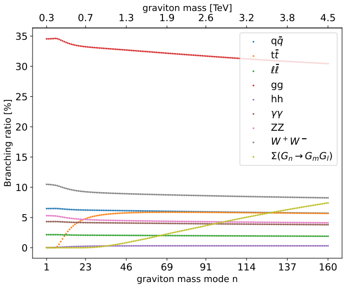

k=0.3 TeV, M_5=2.0 TeV

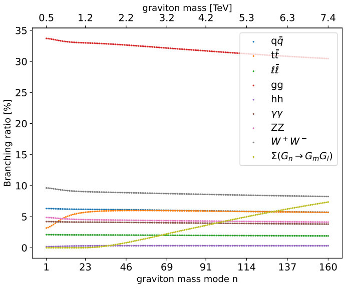

k=0.5 TeV, M_5=2.0 TeV

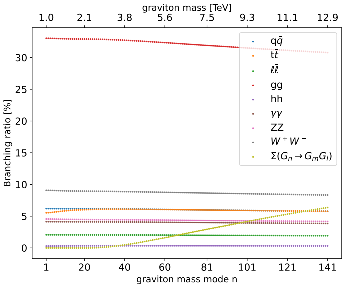

k=1.0 TeV, M_5=2.0 TeV

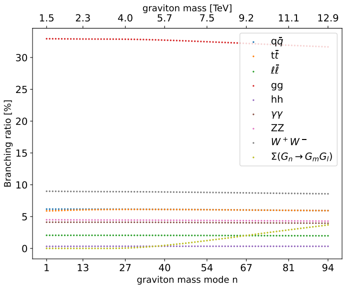

k=1.5 TeV, M_5=2.0 TeV

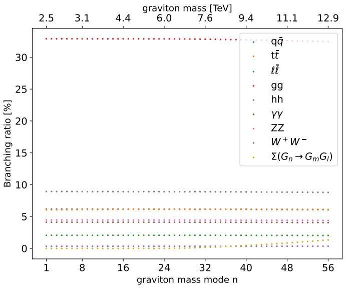

k=2.5 TeV, M_5=2.0 TeV

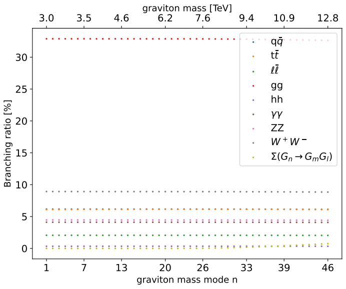

k=3.0 TeV, M_5=2.0 TeV

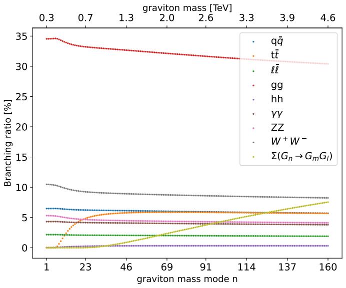

k=0.3 TeV, M_5=3.0 TeV

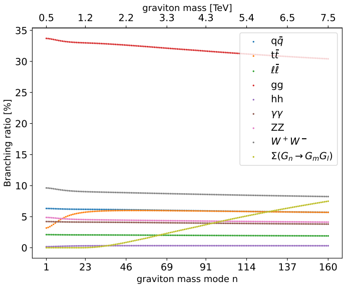

k=0.5 TeV, M_5=3.0 TeV

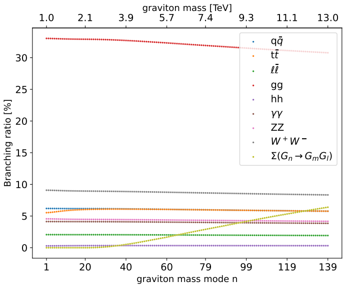

k=1.0 TeV, M_5=3.0 TeV

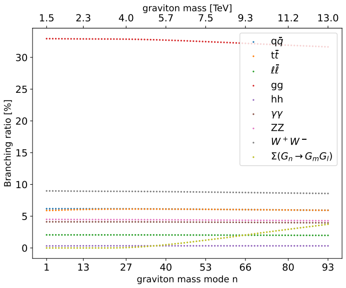

k=1.5 TeV, M_5=3.0 TeV

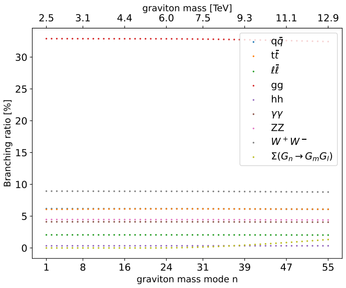

k=2.5 TeV, M_5=3.0 TeV

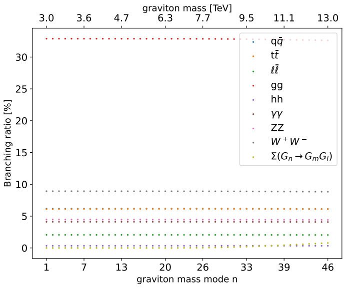

k=3.0 TeV, M_5=3.0 TeV

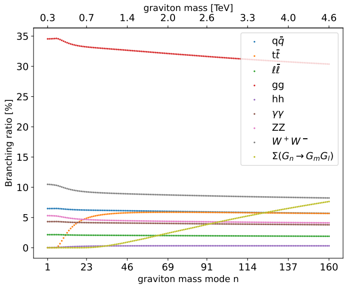

k=0.3 TeV, M_5=4.0 TeV

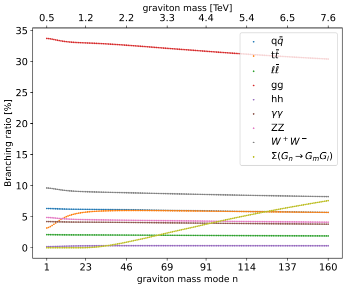

k=0.5 TeV, M_5=4.0 TeV

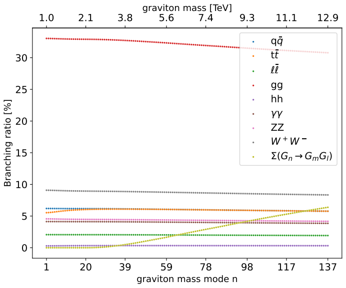

k=1.0 TeV, M_5=4.0 TeV

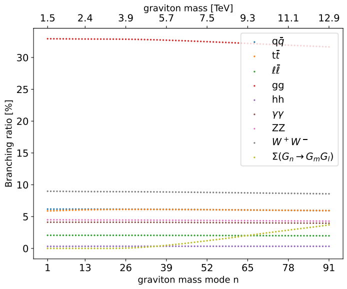

k=1.5 TeV, M_5=4.0 TeV

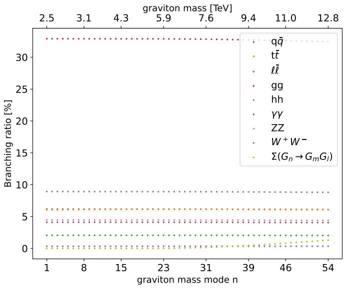

k=2.5 TeV, M_5=4.0 TeV

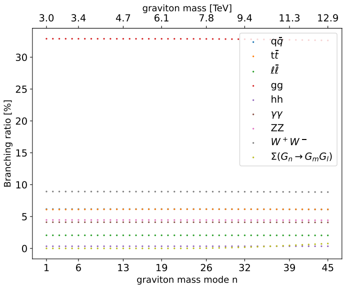

k=3.0 TeV, M_5=4.0 TeV

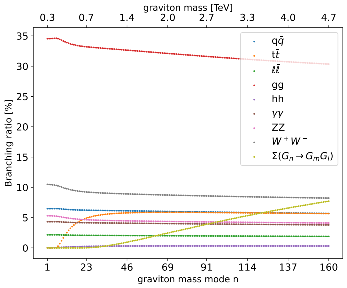

k=0.3 TeV, M_5=5.0 TeV

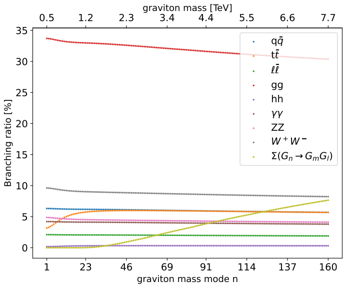

k=0.5 TeV, M_5=5.0 TeV

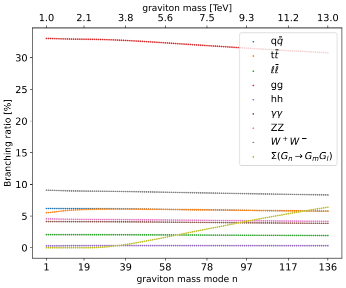

k=1.0 TeV, M_5=5.0 TeV

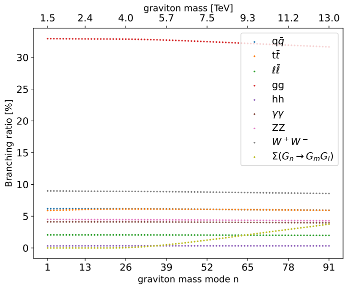

k=1.5 TeV, M_5=5.0 TeV

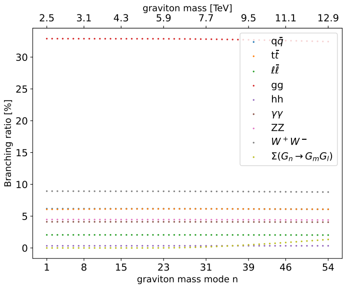

k=2.5 TeV, M_5=5.0 TeV

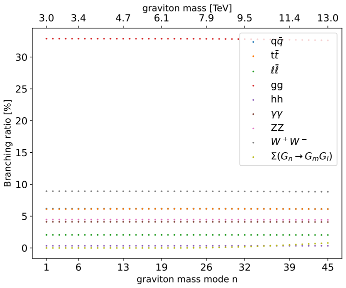

k=3.0 TeV, M_5=5.0 TeV

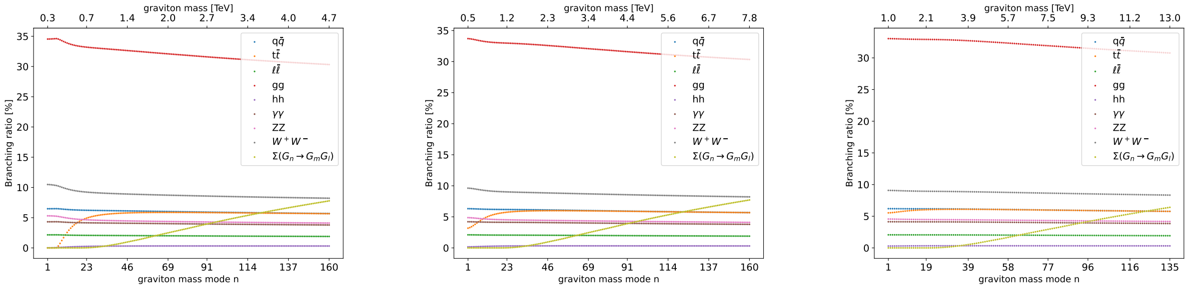

k=0.3 TeV, M_5=6.0 TeV

k=0.5 TeV, M_5=6.0 TeV

k=1.0 TeV, M_5=6.0 TeV

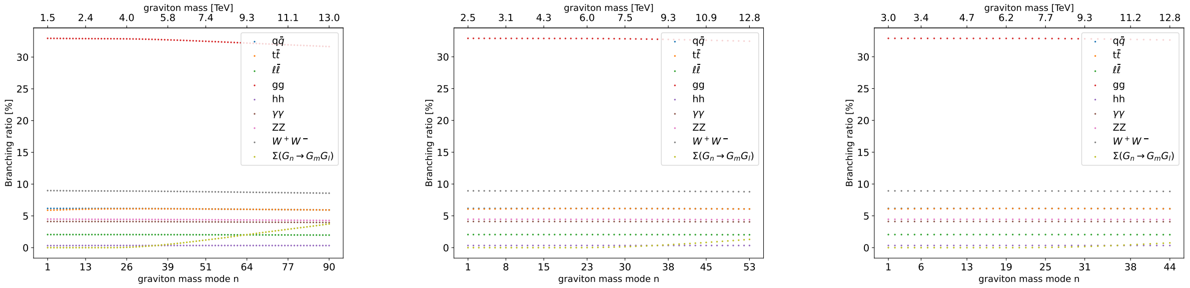

k=1.5 TeV, M_5=6.0 TeV

k=2.5 TeV, M_5=6.0 TeV

k=3.0 TeV, M_5=6.0 TeV

Fig.C: A collection of the branching ratios plots. M_5 does not affect the branching ratio. The first massive graviton at k has mass approximately k, when k is small, some graviton decay channels may be suppressed due to the kinematics.

Appendix D: Cascade decay plots

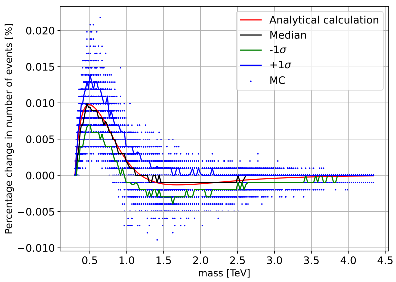

k=0.3 TeV, M_5=1.0 TeV

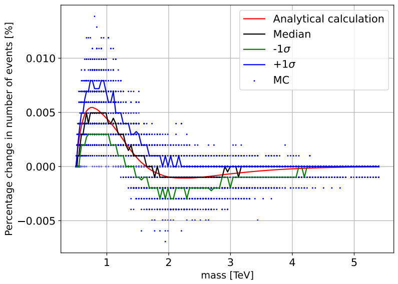

k=0.5 TeV, M_5=1.0 TeV

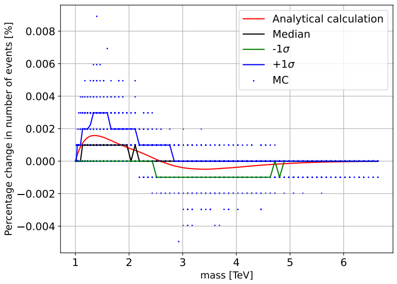

k=1.0 TeV, M_5=1.0 TeV

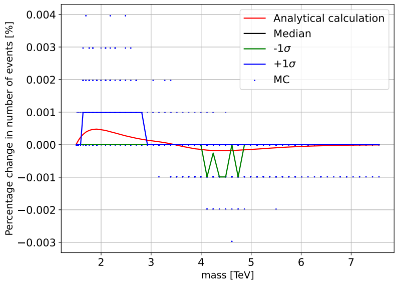

k=1.5 TeV, M_5=1.0 TeV

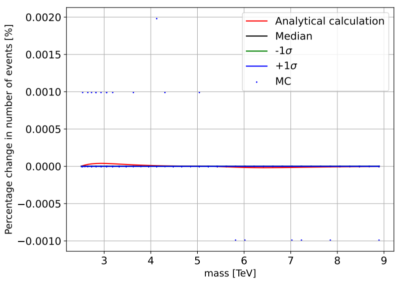

k=2.5 TeV, M_5=1.0 TeV

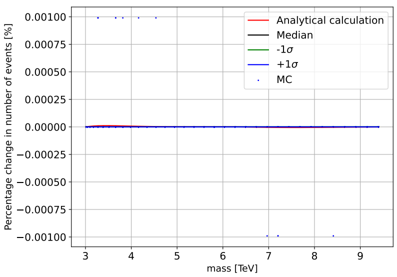

k=3.0 TeV, M_5=1.0 TeV

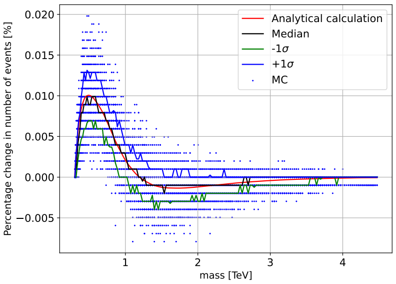

k=0.3 TeV, M_5=2.0 TeV

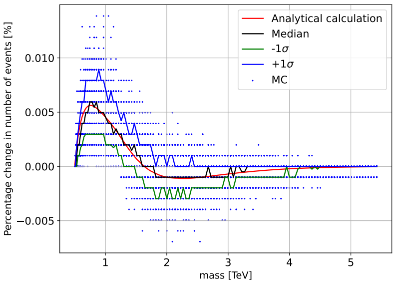

k=0.5 TeV, M_5=2.0 TeV

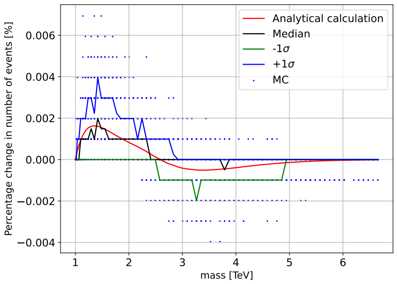

k=1.0 TeV, M_5=2.0 TeV

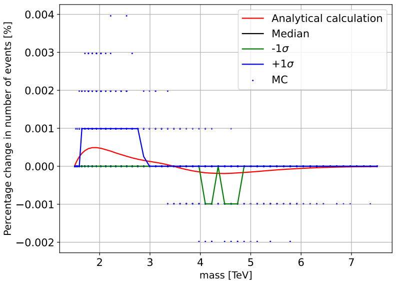

k=1.5 TeV, M_5=2.0 TeV

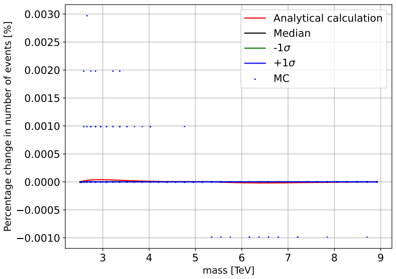

k=2.5 TeV, M_5=2.0 TeV

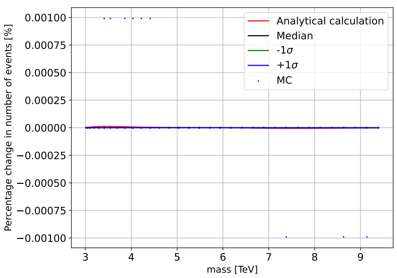

k=3.0 TeV, M_5=2.0 TeV

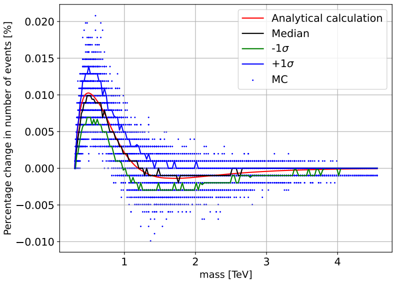

k=0.3 TeV, M_5=3.0 TeV

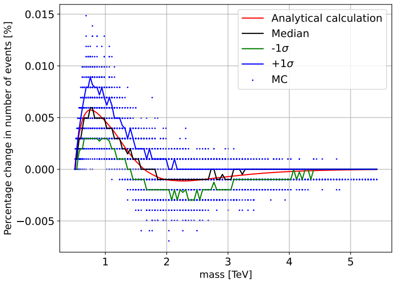

k=0.5 TeV, M_5=3.0 TeV

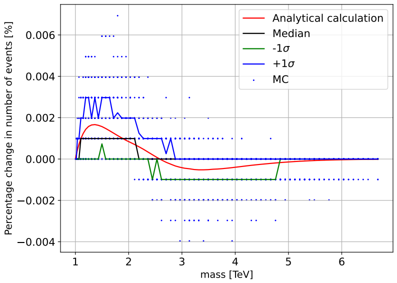

k=1.0 TeV, M_5=3.0 TeV

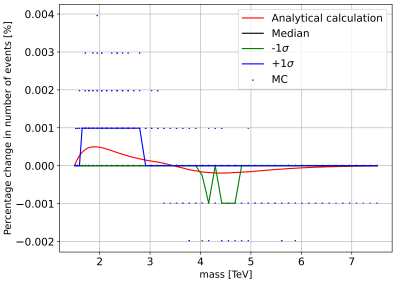

k=1.5 TeV, M_5=3.0 TeV

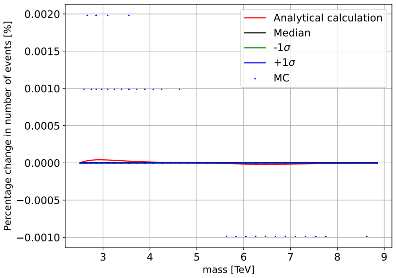

k=2.5 TeV, M_5=3.0 TeV

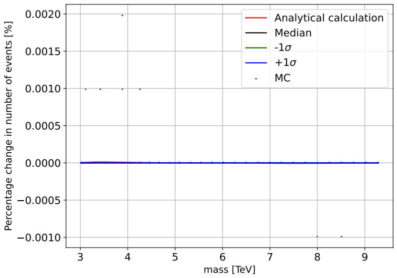

k=3.0 TeV, M_5=3.0 TeV

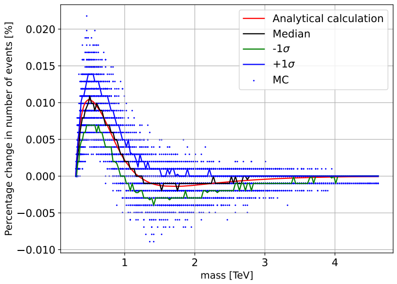

k=0.3 TeV, M_5=4.0 TeV

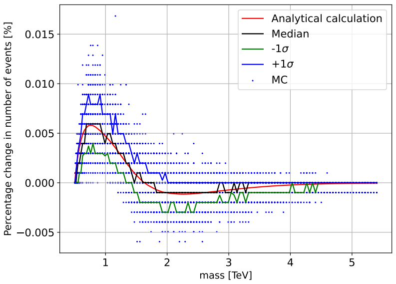

k=0.5 TeV, M_5=4.0 TeV

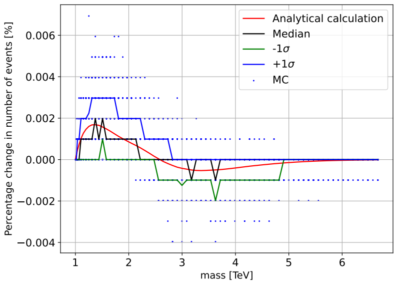

k=1.0 TeV, M_5=4.0 TeV

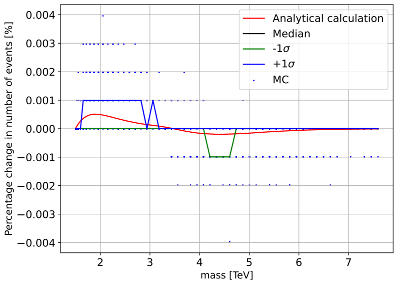

k=1.5 TeV, M_5=4.0 TeV

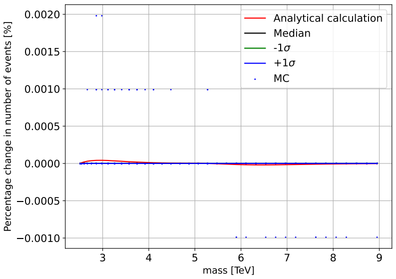

k=2.5 TeV, M_5=4.0 TeV

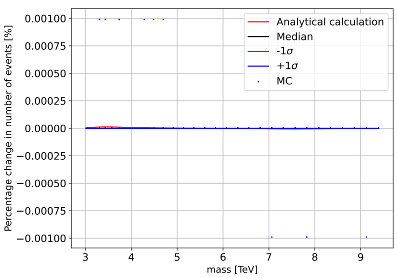

k=3.0 TeV, M_5=4.0 TeV

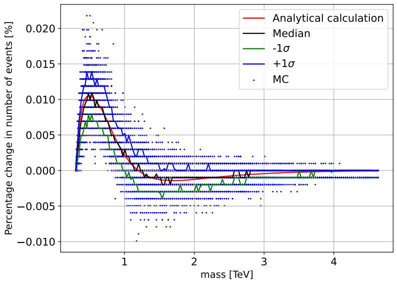

k=0.3 TeV, M_5=5.0 TeV

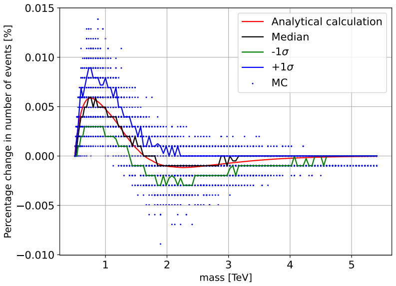

k=0.5 TeV, M_5=5.0 TeV

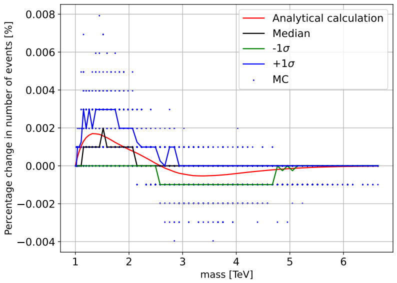

k=1.0 TeV, M_5=5.0 TeV

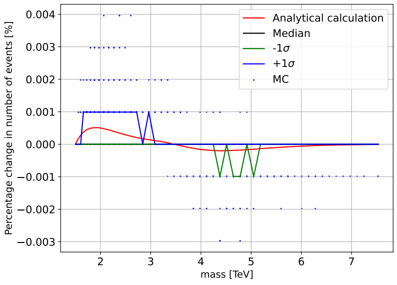

k=1.5 TeV, M_5=5.0 TeV

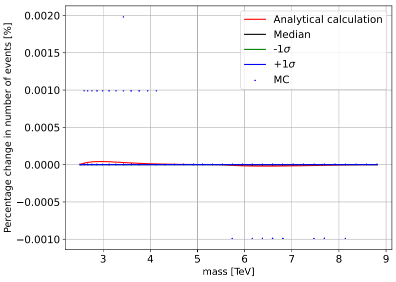

k=2.5 TeV, M_5=5.0 TeV

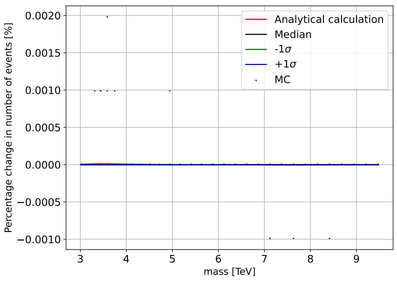

k=3.0 TeV, M_5=5.0 TeV

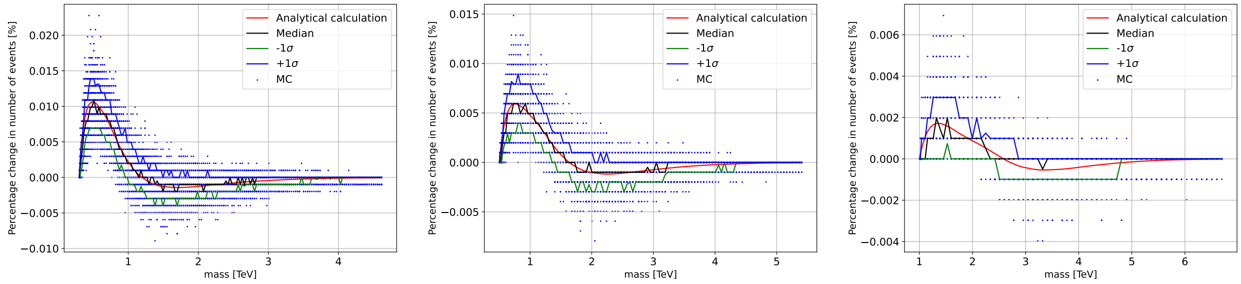

k=0.3 TeV, M_5=6.0 TeV k=0.5 TeV, M_5=6.0 TeV k=1.0 TeV, M_5=6.0 TeV

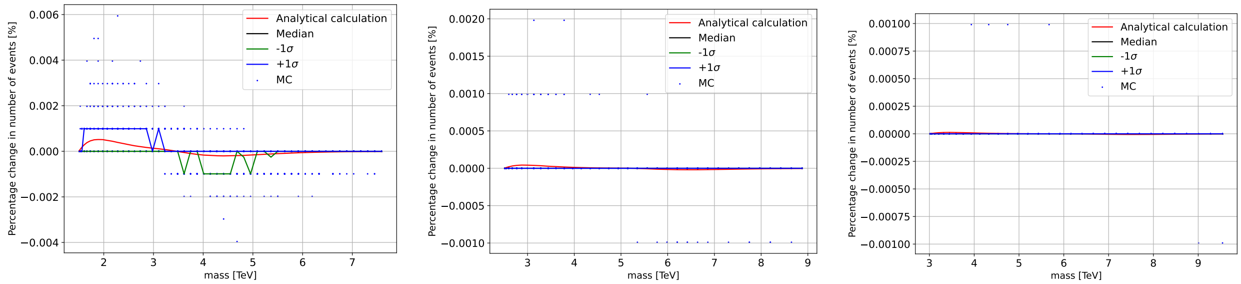

k=1.5 TeV, M_5=6.0 TeV k=2.5 TeV, M_5=6.0 TeV k=3.0 TeV, M_5=6.0 TeV

Fig.D: A collection of cascade decay effect plots. M_5 does not affect the cascade decay effect. Higher k results in a less significant cascade decay effect.

Appendix E: ee Signal-only power spectrum plots

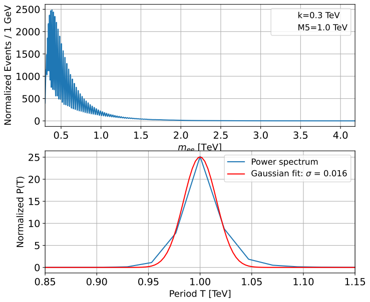

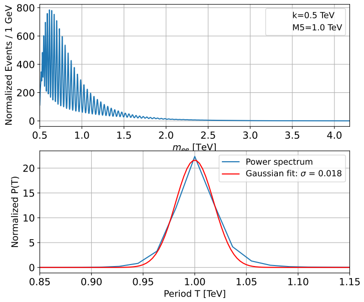

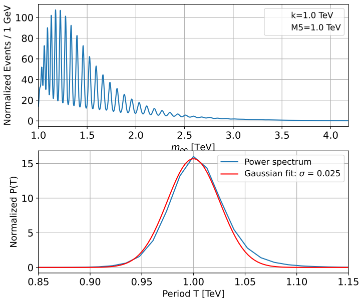

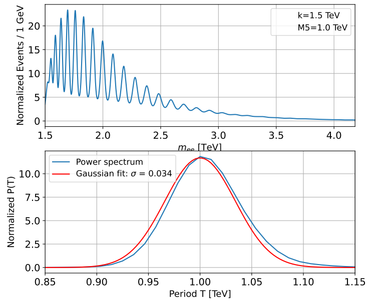

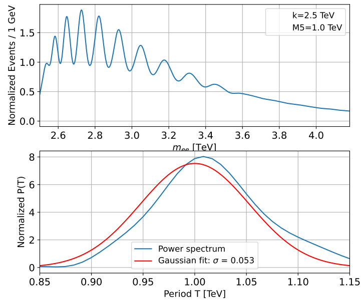

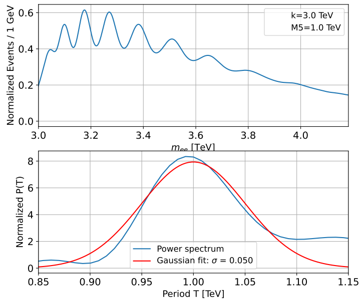

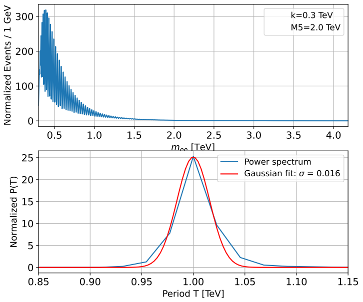
k=0.3 TeV
M5=2.0 TeV
Normalized Events / 1 GeV
m_{ee} [TeV]
Power spectrum
Gaussian fit: σ = 0.016
Normalized P(T)
Period T [TeV]

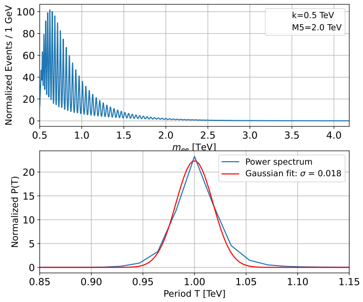
k=0.5 TeV
M5=2.0 TeV
Normalized Events / 1 GeV
m_{ee} [TeV]
Power spectrum
Gaussian fit: σ = 0.018
Normalized P(T)
Period T [TeV]

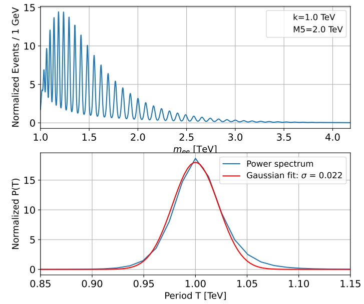
k=1.0 TeV
M5=2.0 TeV
Normalized Events / 1 GeV
m_{ee} [TeV]
Power spectrum
Gaussian fit: σ = 0.022
Normalized P(T)
Period T [TeV]

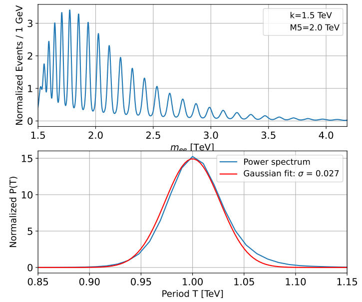
k=1.5 TeV
M5=2.0 TeV
Normalized Events / 1 GeV
m_{ee} [TeV]
Power spectrum
Gaussian fit: σ = 0.027
Normalized P(T)
Period T [TeV]

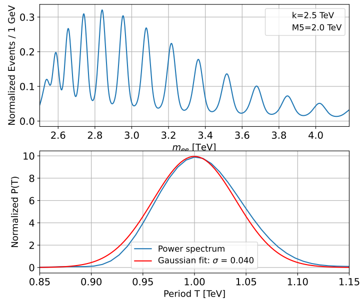
k=2.5 TeV
M5=2.0 TeV
Normalized Events / 1 GeV
m_{ee} [TeV]
Power spectrum
Gaussian fit: σ = 0.040
Normalized P(T)
Period T [TeV]

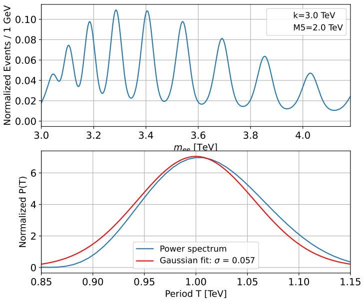
k=3.0 TeV
M5=2.0 TeV
Normalized Events / 1 GeV
m_{ee} [TeV]
Power spectrum
Gaussian fit: σ = 0.057
Normalized P(T)
Period T [TeV]

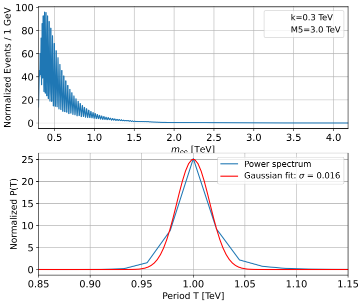
k=0.3 TeV
M5=3.0 TeV
Normalized Events / 1 GeV
m_{ee} [TeV]
Power spectrum
Gaussian fit: σ = 0.016
Normalized P(T)
Period T [TeV]

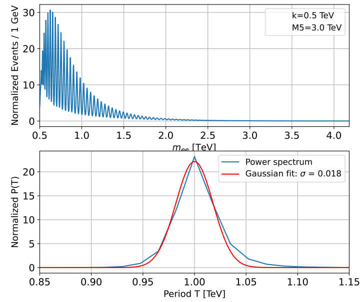
k=0.5 TeV
M5=3.0 TeV
Normalized Events / 1 GeV
m_{ee} [TeV]
Power spectrum
Gaussian fit: σ = 0.018
Normalized P(T)
Period T [TeV]

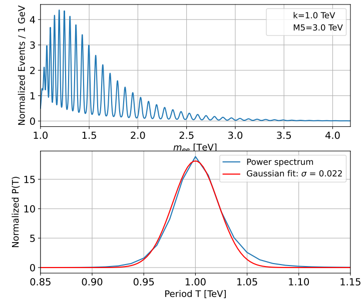
k=1.0 TeV
M5=3.0 TeV
Normalized Events / 1 GeV
m_{ee} [TeV]
Power spectrum
Gaussian fit: σ = 0.022
Normalized P(T)
Period T [TeV]

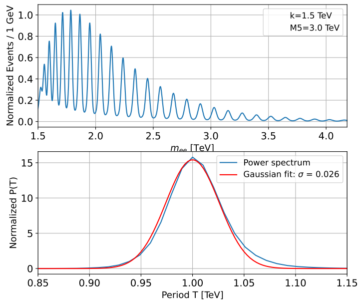
k=1.5 TeV
M5=3.0 TeV
Normalized Events / 1 GeV
m_{ee} [TeV]
Power spectrum
Gaussian fit: σ = 0.026
Normalized P(T)
Period T [TeV]

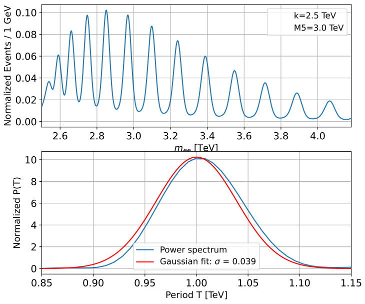
k=2.5 TeV
M5=3.0 TeV
Normalized Events / 1 GeV
m_{ee} [TeV]
Power spectrum
Gaussian fit: σ = 0.039
Normalized P(T)
Period T [TeV]

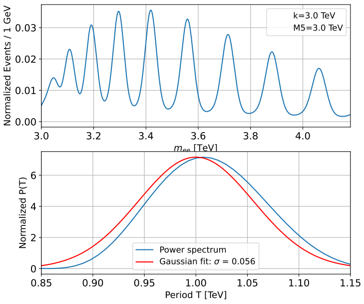
k=3.0 TeV
M5=3.0 TeV
Normalized Events / 1 GeV
m_{ee} [TeV]
Power spectrum
Gaussian fit: σ = 0.056
Normalized P(T)
Period T [TeV]

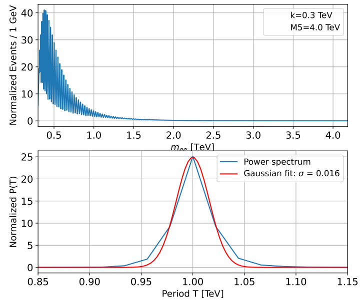
k=0.3 TeV
M5=4.0 TeV
Normalized Events / 1 GeV
m_{ee} [TeV]
Power spectrum
Gaussian fit: σ = 0.016
Normalized P(T)
Period T [TeV]

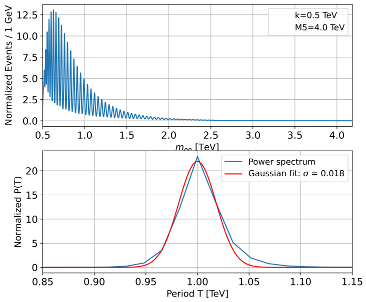
k=0.5 TeV
M5=4.0 TeV
Normalized Events / 1 GeV
m_{ee} [TeV]
Power spectrum
Gaussian fit: σ = 0.018
Normalized P(T)
Period T [TeV]

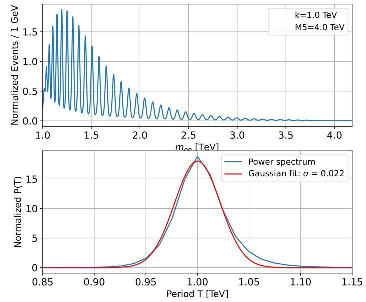
k=1.0 TeV
M5=4.0 TeV
Normalized Events / 1 GeV
m_{ee} [TeV]
Power spectrum
Gaussian fit: σ = 0.022
Normalized P(T)
Period T [TeV]

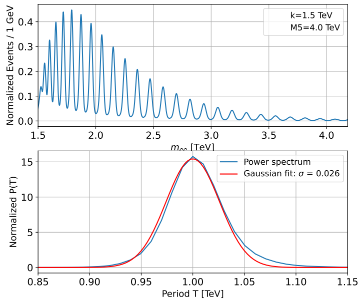
k=1.5 TeV
M5=4.0 TeV
Normalized Events / 1 GeV
m_{ee} [TeV]
Power spectrum
Gaussian fit: σ = 0.026
Normalized P(T)
Period T [TeV]

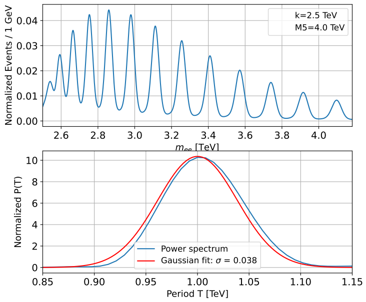
k=2.5 TeV
M5=4.0 TeV
Normalized Events / 1 GeV
m_{ee} [TeV]
Power spectrum
Gaussian fit: σ = 0.038
Normalized P(T)
Period T [TeV]

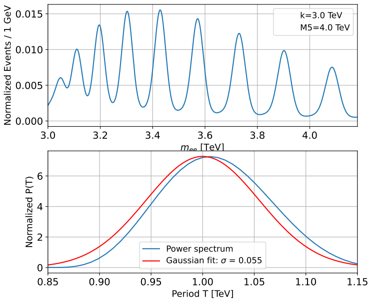
k=3.0 TeV
M5=4.0 TeV
Normalized Events / 1 GeV
m_{ee} [TeV]
Power spectrum
Gaussian fit: σ = 0.055
Normalized P(T)
Period T [TeV]

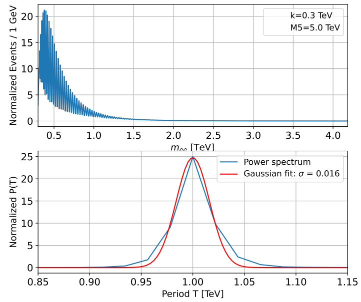
k=0.3 TeV
M5=5.0 TeV
Normalized Events / 1 GeV
m_{ee} [TeV]
Power spectrum
Gaussian fit: σ = 0.016
Normalized P(T)
Period T [TeV]

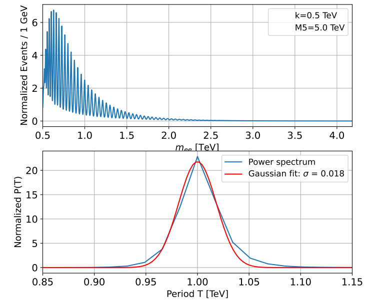
k=0.5 TeV
M5=5.0 TeV
Normalized Events / 1 GeV
m_{ee} [TeV]
Power spectrum
Gaussian fit: σ = 0.018
Normalized P(T)
Period T [TeV]

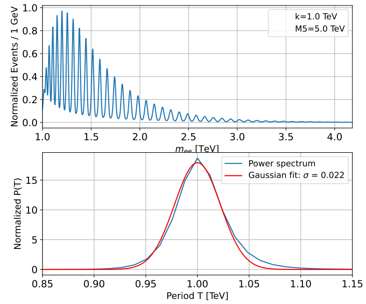
k=1.0 TeV
M5=5.0 TeV
Normalized Events / 1 GeV
m_{ee} [TeV]
Power spectrum
Gaussian fit: σ = 0.022
Normalized P(T)
Period T [TeV]

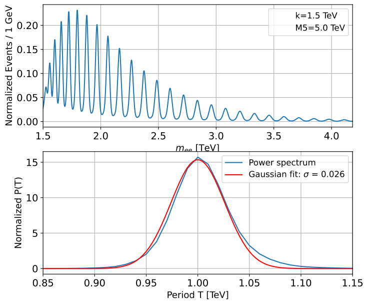
k=1.5 TeV
M5=5.0 TeV
Normalized Events / 1 GeV
m_{ee} [TeV]
Power spectrum
Gaussian fit: σ = 0.026
Normalized P(T)
Period T [TeV]

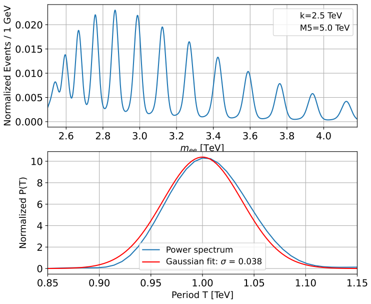
k=2.5 TeV
M5=5.0 TeV
Normalized Events / 1 GeV
m_{ee} [TeV]
Power spectrum
Gaussian fit: σ = 0.038
Normalized P(T)
Period T [TeV]

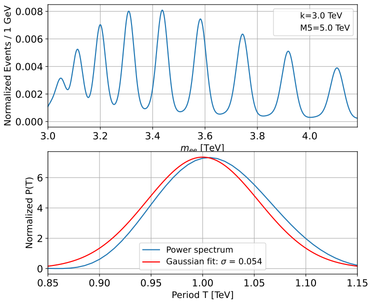
k=3.0 TeV
M5=5.0 TeV
Normalized Events / 1 GeV
m_{ee} [TeV]
Power spectrum
Gaussian fit: σ = 0.054
Normalized P(T)
Period T [TeV]

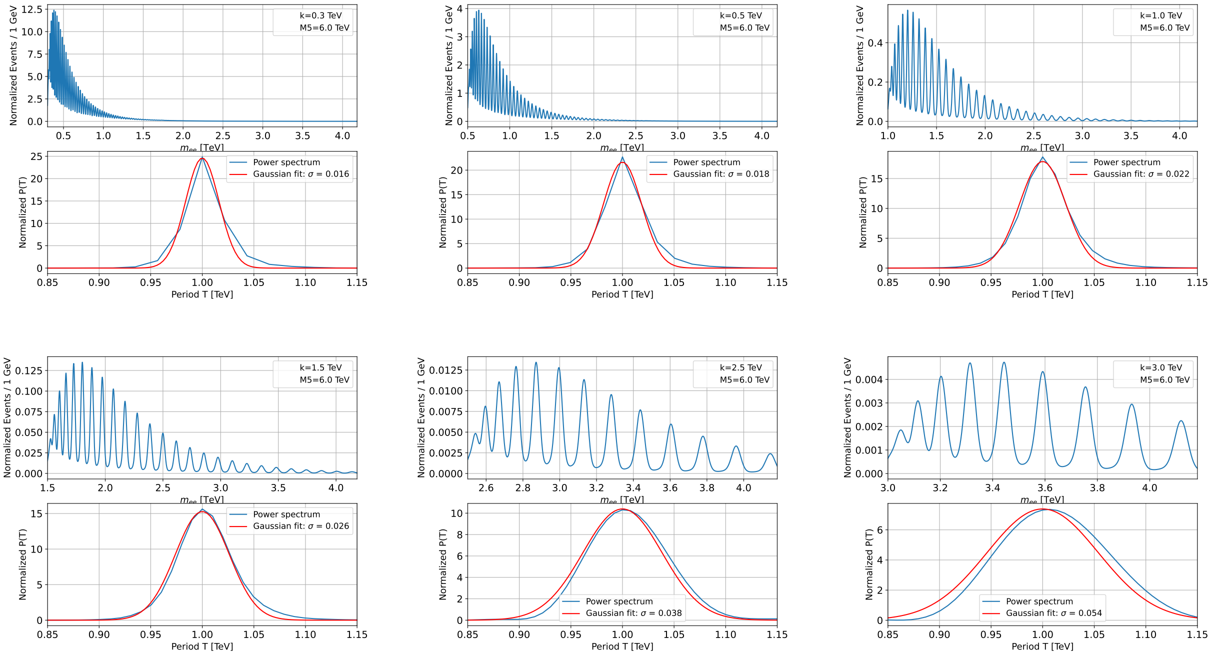

Fig.E: A collection of e^+e^- signal-only power spectrum plots. Top figures are the signal after including the detectors effect. Bottom figures are the power spectrum (blue) with CW/LD model applied. A Gaussian fit (red) is applied to the power spectrum. When k increases, the frequency of the spectrum becomes not well-defined, resulting in a wider width.

Appendix F: $\gamma\gamma$ Signal-only power spectrum plots

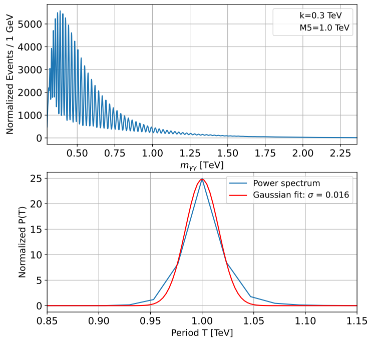

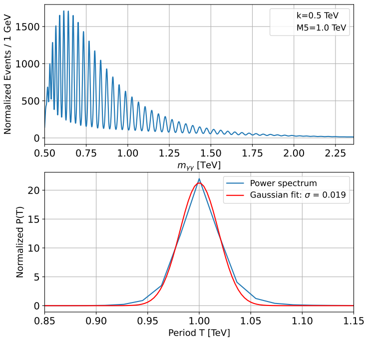

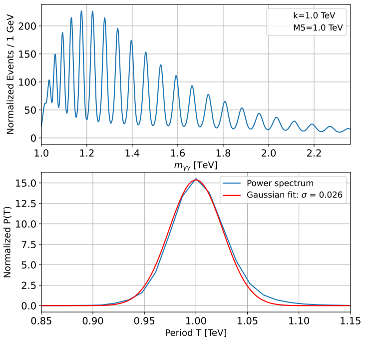

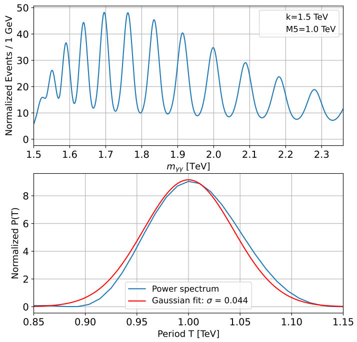

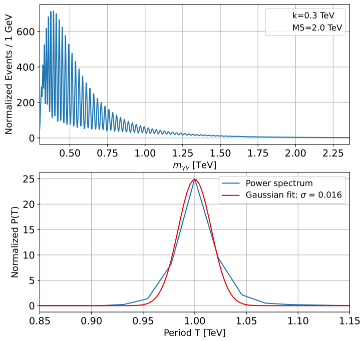

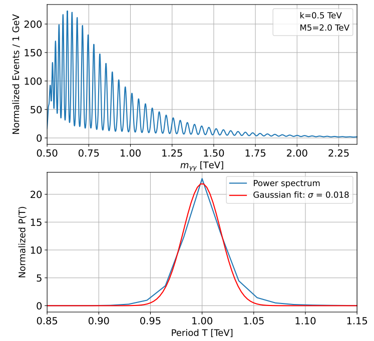

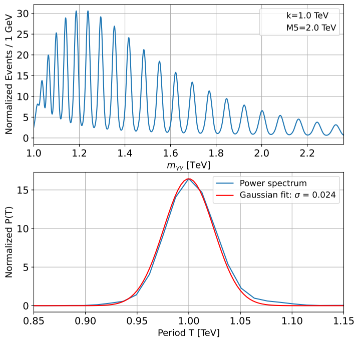

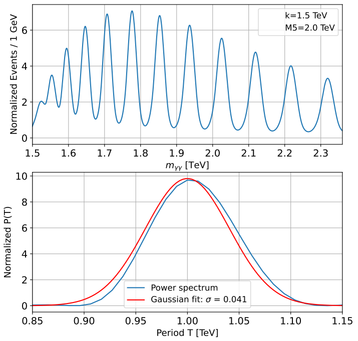

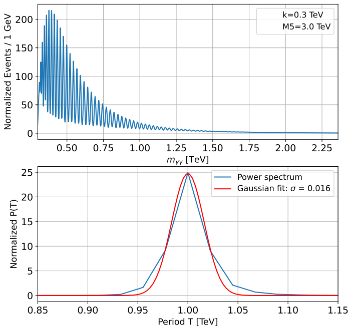
k=0.3 TeV
M5=3.0 TeV
Normalized Events / 1 GeV
$m_{\gamma\gamma}$ [TeV]
Power spectrum
Gaussian fit: σ = 0.016
Normalized P(T)
Period T [TeV]

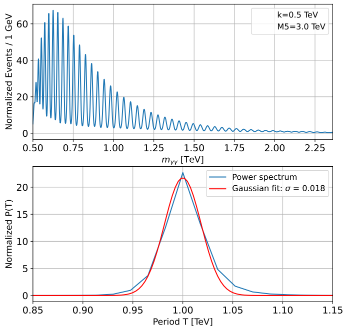
k=0.5 TeV
M5=3.0 TeV
Normalized Events / 1 GeV
$m_{\gamma\gamma}$ [TeV]
Power spectrum
Gaussian fit: σ = 0.018
Normalized P(T)
Period T [TeV]

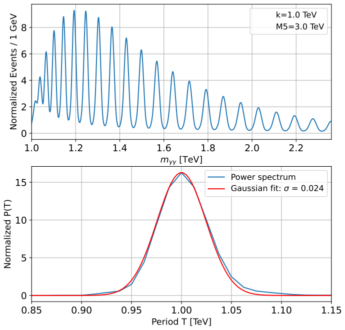
k=1.0 TeV
M5=3.0 TeV
Normalized Events / 1 GeV
$m_{\gamma\gamma}$ [TeV]
Power spectrum
Gaussian fit: σ = 0.024
Normalized P(T)
Period T [TeV]

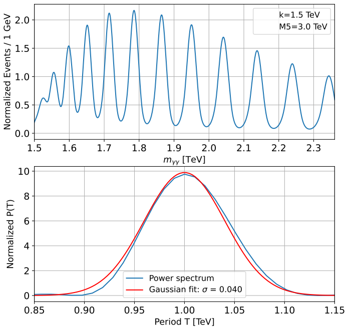
k=1.5 TeV
M5=3.0 TeV
Normalized Events / 1 GeV
$m_{\gamma\gamma}$ [TeV]
Power spectrum
Gaussian fit: σ = 0.040
Normalized P(T)
Period T [TeV]

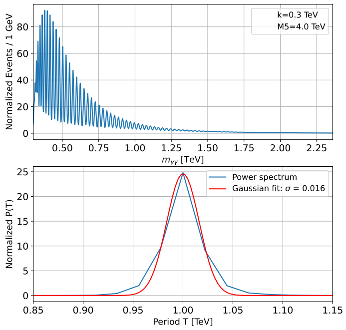
k=0.3 TeV
M5=4.0 TeV
Normalized Events / 1 GeV
$m_{\gamma\gamma}$ [TeV]
Power spectrum
Gaussian fit: σ = 0.016
Normalized P(T)
Period T [TeV]

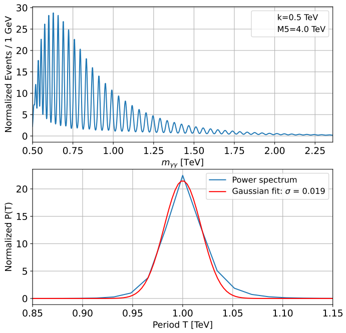
k=0.5 TeV
M5=4.0 TeV
Normalized Events / 1 GeV
$m_{\gamma\gamma}$ [TeV]
Power spectrum
Gaussian fit: σ = 0.019
Normalized P(T)
Period T [TeV]

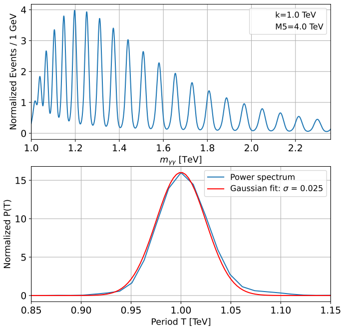
k=1.0 TeV
M5=4.0 TeV
Normalized Events / 1 GeV
$m_{\gamma\gamma}$ [TeV]
Power spectrum
Gaussian fit: σ = 0.025
Normalized P(T)
Period T [TeV]

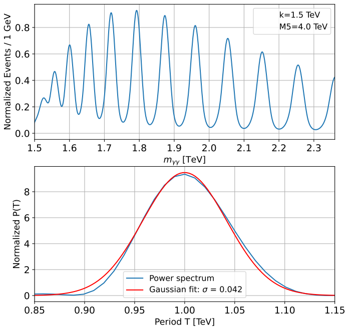
k=1.5 TeV
M5=4.0 TeV
Normalized Events / 1 GeV
$m_{\gamma\gamma}$ [TeV]
Power spectrum
Gaussian fit: σ = 0.042
Normalized P(T)
Period T [TeV]

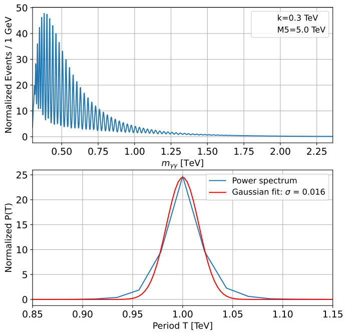
k=0.3 TeV
M5=5.0 TeV
Normalized Events / 1 GeV
$m_{\gamma\gamma}$ [TeV]
Power spectrum
Gaussian fit: σ = 0.016
Normalized P(T)
Period T [TeV]

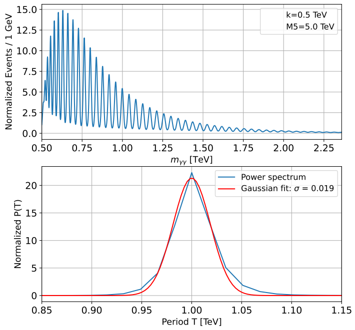
k=0.5 TeV
M5=5.0 TeV
Normalized Events / 1 GeV
$m_{\gamma\gamma}$ [TeV]
Power spectrum
Gaussian fit: σ = 0.019
Normalized P(T)
Period T [TeV]

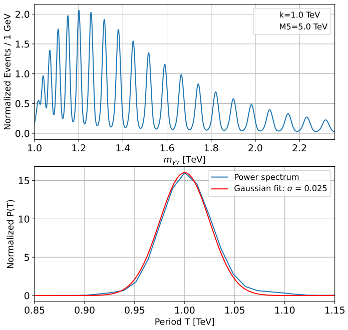
k=1.0 TeV
M5=5.0 TeV
Normalized Events / 1 GeV
$m_{\gamma\gamma}$ [TeV]
Power spectrum
Gaussian fit: σ = 0.025
Normalized P(T)
Period T [TeV]

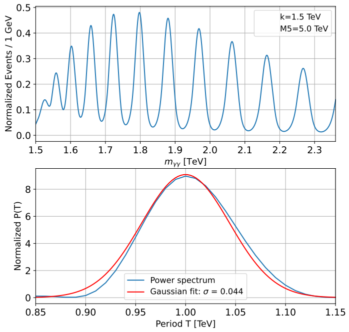
k=1.5 TeV
M5=5.0 TeV
Normalized Events / 1 GeV
$m_{\gamma\gamma}$ [TeV]
Power spectrum
Gaussian fit: σ = 0.044
Normalized P(T)
Period T [TeV]

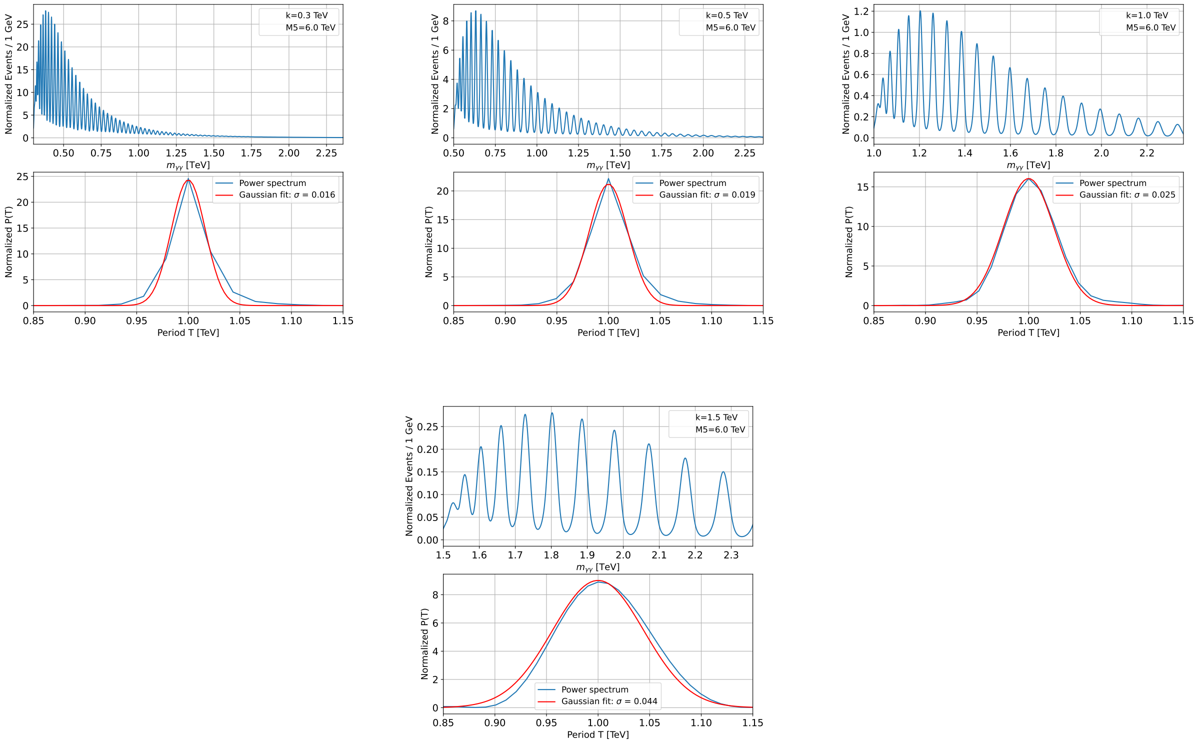

Fig.F: A collection of $\gamma\gamma$ signal-only power spectrum plots. Top figures are the signal after including the detectors effect. Bottom figures are the power spectrum (blue) with CW/LD model applied. A Gaussian fit (red) is applied to the power spectrum. When k increases, the frequency of the spectrum becomes not well-defined, resulting in a wider width.

Appendix G: e^+e^- Background statistics

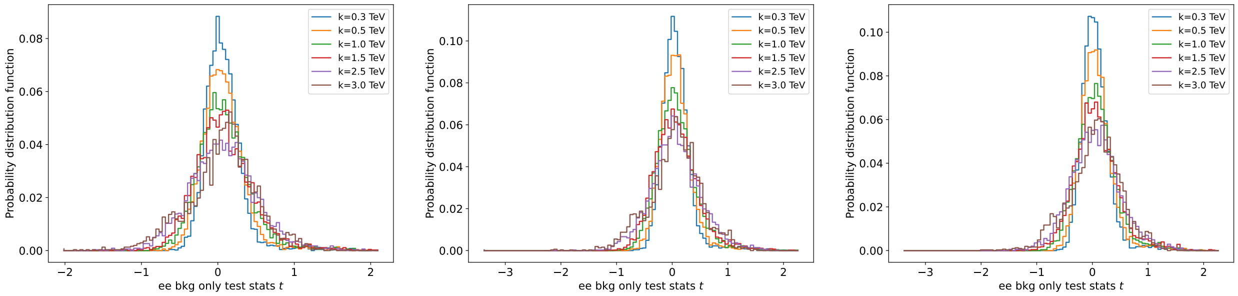

e^+e^- M_5=1.0 TeV e^+e^- M_5=2.0 TeV e^+e^- M_5=3.0 TeV

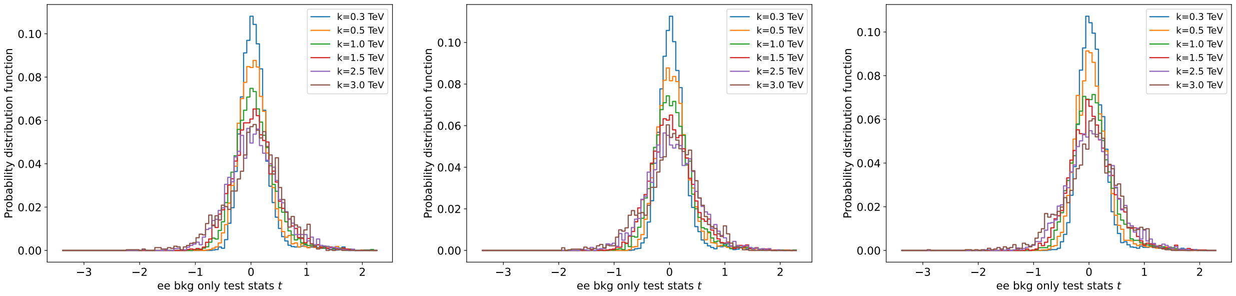

e^+e^- M_5=4.0 TeV e^+e^- M_5=5.0 TeV e^+e^- M_5=6.0 TeV

Fig.G.1: A collection of e^+e^- background only test statistic t distribution plots. Higher k results in a wider distribution.

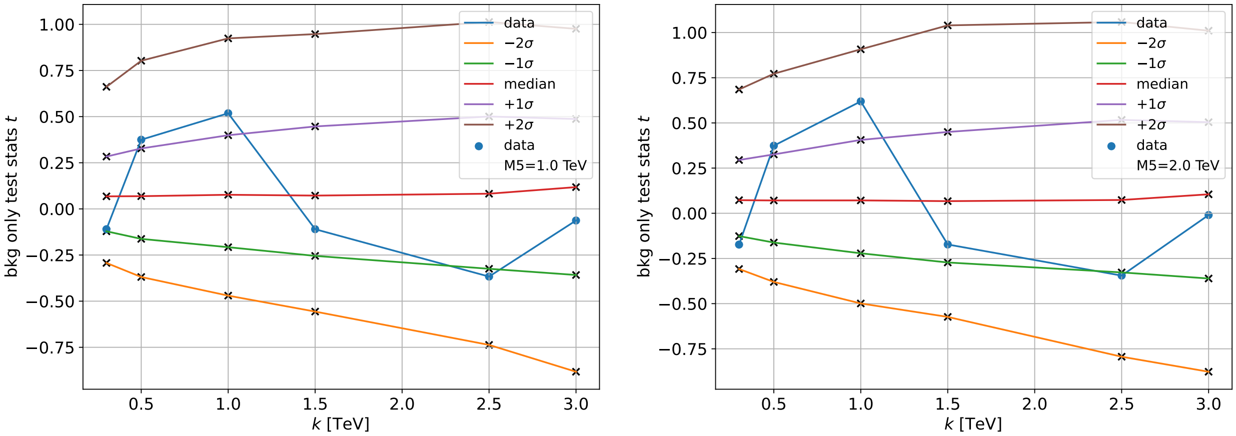

e^+e^- M_5=1.0 TeV e^+e^- M_5=2.0 TeV

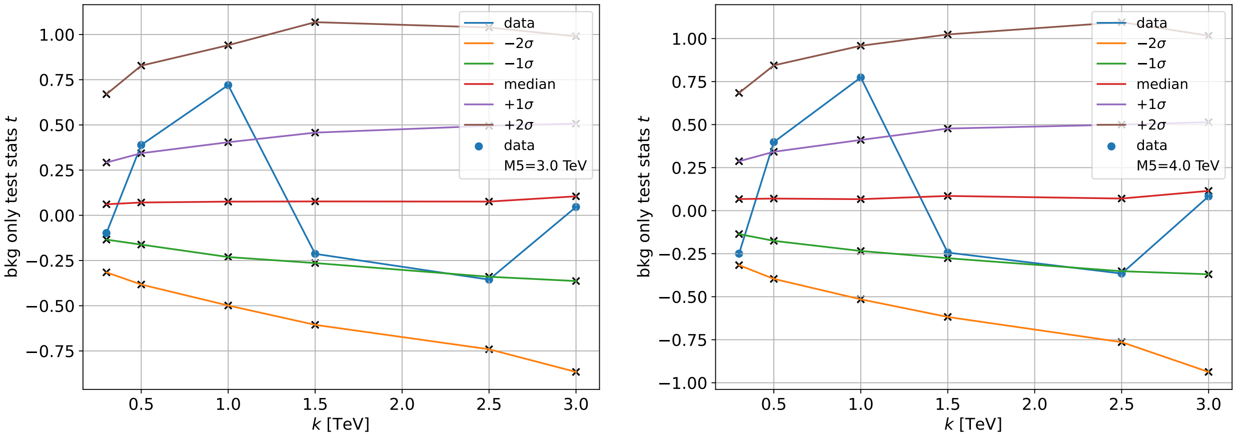

e^+e^- M_5=3.0 TeV e^+e^- M_5=4.0 TeV

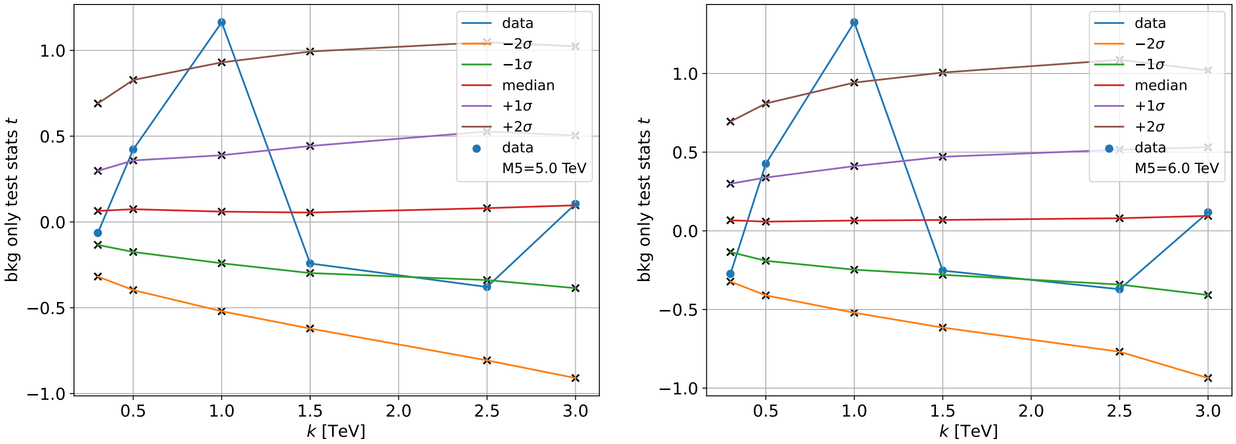

e^+e^- M_5=5.0 TeV e^+e^- M_5=6.0 TeV

Fig.G.2: A collection of e^+e^- data tested against different M_5 models. Quantile of the test statistic t is plotted as supplementary information.

Appendix H: $\gamma\gamma$ Background statistics

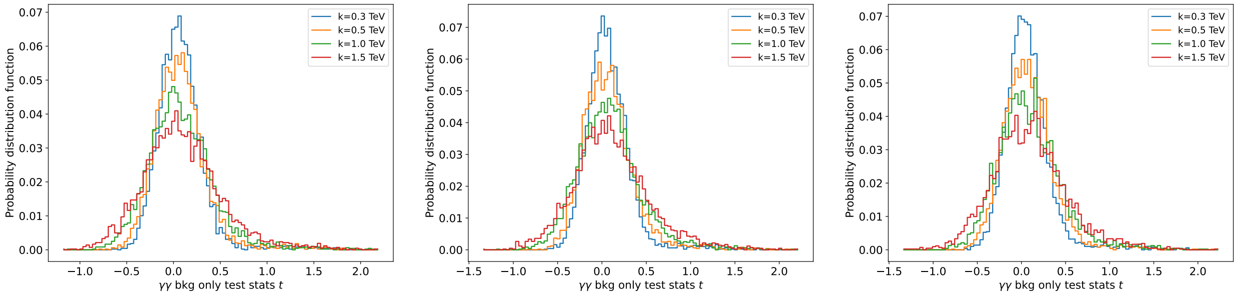

$\gamma\gamma$ M_5=1.0 TeV $\gamma\gamma$ M_5=2.0 TeV $\gamma\gamma$ M_5=3.0 TeV

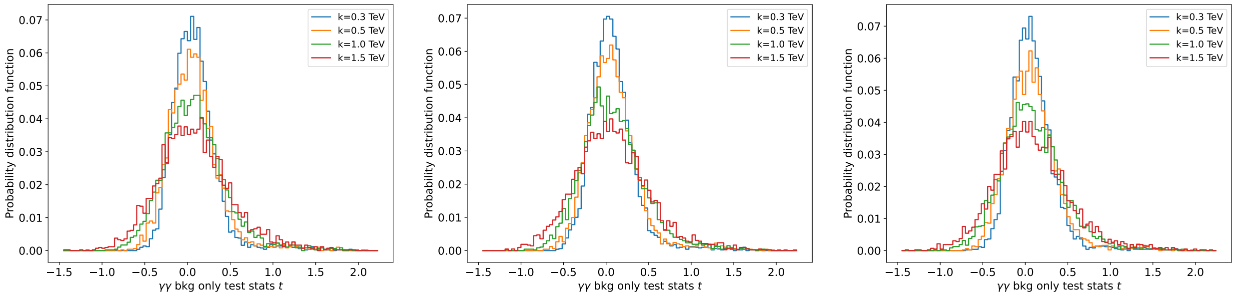

$\gamma\gamma$ M_5=4.0 TeV $\gamma\gamma$ M_5=5.0 TeV $\gamma\gamma$ M_5=6.0 TeV

Fig.H.1: A collection of $\gamma\gamma$ background only test statistic t distribution plots. Higher k results in a wider distribution.

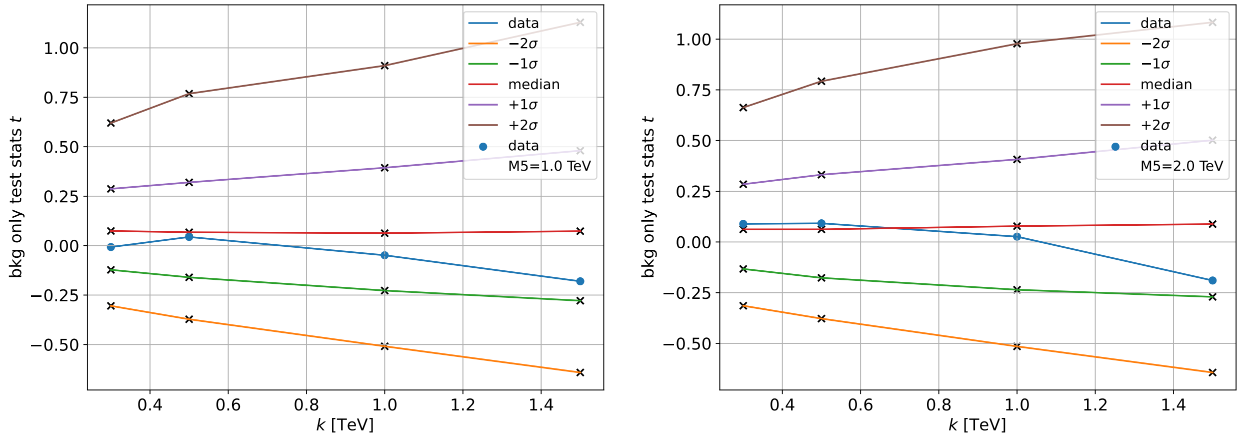

$\gamma\gamma$ M_5=1.0 TeV

$\gamma\gamma$ M_5=2.0 TeV

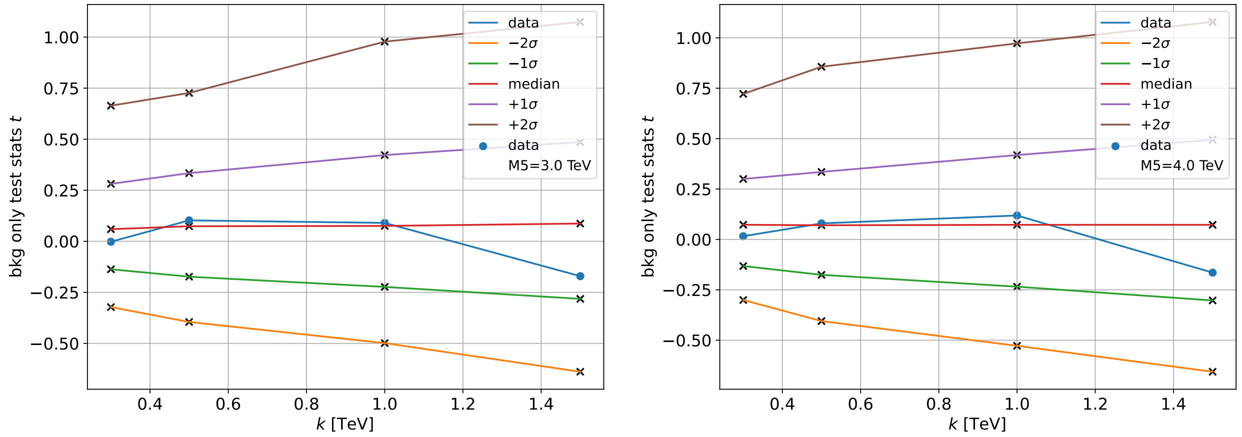

$\gamma\gamma$ M_5=3.0 TeV

$\gamma\gamma$ M_5=4.0 TeV

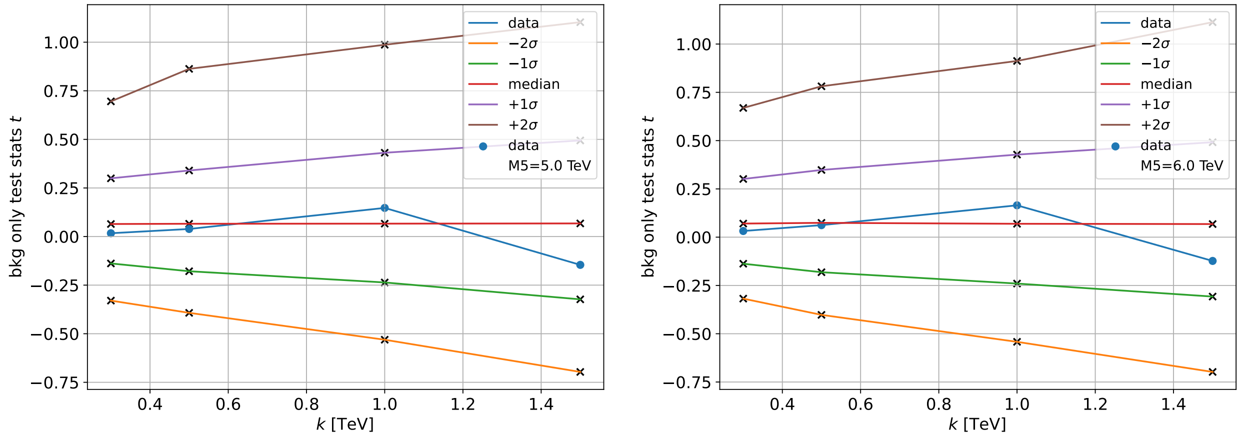

$\gamma\gamma$ M_5=5.0 TeV

$\gamma\gamma$ M_5=6.0 TeV

Fig.H.2: A collection of $\gamma\gamma$ data tested against different M_5 models. Quantile of the test statistic t is plotted as supplementary information.